



A multi-organ chip with matured tissue niches linked by vascular flow

Kacey Ronaldson-Bouchard¹, Diogo Teles^{1,2,3}, Keith Yeager¹, Daniel Naveed Tavakol¹, Yimu Zhao¹, Alan Chramiec¹, Somnath Tagore⁴, Max Summers¹, Sophia Stylianos¹, Manuel Tamargo¹, Busub Marcus Lee¹, Susan P. Halligan¹, Erbil Hasan Abaci⁵, Zongyou Guo⁵, Joanna Jacków⁵, Alberto Pappalardo⁵, Jerry Shih⁶, Rajesh K. Soni⁷, Shivam Sonar⁸, Carrie German⁸, Angela M. Christiano^{5,9}, Andrea Califano^{10,11,12,13}, Karen K. Hirschi¹⁴, Christopher S. Chen¹⁵, Andrzej Przekwas⁸ and Gordana Vunjak-Novakovic^{1,12,15} ✉

Engineered tissues can be used to model human pathophysiology and test the efficacy and safety of drugs. Yet, to model whole-body physiology and systemic diseases, engineered tissues with preserved phenotypes need to physiologically communicate. Here we report the development and applicability of a tissue-chip system in which matured human heart, liver, bone and skin tissue niches are linked by recirculating vascular flow to allow for the recapitulation of interdependent organ functions. Each tissue is cultured in its own optimized environment and is separated from the common vascular flow by a selectively permeable endothelial barrier. The interlinked tissues maintained their molecular, structural and functional phenotypes over 4 weeks of culture, recapitulated the pharmacokinetic and pharmacodynamic profiles of doxorubicin in humans, allowed for the identification of early miRNA biomarkers of cardiotoxicity, and increased the predictive values of clinically observed miRNA responses relative to tissues cultured in isolation and to fluidically interlinked tissues in the absence of endothelial barriers. Vascularly linked and phenotypically stable matured human tissues may facilitate the clinical applicability of tissue chips.

Drug safety and efficacy are typically evaluated in animal models, which frequently fail to predict clinical responses^{1–4}. Microphysiological systems with bioengineered human tissues designed to mimic organ-level functions are being developed to enable modelling of human physiology in vitro^{5–10}. Culturing a tissue in isolation can provide meaningful insights into some of the organ functions, but not the systemic interactions that influence organ responses to injury, disease and therapy^{5,8,11,12}. Organs in the body interact by virtue of (1) ‘boundaries’ preserving the specificity of their individual environments, (2) ‘endothelial barriers’ separating the intratissue from intravascular spaces and (3) ‘organ–organ cross-talk’ via vascular flow. These features are critical for tissue homeostasis in health and disease. Diseases that impact several organs and vascular flow are particularly difficult to emulate in vitro. Systemic diseases of high interest remain understudied, including cancer, fibrosis, inflammation and infection.

Although there is a clear need for microphysiological system designs that can model the complexity of human physiology, the functional integration of tissues has been an elusive goal due to the conflicting requirements for maintaining and connecting tissue-specific niches¹³. Current methods rely on transferring

supernatant between the tissues or use of shared (common) media that contain a mix of factors collectively required by all tissues in the system^{3,5,10}. While these models can recapitulate certain aspects of human pathophysiology^{9,13,14}, they provide limited phenotypic stability when the same medium is used to cultivate tissues from different germ layers. Common media can also induce committed cells to revert back to more plastic and immature phenotypes. As engineering of physiologically matured tissues continues to advance, methods to preserve the achieved maturity of physiologically linked multi-tissue systems also need to be developed.

To this end, we designed a ‘Multi-organ’ tissue chip that allows physiologically relevant integration of bioengineered tissues by (1) providing each tissue with its own specialized environment, (2) connecting tissues by vascular flow, and (3) separating the vascular and tissue compartments by a selectively permeable endothelial barrier. The tissue chip contained four tissues: heart, bone, liver and skin, selected for their distinctly different properties and importance for modelling diseases and testing drugs. The tissues were engineered from human induced pluripotent stem cells (hiPSC) for biological specificity and combined with supporting stromal cells (primary or hiPSC) within a physiologically relevant extracellular matrix (ECM), matured individually for 4–6 weeks

¹Department of Biomedical Engineering, Columbia University, New York City, NY, USA. ²Life and Health Sciences Research Institute (ICVS), School of Medicine, University of Minho, Braga, Portugal. ³ICVS/3B's, PT Government Associate Laboratory, Braga/Guimarães, Braga, Portugal. ⁴Department of Systems Biology, Columbia University, New York City, NY, USA. ⁵Department of Dermatology, Columbia University, New York City, NY, USA. ⁶Department of Biomedical Engineering, Boston University, The Wyss Institute for Biologically Inspired Engineering at Harvard University, Boston, MA, USA. ⁷Herbert Irving Comprehensive Cancer Center, Columbia University, New York City, NY, USA. ⁸CFD Research Corporation, Huntsville, AL, USA. ⁹Department of Genetics and Development, Columbia University, New York City, NY, USA. ¹⁰Department of Biomedical Informatics, Columbia University, New York City, NY, USA. ¹¹Department of Biochemistry and Molecular Biophysics, Columbia University, New York City, NY, USA. ¹²Department of Medicine, Vagelos College of Physicians and Surgeons, Columbia University, New York City, NY, USA. ¹³J.P. Sulzberger Columbia Genome Center, New York, NY, USA. ¹⁴Department of Cell Biology, University of Virginia, Charlottesville, VA, USA. ¹⁵College of Dental Medicine, Columbia University, New York, NY, USA. ✉e-mail: gv2131@columbia.edu

under conditions promoting their phenotype, transferred into the tissue chip and linked by vascular flow.

The maintenance of matured tissues in the Multi-organ tissue chip was compared to that of the Mixed tissue chip (equivalent to the Multi-organ tissue chip, except for the lack of endothelial barrier, thus representing the common medium culture) and Isolated cultures (tissues cultured individually, with and without endothelial barriers). To demonstrate the tissue chip utility for drug screening, we investigated the multi-organ toxicity of doxorubicin (a drug metabolized by the liver) from measured tissue responses at the molecular, cellular and functional levels in all tissue chip configurations. Experimental and computational pharmacokinetics/pharmacodynamics (PK/PD) studies were also conducted for these configurations, enabling further understanding of the contributions of tissues cultured systemically versus individually, with and without endothelial barriers. The tissue outcomes were benchmarked and validated using data from adult and paediatric clinical studies detailing miRNA biomarkers related to doxorubicin-induced cardiac toxicity, the most serious side effect of chemotherapy^{14–19}.

Results

Multi-tissue chip designs. The Multi-organ tissue chip was designed to allow physiological communication of engineered human tissues over long culture times (4 weeks), while maintaining their individual phenotypes (Fig. 1a,b, and Extended Data Figs. 1a–c and 2). All tissues and endothelium were matured individually before integration to establish adult-like functions and connected by vascular flow containing circulating immune cells, cytokines and extracellular vesicles, with an endothelial barrier separating the tissues and vascular flow. The tissue chip is manufactured from polysulfone, a biocompatible inert polymer. The tissue chambers are modular, have open access and can be connected in any order to model different physiological scenarios (Fig. 1b, Extended Data Fig. 1d–f and Supplementary Video 1), by virtue of the same outside geometry and customized interiors, leak-free click connectors and ports. The tissue chip uses a single channel of a peristaltic pump to recirculate culture media at a set flow rate and shear stress (Extended Data Figs. 1g,h and 2). The modular design allows tissues to be placed into the tissue chip after they have passed quality control and enables configurability in terms of the types, numbers and order of the tissues, tailored to the exact experimental design. To validate the tissue chip utility, we evaluated the maintenance of tissue phenotypes over 4 weeks of culture (Fig. 1c) and in response to doxorubicin (Fig. 1d).

Generating matured human tissues. Achieving and maintaining tissue maturity, which is necessary for recapitulating adult human physiology, has been difficult to achieve for tissues derived from hiPSCs. We formed and matured tissues individually before link in the tissue chip, allowing different maturation regimens and durations required for different tissue types as well as quality control of each tissue to maximize consistency. The methods for tissue formation and maturation and the specifications of tissue properties are summarized in Fig. 2, Extended Data Fig. 3 and Supplementary Table 1.

'Heart muscle' was formed from hiPSC-derived cardiomyocytes (CM) and fibroblasts in a fibrin matrix anchored to two auxotonic flexible pillars, and electromechanically matured at an increasing intensity for 4 weeks (Fig. 2a), as we previously reported¹¹. Electromechanically matured tissues displayed aligned sarcomeres with high expression of alpha-actinin-2, increased maximum capture rate, decreased excitation threshold and increased contractile force compared with non-matured controls (Extended Data Fig. 3a–c).

'Liver tissues' were formed from aggregates of hiPSC-derived hepatocytes and supporting human fibroblasts encapsulated in fibrin matrix²⁰ (Fig. 2b and Extended Data Fig. 3d). The liver tissues

displayed active metabolism and sustained production of albumin (Extended Data Fig. 3e).

'Bone tissues' were made by seeding human bone-marrow-derived mesenchymal stromal cells (MSC) into decellularized bone scaffolds and inducing the cells towards the osteoblastic phenotype over a period of 3 weeks²¹ (Fig. 2c). To recapitulate the osteolytic cycle, primary CD14⁺ monocytes were seeded into the osteoblastic bone and cultured in osteolytic medium capable of supporting both existing osteoblasts and additional monocytes as they differentiate into osteoclasts²¹. The resulting bone tissues displayed high presence of bone sialoprotein and osteocalcin, and mature tissue-specific morphology, as detailed by the presence of osteoblast leading edges and tartrate-resistant acid phosphatase (TRAP) positive lacunae (Extended Data Fig. 3f). Micro-computed tomography imaging showed increased bone density during osteoblastic maturation and stable bone volume during the induction of the osteolytic phase of bone maturation (Extended Data Fig. 3g).

'Skin tissues' were produced by seeding human dermal fibroblasts into collagen matrix, adding human keratinocytes, and by cultivation at the air–liquid interface for 3 weeks, to form and mature stratified epidermal tissues (Fig. 2d and Extended Data Fig. 3h)²². These tissues showed barrier function, as determined by measurement of the transepithelial/transendothelial electrical resistance (TEER), consistent with published values for human skin explants (Extended Data Fig. 3i)²³.

Generating a mature and selectively permeable vascular barrier.

Underneath each tissue chamber is an elastic mesh insert (Fig. 3a,b and Extended Data Fig. 2a) covered with endothelial cells and supporting MSCs^{24,25} forming a vascular barrier (Extended Data Fig. 4a,c). We found that the 20 μm pores best supported the formation of confluent endothelium (Fig. 3c and Extended Data Fig. 4a,b). We further evaluated the effects of shear stress (1.88 to 6.27 dynes cm^{-2}) on the vascular endothelium, and determined that lower shear stress was more conducive to the maintenance of a stable vascular barrier (Fig. 3d and Extended Data Fig. 4c,d). We also determined that a slow ramping of the applied shear stress facilitated the establishment of the endothelial barrier, and matured the endothelial and mesenchymal cells by gradual exposure to haemodynamic shear⁷ increasing from 0.5 to 1.88 dynes cm^{-2} over 60 h of culture (Fig. 2e). Tight barrier function was maintained at a shear stress of 1.88 dynes cm^{-2} , with the formation of vascular gap junctions and barrier integrity (Fig. 3d and Extended Data Fig. 4c,d). The tissues communicated by cytokines, exosomes and cells in the circulating flow beneath the vascular barrier (Extended Data Fig. 4e). Additionally, these studies were conducted using hiPSC from a single donor, thereby demonstrating the tissue chip's utility for 'patient-on-a-chip' models. The ability to use matched patient-specific cells in each linked engineered tissue enables in vitro human studies of an individual patient and their specific genetic background at both the individual organ and systemic level.

To document cross-talk between tissues, we generated heart tissues from hiPSC-derived CM transfected with a green fluorescent protein (GFP)-labelled CD63 exosome reporter (Fig. 3e), thereby enabling the tracking of a non-ubiquitous organ-specific marker of known origin. CD63 exosomes secreted by heart tissues were found in all tissues after 2 weeks of culture in the Multi-organ tissue chip (Fig. 3f,g). Similarly, immunofluorescence imaging of the vascular barrier beneath the heart tissue after 2 weeks showed exosome uptake by endothelial cells (Fig. 3h).

To include immune cells into the vascular flow, CD14⁺ monocytes were added into the reservoir. Over 98% of the initial monocytes expressed CD14 and ITGAM (CD11b) markers (Extended Data Fig. 5a and Supplementary Fig. 1), attached to the endothelial barriers (Extended Data Fig. 5b) and remained viable in the tissue chip, with or without endothelial barrier (Extended Data Fig. 5c).

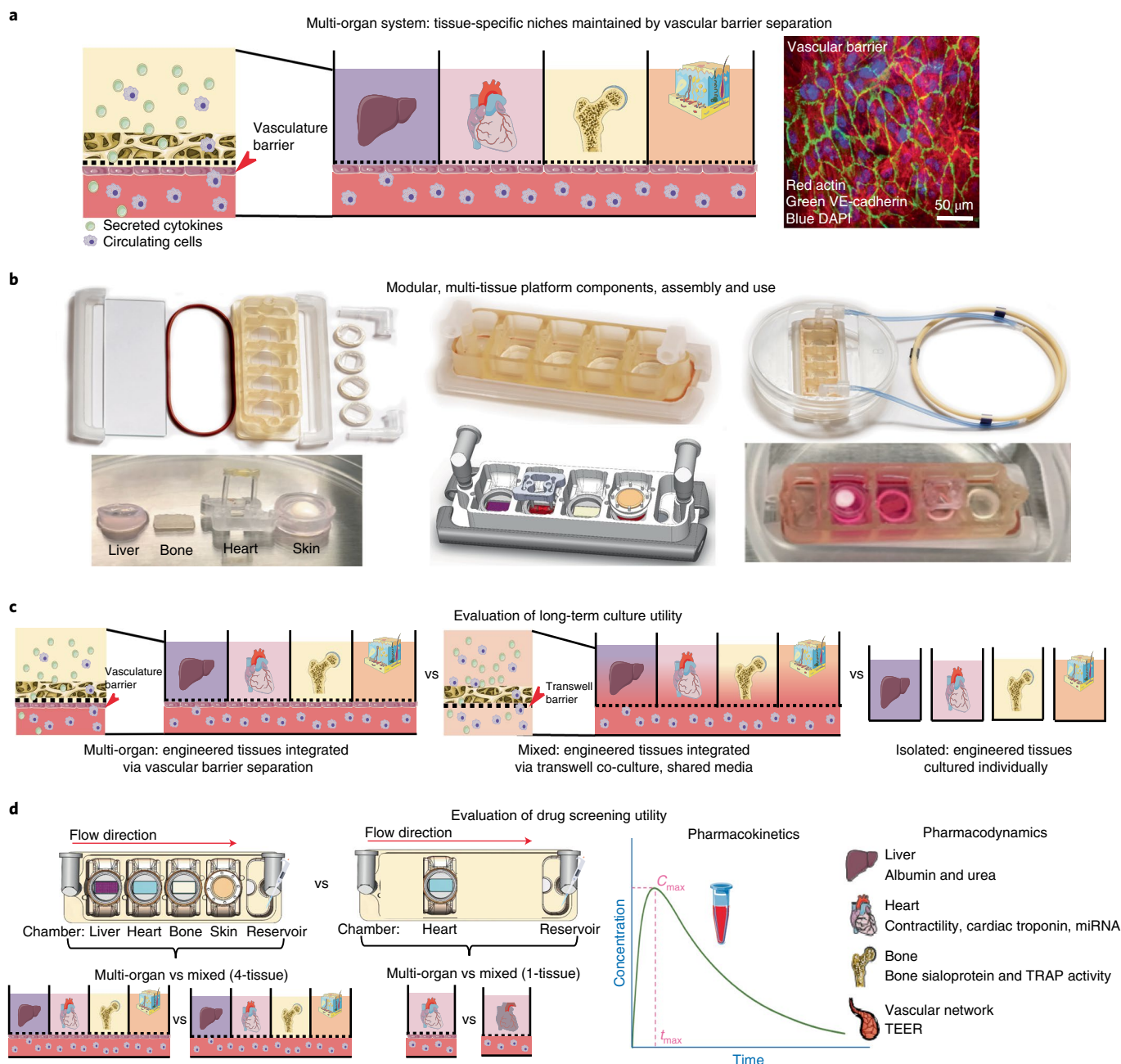


Fig. 1 | Integrated Multi-organ chip enables maintenance of a tissue-specific niche while allowing for organ cross-talk. **a**, Left: schematic detailing a side view of the multi-tissue chip where integration is enabled by a vascular barrier beneath each tissue, which creates a tissue-specific niche in the above chambers for each engineered organ while enabling cross-talk between organs within the system through the vascular circulation. Right: immunostaining demonstrates expression of actin alpha (red) and VE-cadherin (green) by the endothelial barrier. Samples were counterstained with DAPI (blue). Scale bar, 50 μm . **b**, Top row: photographs detailing that the engineered chip is easily configurable, allowing for a ‘plug-and-play’ system for individual organ chambers and a vascular flow channel beneath each organ. Bottom row: engineered tissues are shown before and after being placed into the engineered tissue chip, where the vascular barrier enables maintenance of each specific medium, as detailed by the differences in medium colour within the photograph. **c**, Schematics of the experimental design for evaluating the tissue chip’s long-term culture utility and validating the importance of the vascular barrier within the Multi-organ tissue chip, as compared to the lack of a vascular barrier in the Mixed tissue chip, and benchmarked against the tissues cultured for the same length of time in isolation. **d**, Schematics of the experimental designs for evaluating tissue chip utility for drug screening of doxorubicin, where the pharmacokinetic (middle right) and pharmacodynamic (right) drug responses of the engineered tissues cultured in the Multi-organ and Mixed tissue chips were compared directly, for cases where all four tissue, or single tissues were cultured in either tissue chip.

Over 4 weeks, monocytes in the Multi-organ tissue chip maintained their classical (CD16⁻CD14⁺) phenotype, whereas the Mixed and Isolated tissue chip shifted towards an intermediate (CD16⁺CD14⁺) phenotype (Extended Data Fig. 5d).

The circulating human CD14⁺ monocytes extravasated from vascular flow in response to injury signals, and otherwise stayed confined to the vascular compartment. Specifically, in response to a cryo-induced injury to the heart tissue, circulating immune cells

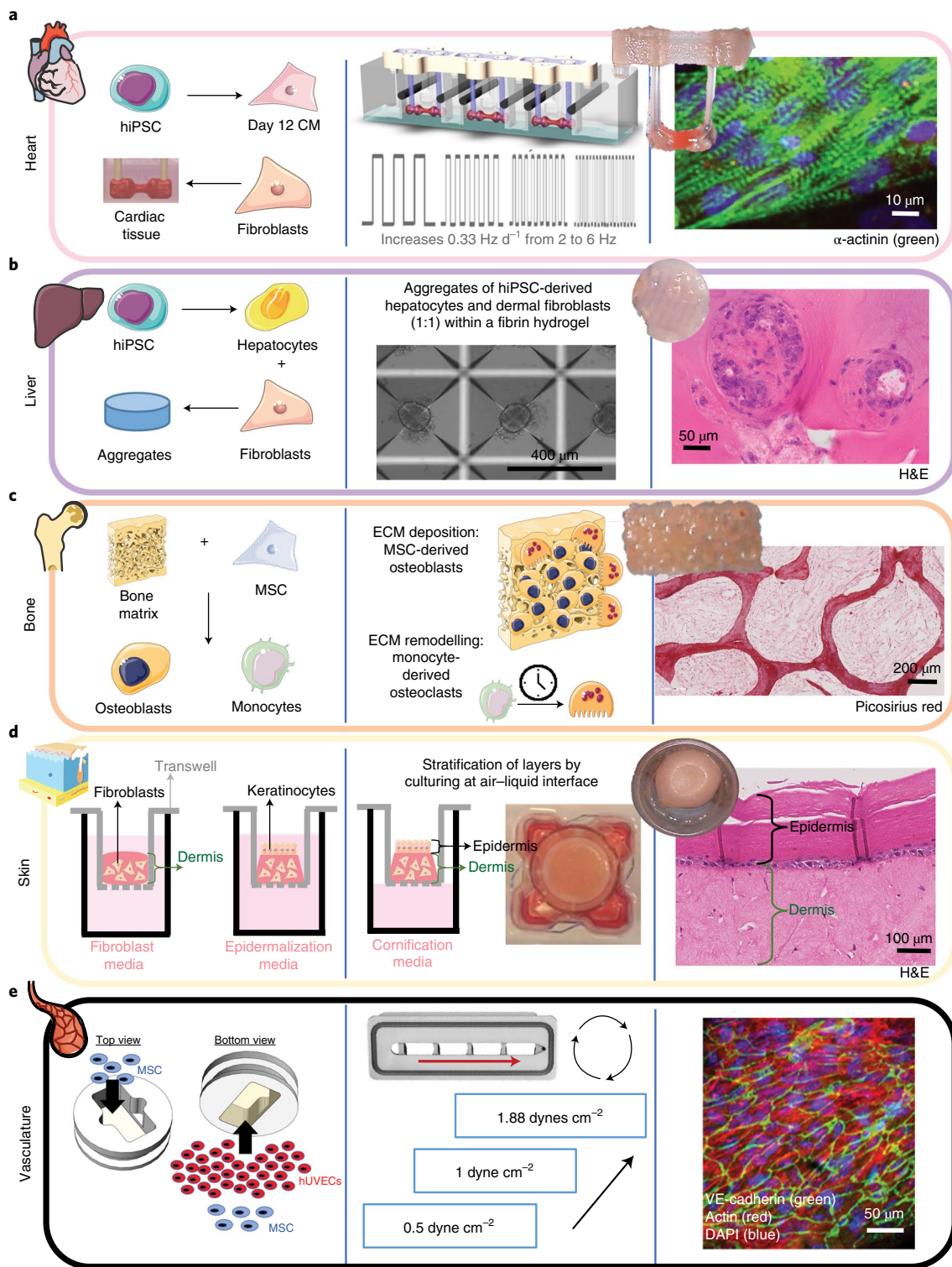


Fig. 2 | Formation, maturation and characterization of engineered human tissues. **a–e**, Schematics detailing initial tissue formation (cell types and scaffold or extracellular matrix (ECM)), tissue-specific maturation protocols, and representative tissue photographs and immunofluorescence or immunohistochemical images for heart (**a**), liver (**b**), bone (**c**), skin (**d**) and vasculature (**e**) after the maturation protocol is completed.

extravasated from the vascular flow within 24h and targeted the injured tissue, but not the healthy tissues. Selective infiltration of monocytes into the injured tissues was only seen in the Multi-organ tissue chip, whereas the Mixed tissue chip showed non-selective infiltration (Fig. 3i,j). Monocytes also accumulated on the endothelial layer underneath the injured tissues (Fig. 3k).

Upon injury, heart tissues secreted troponin, a ubiquitous cardiac-specific marker, which could be found in other tissue compartments, indicating cross-talk (Fig. 3l). Cardiac troponin concentrations were uniform within the Mixed tissue chip, a non-physiological condition that was due to the lack of a vascular barrier. Culture of healthy and cryoinjured heart tissues in adjacent

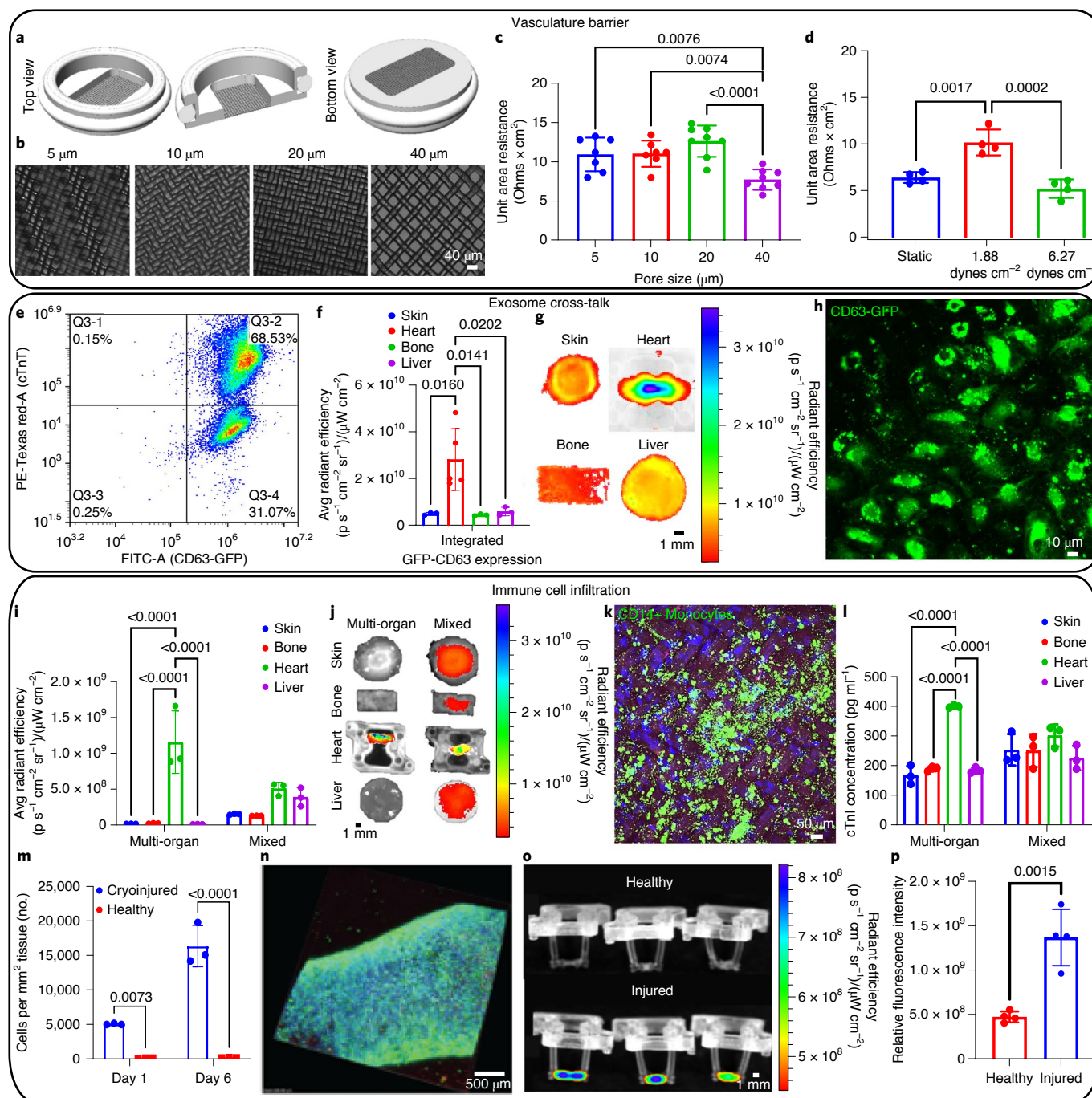


Fig. 3 | Multi-organ communication of tissue-specific niches via vascular barrier and vascular flow. **a–c**, Characterization of the vascular barrier insert (**a**) at various pore sizes (**b**) as measured by vascular TEER values (**c**) ($n=7-8$ biological replicates). **d**, TEER measurements as a function of shear stress ($n=4$ biological replicates). Data shown as mean \pm s.d. and statistics determined by one-way ANOVA. **e**, Cardiac tissues contain a majority of GFP⁺CD63⁺ cardiomyocytes, as indicated by expression of cardiac troponin (cTnT) and CD63 in quadrant 3 of the flow cytometry scatterplot. **f, g**, Average expression (**f**) (data shown as mean \pm s.d. and statistics determined by two-way ANOVA, $n=5$ biological replicates.) and tissue heat-map expression (**g**) of GFP⁺CD63 within all tissues cultured in the Multi-organ tissue chip for 2 weeks. **h**, Immunofluorescence image of GFP⁺CD63 expression within the vascular barrier beneath the cardiac tissue after 2 weeks. **i, j**, Average expression (**i**) and tissue heat-map expression (**j**) of labelled monocytes within all tissues cultured in the Multi-organ or Mixed tissue chips for 24 h (data shown as mean \pm s.d. and statistics determined by two-way ANOVA, $n=3$ biological replicates). **k**, Immunofluorescence image of CD14⁺ monocytes attached to the vascular barrier beneath the cardiac tissue after 24 h. Scale bar, 10 μm. **l**, Cardiac troponin concentration within each tissue chamber 24 h after cardiac cryoinjury (data shown as mean \pm s.d. and statistics determined by two-way ANOVA, $n=3$ biological replicates). **m**, Monocyte infiltration over time as measured by confocal tracking of labelled monocytes ($n=3$ biological replicates, data shown as mean \pm s.d. and statistics determined by two-way ANOVA). **n**, Immunofluorescence image of CD14⁺ monocytes (green) attached to a cryoinjured cardiac tissue counterstained with Hoechst 33342 (blue) after 7 d. Scale bar, 10 μm. **o, p**, Tissue heat-map expression (**o**) and average expression (**p**) of labelled monocytes within healthy and cryoinjured cardiac tissues after 7 d (data shown as mean \pm s.d., statistics determined by unpaired *t*-test, $n=4$ biological replicates).

chambers of the Multi-organ tissue chip showed selective infiltration of monocytes into only the injured heart tissue, a response that was maintained over 1 week of culture (Fig. 3m–p).

Physiological effects of tissue maturation. The methods we used to achieve maturity utilize tissue-specific mechanisms (chemical, metabolic, electrical and/or mechanical). Here we highlight the effects of maturation on the heart tissue, achieved by subjecting early hiPSC-derived CM encapsulated in fibrin hydrogel to electromechanical conditioning at a gradually increasing intensity. RNA sequencing of matured heart muscle revealed the role of electromechanical stimulation in promoting the development of contractile function, metabolism and calcium regulation (Supplementary Fig. 2a–c).

Ingenuity Pathway Analysis (IPA) revealed upregulation of the more mature sarcomere isoforms MYL2 and MYH7 (Supplementary Fig. 2a,c). GSEA against adult healthy human tissue databases²⁶ showed the enhancement of cardiac myogenesis, metabolic maturation via oxidative phosphorylation and fatty acid metabolism (Supplementary Fig. 2d), and highly upregulated pathways to striated tissue contraction, calcium handling and relaxation (Supplementary Fig. 2e). Gene set enrichment for gene ontology details that maturation promoted heart muscle contraction, development and differentiation (Supplementary Fig. 3).

Gene ontology (GO) analysis showed upregulation of biological processes related to the development of cardiac and striated muscle, myofibril assembly and striated muscle contraction (Supplementary Fig. 4a). Gene ontology for cellular components showed upregulation of cardiac-specific ultrastructure (sarcomere, myofibril, Z disc, I band) and sarcoplasmic reticulum (Supplementary Fig. 4b). Matured tissues recapitulated the clinical half maximal effective concentration (EC₅₀) values of several drugs, defined as the concentration of a compound that elicits 50% of its maximal overall effect values of several drugs, and the bradycardic effects of calcium channel blockers seen in patients (Supplementary Fig. 4c). Of note, screening of these drugs using hiPSC-derived CM monolayers revealed tachycardic responses²⁷, further supporting the need for maturation of engineered tissues for use in modelling disease.

Tissues maintain their phenotypes over 4 weeks in the Multi-organ tissue chip. The maturity of engineered tissues needs to be maintained after the tissues are connected for sufficient periods of time to conduct physiological studies. The Multi-organ tissue chip was designed to preserve the tissue-specific niche and mature phenotype of each tissue while enabling tissue–tissue communication. To evaluate this critically important capacity, the Multi-organ tissue chip was systematically compared over 4 weeks of culture to the identical tissue chip without endothelial barriers (Mixed condition, corresponding to the co-culture in common medium) and tissues cultured individually (Isolated condition, benchmark for phenotype stability) (Figs. 1c and 4).

All tissues in the Multi-organ tissue chip maintained the structural, functional and molecular stability of the ‘gold standard’ (Isolated group), and markedly exceeded the corresponding tissue properties in the Mixed group over 4 weeks of culture following integration by vascular flow (Fig. 4). Specifically, heart muscle showed increased cell elongation and striations in the Multi-organ and Isolated groups compared with the Mixed group. Bone tissues in the Multi-organ and Isolated groups displayed mature osteolytic phenotype, while the Mixed group showed decreased collagen deposition. Liver tissue morphology was comparable for the Multi-organ and Isolated groups and inferior in the Mixed group. The epidermal layer of the skin remained intact in the Multi-organ and Isolated groups, whereas the Mixed tissue chip showed disruptions (Fig. 4a,b,g).

The vascular endothelium in the Multi-organ tissue chip maintained barrier function, with the exception of the liver endothelium

that assumed decreased TEER value already by 2 weeks of cultivation (Fig. 4c). This result is consistent with the characteristically leaky liver endothelium that has lower VE-cadherin expression than other tissues. Further studies are needed for a more definitive characterization of tissue-specific endothelial commitment.

Tissue functions were comparable after 4 weeks of culture for the Multi-organ and Isolated groups. Heart tissues maintained the beating rate (Fig. 4d, Extended Data Fig. 8a,b), liver tissues maintained albumin secretion (Fig. 4e) and skin tissues maintained epidermal thicknesses (Fig. 4g). Bone tissues maintained the mature osteolytic TRAP activity only in the Multi-organ group, consistent with the notion that bone function requires interaction with other tissues that are not provided in the Isolated cultures (Fig. 4f). Connecting tissues without establishing physiologic separation between the vascular and tissue compartments (Mixed condition) did not support mature osteolytic function 4 weeks after connecting tissues in the tissue chip, suggesting that the maintenance of tissue-specific niches is critical for dynamic functions that rely on tissue communication. The Mixed tissue chip was unable to maintain cardiac contractility (Fig. 4d) or liver albumin production (Fig. 4e). Immune cell cytokine secretions remained stable over 4 weeks in the Multi-organ group, and decreased in the Mixed and Isolated groups (Extended Data Fig. 6a,b), suggesting that the vascular barriers may maintain immune cell function and homeostasis.

By whole proteome analysis, we detected thousands of proteins in each engineered tissue (heart: ~6,000; liver: ~4,000; bone: ~5,000; skin: ~2,000) that were differentially expressed between the Multi-organ and Mixed media conditions (Fig. 4d–g, and Extended Data Figs. 7 and 8). Through IPA and GO analysis, we identified common genes expressed in all tissues among the three conditions (Multi-organ, Mixed and Isolated; Figs. 1c and 5a). Notably, the top genes shared among all tissues in the Multi-organ and Isolated cultures were primarily related to normal physiological functions (for example, metabolism), while the shared genes under the Mixed condition were primarily related to the off-target organ functions (Fig. 5a, Supplementary Fig. 5).

Tissue-specific proteins expressed in adult and engineered tissues were identified and tertiled into high, medium and low expression levels on the basis of the Human Protein Atlas²⁸. Engineered tissues showed high overlap of gene expression with adult human tissues (Fig. 5b). Further comparisons of the expression levels of these overlapping genes between matched adult and engineered tissues revealed that the heart, bone and skin tissues in the Multi-organ and Isolated tissue chips more closely matched the published data for adult donors (Fig. 5b), outperforming the Mixed tissue chip. Additional analysis showed that engineered tissues in the Multi-organ tissue chip better matched the repertoire of highly abundant genes in adult heart, liver, bone and skin (Fig. 5c), confirming the enhanced ability of the Multi-organ tissue chip to preserve the biological fidelity of connected tissues over 4 weeks of culture. Proteins associated with epithelial, neurogenic and osteochondral development were markedly higher in heart tissues cultured under the Mixed conditions, presumably due to the presence of growth factors from adjacent tissues in the absence of an endothelial barrier (Fig. 5d).

Mixed culture conditions showed upregulated biological process pathways related to skin epidermis development within the bone tissues (Extended Data Fig. 7d), and upregulated collagen deposition, calcification and aberrant extracellular matrix reorganization (Extended Data Fig. 7g). Within the cardiac tissues, the Mixed culture conditions showed decreased functionality (Extended Data Fig. 8a,b), displayed differential protein activity that clustered separately (Extended Data Fig. 8c,d) and displayed opposing biological process pathways (Extended Data Fig. 8f) from the other conditions, and showed downregulation of genes related to cardiac structure, energetics and calcium handling (Extended Data Fig. 8e). Mixed

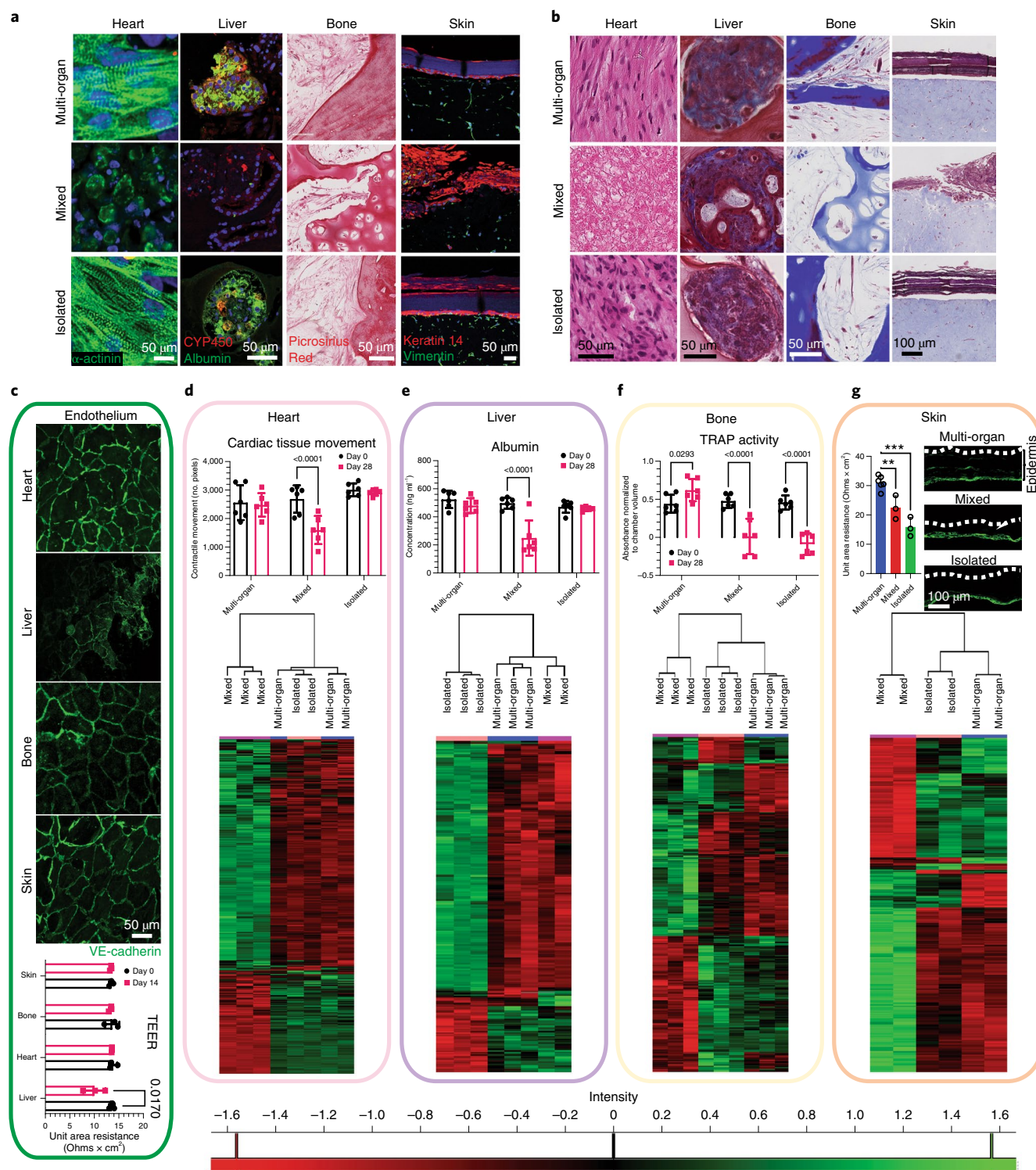


Fig. 4 | Multi-organ tissue chip maintained the phenotypes of each organ over 4 weeks of culture. a,b, Representative immunofluorescence staining (**a**) and trichrome histological staining (**b**) displays morphological differences between groups. Scale bar, 50 μm for heart, liver and bone; 100 μm for skin. **c**, Top images: vascular stability is maintained after 4 weeks in culture as shown by VE-cadherin expression (green). Scale bar, 50 μm . Bottom: TEER measurements of the endothelial barrier ($n=3$ biological replicates, data shown as mean \pm s.d. and statistics determined by two-way ANOVA). **d-g**, Functional (top) ($n=6$ biological replicates) and overall proteomic comparison of molecular features (bottom) ($n=2-3$ biological replicates) for each engineered organ compared in each condition. Immunostaining (**g**, top right) shows the epidermal layer of the skin. Scale bar, 100 μm . Data shown as mean \pm s.d. and statistics determined by two-way ANOVA.

culture conditions suppressed the pathways related to cardiac conduction, muscle contraction, striated muscle tissue development, action potential, muscle adaptation and cardiac cell development

within the cardiac tissues (Extended Data Fig. 8f). GO analysis of cellular components revealed that only Multi-organ and Isolated conditions maintained the mature cardiac phenotype, as evidenced

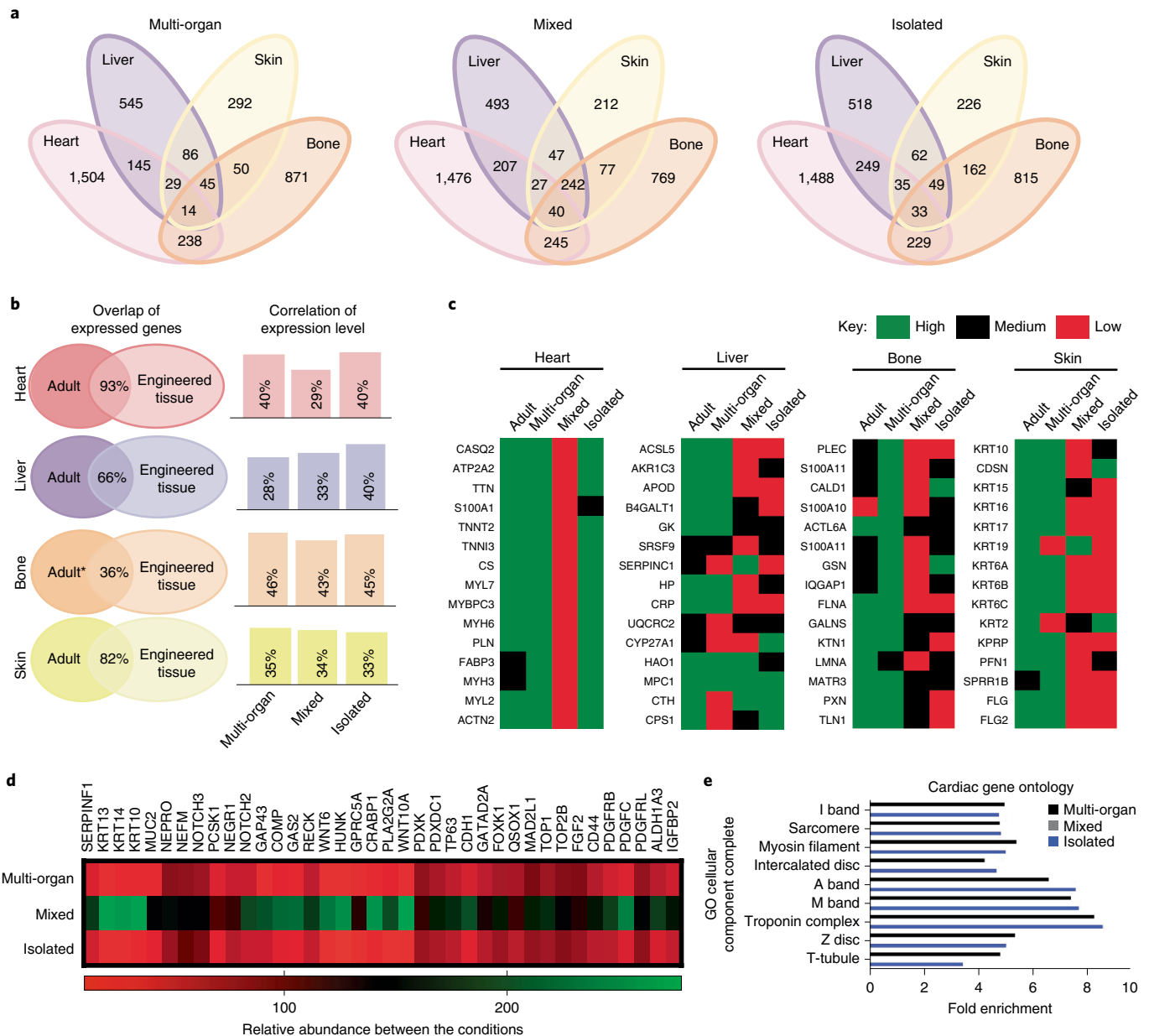


Fig. 5 | Proteomic analysis confirms biological fidelity of Multi-organ tissue chip in comparison with gold standards and adult organs. **a**, When comparing all engineered organs within each experimental group, GO analysis identified gene pathways shared among the different organs. **b**, Comparison between published adult data and engineered tissues demonstrates high similarities in the shared expression of genes to native tissue (left); additional comparison of how the expression level of these shared genes within each experimental group correlates with adult tissue is also presented (right). (*corresponds to bone marrow tissue comparison, due to unavailability of bone tissue data) **c**, Within each organ system, top proteins of interest were identified via the Human Protein Atlas and compared to adult tissue. **d**, Data show the relative abundance of proteins between the conditions. In cardiac tissues cultured in the Mixed group, we identified a number of candidate proteins that are often found in off-target tissues, including in development of epithelial, osteochondral and neural tissues. In contrast, cardiac tissues in Multi-organ tissue chips and isolated cultures maintained high biological fidelity. **e**, GO analysis identified cardiac-specific, adult-like structural components present in the Multi-organ (black) and Isolated (blue) groups, but not in the Mixed condition (grey).

by enriched contractile proteins and T-tubules (Fig. 5e), further supporting the need to preserve tissue-specific niches.

Mechanistic multi-compartment model of the tissue chip for drug studies. PK models are typically formulated as a multi-compartment model (flow-rate limited) or a blood-tissue model (permeability-rate limited)^{29–32}. To enable in vivo translation, we developed a mechanistic multi-compartment model of the Multi-organ tissue chip (Extended Data Fig. 9a) using ordinary differential equations (ODE) for distributed multi-compartment

reduced-order model that simulated the tissue chambers fluidically connected by a closed vascular flow loop. Each chamber was modelled with a fluidic inflow segment (IFC), fluidic perfusion segment (FC), endothelialized membrane (MM) and a tissue tank (T).

The topology of each tissue was designed to replicate its morphology and location. The heart tissue was suspended by vertical pillars, the skin tissue was cultured in the top section to maintain air-liquid interface, and the liver and bone tissues were cultured in the lower sections (Extended Data Fig. 9b–f). The endothelial barrier was modelled as a porous membrane with a layer of cells

at each side (Supplementary Fig. 6a). For simulation of studies without endothelial barrier (Mixed conditions), the membrane separating the tank from the fluidic channel consisted of a single layer (Supplementary Fig. 6d,e). A set of flux equations was used to calculate drug transport across the tissue chip. As tubing permits partitioning of lipophilic compounds, we solved for species mass transport between the fluid and the tubing wall.

In a previous study, we showed relatively slow diffusive distribution of a drug within the tissue chamber³³. For better resolution of concentration gradients, each tissue chamber was divided into three sub-compartments. The reservoir had a time-dependent volume due to sampling. The entire fluidic loop was represented as a virtual linear model with a number of segments in the external flow loop. The mathematical models were solved for the time-dependent fluid mass and species transport, assuming constant flow rates. We validated the model for mass and volume conservation over the entire duration of simulation (Supplementary Fig. 6b,c).

Fluorescein isothiocyanate (FITC)-labelled dextran was circulated for 72 h without measurable absorption by the transwells (Supplementary Fig 7a). In previous studies, we had already tested FITC absorption by the tissue chip with similar results³³. We also assessed diffusion through the transwell and observed FITC-dextran reached a uniform concentration after 72 h, without flow rate (Supplementary Fig. 7b). FITC-dextran introduced into the circulation at a 3.3 ml min^{-1} flow rate reached uniform concentration between all chambers within 24 h (Supplementary Fig. 7c–h).

PK model of doxorubicin. Having established tissue-specific functionality along with tissue cross-talk over 4 weeks of culture, the Multi-organ tissue chip provided an in vitro mimic of human physiology for drug testing. To show capability for elucidating the PK and PD of therapeutic agents, we modelled cardiotoxicity of doxorubicin, a drug used in treating several types of cancer. Doxorubicin is metabolized in the liver into doxorubicinol, which we also observed in doxorubicin-exposed liver tissues (Supplementary Fig. 8). A doxorubicin dose of $30 \mu\text{M}$ ($17,400 \text{ ng ml}^{-1}$) was determined according to the surface area of the tissues to correspond to the clinically administered cumulative dose shown to induce cardiotoxicity^{17,18} and was delivered to the tissues through the vascular channel.

We compared the Multi-organ condition against the Mixed condition and the Isolated single-tissue tissue chips with and without endothelium (Fig. 1d) to elucidate the effects of the endothelial barrier and tissue communication. The predictive power of the computational model was determined against experimental data. The time-concentration profiles of doxorubicin and doxorubicinol in the Multi-organ tissue chip (Fig. 6) show that the model closely matched the experimental data, correctly predicting doxorubicin metabolism into doxorubicinol by liver tissue, and its diffusion into tissue chambers and the reservoir over time. The peak drug concentration in the heart tissue chamber was the lowest, most probably due to some absorption of the drug by the elastomer pillars supporting the tissue. Also, for the first timepoint, the calculated doxorubicin concentration in the reservoir did not fit well with the experimental data, presumably due to the model assumption of perfect mixing. The concentration profile of doxorubicin and doxorubicinol in the Mixed tissue chip (Supplementary Fig. 9) reached a peak faster than in the Multi-organ tissue chip, presumably due to less resistance to drug transport in the absence of the endothelial barrier.

The concentration–time profiles for the Mixed tissue chip were consistently above those for the Multi-organ tissue chip (Extended Data Fig. 10). This result is in line with the fewer barriers to drug diffusion between the fluidic channels and the tissue chambers in the Mixed tissue chip. The higher concentration of the metabolite doxorubicinol in the liver chamber is also expected as the primary drug doxorubicin is metabolized by the liver.

PD model of doxorubicin. We then studied whether the Multi-organ tissue chip was able to model doxorubicin PD by exposing all tissue chip configurations to the same concentration of doxorubicin ($30 \mu\text{M}$) over 72 h, as in PK studies. Liver tissues showed decreased albumin production and stable urea production (Fig. 7a,b), as seen clinically³⁴. Cardiac excitability decreased and cardiac troponin I release increased, both of which are clinical measures of cardiac cell damage (Fig. 7c,d). Bone tissues displayed decreased bone sialoprotein levels only in the Multi-organ tissue chip (Fig. 7e), with stable TRAP responses (Fig. 7f) and decreased cellularity (Fig. 7g), suggesting that osteoblasts are more sensitive to doxorubicin than osteoclasts, as observed in pre-clinical studies³⁵. As expected, the endothelium showed decreased resistance in response to doxorubicin (Fig. 7h).

Identification of miRNA biomarkers of doxorubicin cardiotoxicity. Current monitoring of cardiotoxicity in patients receiving doxorubicin includes measurements of left ventricular ejection fraction and cardiac troponin serum levels. Recently, miR-1 has been identified as a superior biomarker for predicting patients who will develop doxorubicin-induced cardiotoxicity³⁶. We also detected increased cardiac troponin I levels after doxorubicin treatment and changes in miRNAs including miRNA1 (Fig. 7c,i–m).

Differential miRNA expression was measured in the heart tissues and vascular flow by the GeneChip miRNA 4.0 Array following doxorubicin treatment to predict doxorubicin-induced cardiotoxicity and subsequent cardiomyopathy for heart tissues cultured in the presence of the other tissues (4-tissue) or in isolation (1-tissue) (Fig. 1d), as shown in Fig. 7i–m and Supplementary Figs. 10–12^{14,16,19}. Only the Multi-organ tissue chip showed differential upregulation of miR-1 after doxorubicin treatment ($P=0.0028$). The Multi-organ configuration showed the highest fold change (FC) of miR-1 (Multi-organ vs Mixed FC = 38.84, $P=0.0015$, Fig. 7i), followed by the 1-tissue tissue chip (Multi-organ vs Mixed FC = 18.84, $P=0.0245$, Fig. 7j). Evaluation of the perfusate from the Multi-organ and Mixed conditions also showed upregulated miR-1 only in the Multi-organ tissue chip (4-tissue Multi-organ vs Mixed perfusate FC = 4.69, $P=0.0048$, Fig. 7k).

Identification of miRNA biomarkers of doxorubicin cardiomyopathy. We were able to detect early miRNA biomarkers of doxorubicin cardiomyopathy suggested by a recent clinical study identifying 17 miRNAs differentially expressed in paediatric cancer patients who developed left ventricle failure following treatment with doxorubicin (Fig. 7l,m)¹⁶. Following principal component analysis dimensionality reduction, the statistically significant similarity of the clinical data cluster to the Multi-organ cluster ($P=0.0021$), but not to the Mixed model cluster ($P=0.11$) (Fig. 7l) suggests that linking of matured tissues by vascular flow provides a more physiological context than tissues cultured in common medium. When miRNAs were prioritized on the basis of their statistical significance for subsequent cardiomyopathy in the clinical study, 85.7% of the miRNAs in the Multi-organ model showed similar fold changes versus only 28.6% of the miRNAs in the Mixed 4-tissue model, and 71.4% for both the Multi-organ and Mixed 1-tissue models (Fig. 7m).

To further probe the capabilities of the Multi-organ tissue chip, we determined the differential activities of miRNAs that were identified in paediatric¹⁶ and adult¹⁹ clinical studies following doxorubicin treatment, by measuring the Normalized Enrichment Scores (NES) of their targets in underexpressed genes computed by GSEA analysis²⁶. Individual miRNA targets were assessed using the miRDB database³⁷.

Differential activity of previously validated paediatric miRNAs was highly significant in the Multi-organ tissue chip, consistent with clinical results for 10 out of 17 miRNAs (58.8%) versus 5

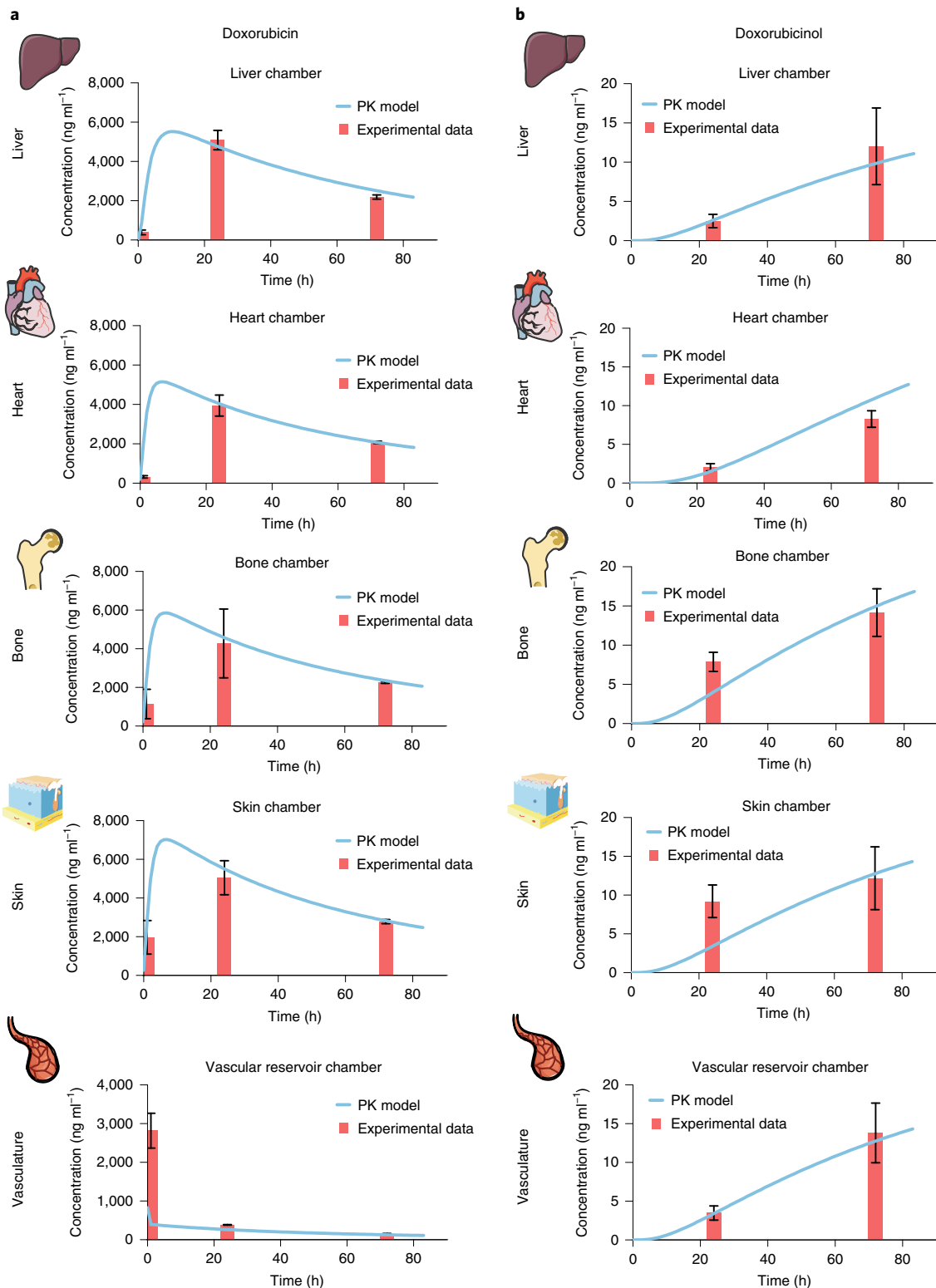


Fig. 6 | Experimental data and PK model of doxorubicin treatment in the Multi-organ tissue chip. a, b, Doxorubicin (a) and doxorubicinol (b) levels measured over time by UPLC-MS/MS within all tissue chambers and in the reservoir (red bar), compared with the prediction of the computational PK model (blue line). Data are mean \pm s.d. ($n=3$ biological replicates).

out of 17 miRNAs (29.4%) for the Mixed model (Supplementary Fig. 10a–c)¹⁶. For Isolated tissues, the presence of vascular endothelium increased specificity, with 12 vs 9 out of the 17 miRNAs, for vascularized vs nonvascularized tissues, respectively, (Supplementary Fig. 11a–c)¹⁶.

miRNA expression was also assessed for the vascular flow, to mimic clinical serum measurements. The Multi-organ perfusate showed miRNA activity consistent with clinical results for 9 out of the 17 (52.9%) paediatric miRNA biomarkers, compared with the Mixed model showing consistent activity for only 4 out of

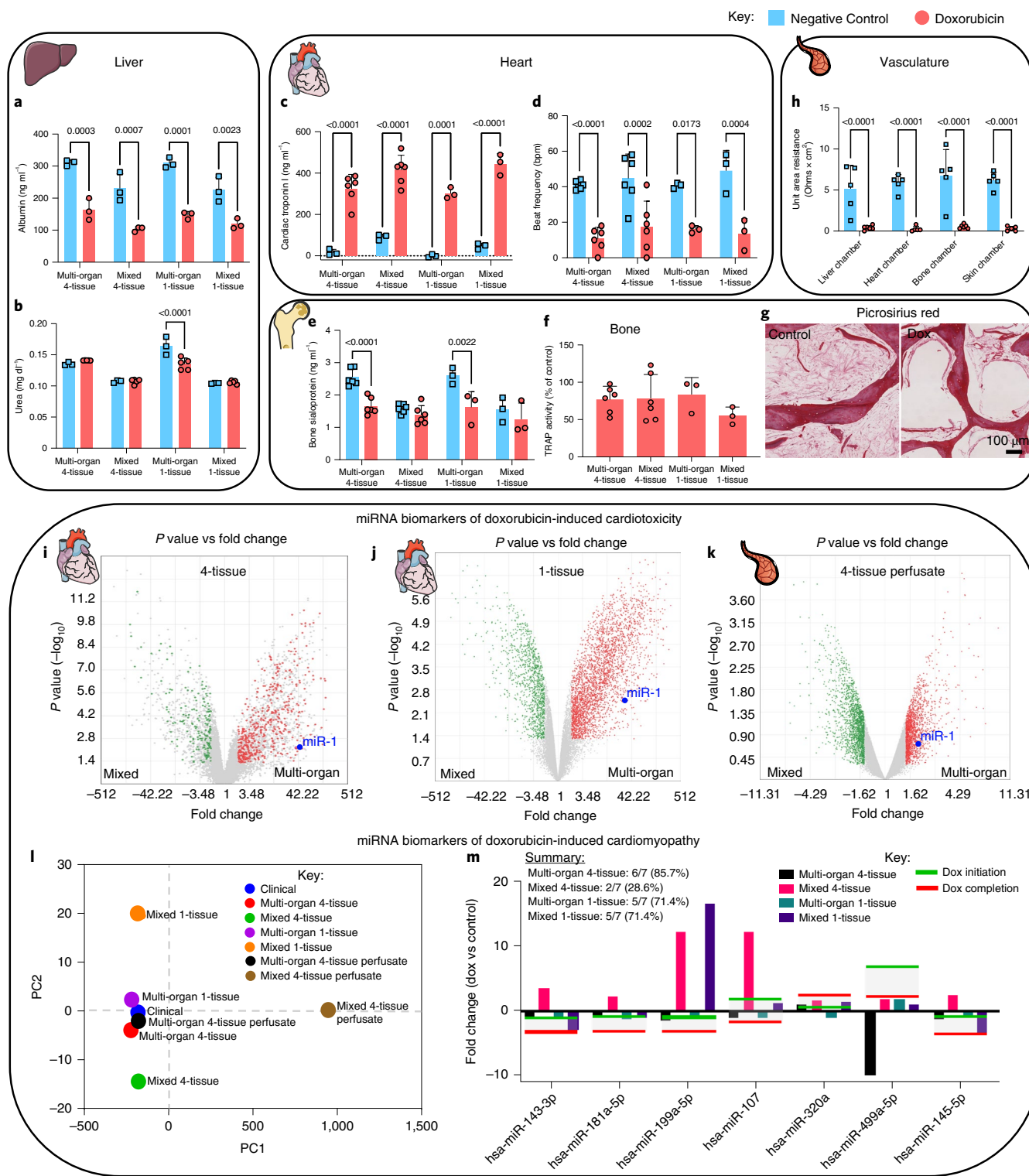


Fig. 7 | PD model of doxorubicin toxicity in the Multi-organ tissue chip. a, b, Liver-specific measurements of albumin (a) and urea (b) secretion after 72 h ($n=3-5$ biological replicates). **c, d,** Cardiac-specific measurements of cardiac troponin secretion (c) and cardiac contractility (d) after 72 h ($n=3-6$ biological replicates). **e-g,** Bone-specific measurements of secreted bone sialoprotein (e), TRAP activity (f) and immunohistochemical images (g) after 72 h ($n=3-6$ biological replicates). Scale bar, 100 μm . **h,** Vascular TEER values as a measure of barrier integrity after 72 h ($n=3-5$ biological replicates). **i-k,** Volcano plots detailing significant miRNA fold changes after doxorubicin treatment between the Multi-organ and Mixed tissue chips for cardiac tissues cultured in the presence of the other 3 tissues (i), in isolation as single tissues (j) or perfusate from the 4-tissue Multi-organ and Mixed conditions (k). **l, m,** Principal component analysis of miRNA fold changes (l) and tissue chip-specific depiction of miRNA fold changes (m) after doxorubicin exposure for clinically relevant miRNAs (shaded region on graph) identified in doxorubicin-induced cardiomyopathy within paediatric patients¹⁶. Data shown as mean \pm s.d. and statistics determined by two-way ANOVA.

17 miRNAs (23.5%) (Supplementary Fig. 12)¹⁶. Overall, the Multi-organ tissue chip outperformed the Mixed tissue chip, as evidenced by stronger clustering with clinical data (Fig. 7m), and enrichment scores and fold changes that are more consistent with those seen clinically (Fig. 7i–k, and Supplementary Figs. 11 and 12).

A set of miRNAs that were related to doxorubicin cardiotoxicity in adult clinical study were evaluated similarly in the multi-tissue tissue chips (Supplementary Fig. 10d,e) and the Isolated tissues (Supplementary Fig. 11d,e)¹⁹. We observed highly significant activity of miR-1273a, reported as a central regulator of pathways related to doxorubicin-induced heart failure in adult patients, in the Multi-organ tissue chip (FC = -45.23, NES = -43.24, $P = 3.3 \times 10^{-19}$) (Supplementary Figs. 10d,e and 11d,e)¹⁹.

Overall, the Multi-organ tissue chip presented substantial activation or inactivation (by GSEA) consistent with clinical data for 10 of 17 miRNAs (Supplementary Fig. 10). The Isolated heart tissue with endothelial barrier presented a similar consistent response (Supplementary Fig. 11). In contrast, in the Mixed tissue chip, all 17 miRNAs showed differential activity. However, only 5 were in agreement with published results (29.4%), while 12 showed differential activities opposite to clinical observation (Supplementary Fig. 10). These data suggest significant effects of multi-organ communication, endothelial-mediated partitioning and metabolic processing of the drug on treatment responses to doxorubicin.

Discussion

The Multi-organ tissue chip maintained the matured phenotypes of distinctly different human tissues (heart, liver, bone, skin) linked by vascular flow, over 4 weeks of culture. The endothelial barrier provided each tissue to be cultured with its own optimized environment while enabling communication by cytokines, circulating cells and exosomes. These conditions allowed recapitulation of clinical PK/PD profiles of doxorubicin and miRNA biomarkers of cardiotoxicity. We believe that further studies of the Multi-organ tissue chip may lead to patient-specific models of systemic pathologies for testing new therapies and early biomarkers of drug toxicity.

However, this tissue chip also has limitations. Several important organs that can influence drug PK/PD (kidney, gut, fat) are not included, while their functions are important for studies of drugs acting systemically. Future work should also continue validating the model with different routes of administration, dosing schemes, metabolism and elimination for doxorubicin and other drugs. For example, skin tissue in the tissue chip allows PK/PD studies of topical drugs and environmental compounds.

We observed lower concentrations of doxorubicin in the heart chamber, presumably due to its absorption by the polydimethylsiloxane (PDMS) pillars. In future studies, such unwanted drug absorption could be reduced by coating or chemically modifying the PDMS surface. Because the focus was on predicting doxorubicin-induced cardiomyopathy, we chose a single high dose clinically shown to be the main causative factor associated with doxorubicin-induced cardiomyopathy. However, evaluating the effects of lower doses delivered over long periods of time and different drug formulations is of high importance for future studies.

Furthermore, the Multi-organ tissue chip would greatly benefit from multiplexing and standardization to better control multi-tissue homeostasis, drug delivery and sampling, and obtain more robust quantitative readouts. To increase translation, future work should adopt a more scalable version of the tissue chip on a 96-well plate footprint, to allow automated handling and compatibility with existing high-content imaging systems and instrumentation.

An interesting observation was that the endothelial barrier, one of the defining components of the tissue chip, maintained its permeability in heart, skin and bone compartments and decreased it in the liver compartment. This change is in line with the high

permeability of liver endothelium, but also indicates that the initial endothelium has plasticity that should be further investigated.

Vascular barriers enabled recapitulation of clinically relevant PK/PD profiles, as only the Multi-organ tissue chip showed clinically relevant biomarkers of doxorubicin cardiotoxicity (miR-1)¹⁴ and cardiomyopathy¹⁶. Linking tissues by vascular flow markedly increased the specificity of cardiac miRNA biomarker changes aligning with those seen clinically¹⁶, with the Multi-organ 4-tissue tissue chip showing a specificity of 81.8% versus 40% for the Mixed tissue chip. The need for connecting multiple tissues to reproduce clinical predictions was further supported by the most differentially expressed miRNA in the Multi-organ tissue chip, hsa-miR-1273a (ref. 19).

This study suggests that the Multi-organ tissue chip can serve as a patient-specific model for developmental testing of new therapeutic regimens and biomarkers of drug toxicity, on the basis of its ability to maintain the biological fidelity of each tissue while also allowing their communication. Medium separation is particularly important for tissues derived from hiPSC, which maintain some developmental plasticity and are not fully matured. The endothelial barrier between the tissues and vascular flow promotes physiological cell and tissue responses due to the paracrine signalling, selective transport of drugs and secreted factors, and immune cell extravasation. Interestingly, the role of the endothelial barrier was more pronounced with the increased biological complexity of the 4-tissue tissue chip compared with the single-tissue tissue chip. However, there is much more to be learned in continued studies of human Multi-organ tissue chips.

Methods

Multi-tissue chip. Tissue chip design. The Multi-organ tissue chip is designed to support the culture and communication of multiple types of engineered tissues, each maintained within its own optimal medium. Tissue communication occurs via recirculating vascular medium across an endothelium that serves as a selectively permeable barrier. The tissue chip is sized to fit onto a standard glass microscope slide. It has a modular design, with four culture chambers that can each contain 1.5 ml of tissue-specific medium, and a reservoir for the recirculating vascular medium. Two ports and a channel enable recirculation of vascular medium via a peristaltic pump. A glass slide at the bottom enables real time imaging. Each chamber has an insert with a porous nylon mesh serving as a substrate for the endothelial layer.

Tissue chip fabrication. The tissue chip has four different components: (1) a body with the tissue chambers, media reservoir and flow channel, (2) two clamps, (3) an O-ring and (4) a glass slide at the bottom. The body was fabricated from polysulfone (McMaster-Carr) using a 3-axis computer numerical control (CNC) milling machine (Haas OM2). The clamps and tubing transfer lid, a secondary spacer between the cell culture dish and the lid to pass tubing in and out without introducing gaps, were machined in the same manner from polycarbonate (McMaster-Carr). The nylon mesh inserts were made via overmoulding using an injection moulding machine (A.B. Plastic Injectors, AB-200) and polypropylene thermoplastic (Flint Hills Resources, P9M7R-056). An aluminum tool (McMaster-Carr, alloy 7075) was CNC-machined for this process and porous nylon meshes with different pore sizes (Millipore) were laser cut into 11 mm circles using a 30 W CO₂ laser (ULS VersaLaser 3.50). The meshes were clamped into a multi-cavity aluminum tool, and polypropylene was injected to form the structure of the mesh insert. An O-ring was installed around the structure to provide a seal (Viton, dash 011, 60 A durometer, McMaster-Carr).

The remaining components of the tissue chip are off-the-shelf: 100 mm cell culture dish, 1 × 25 × 75 mm glass slide, Pharmed BPT tubing (1.6 mm inner diameter, Cole-Parmer, EW-96880-03; and 2.29 mm inner diameter, Pharmed, Cole-Parmer, EW-95714-44), 3-way stopcock valve (Smiths Medical, ASD MX9311L), Luer elbow (Cole-Parmer, EW-45508-84), male and female polypropylene connectors (Cole-Parmer EW-45518-00 and EW-45508-00, respectively), O-rings (McMaster-Carr, 1283N47) and a peristaltic pump (Cole-Parmer, EW-07557-00 and EW-07519-25). Connections between tubing components were made with appropriately sized barbed Luer connectors (polypropylene, Cole-Parmer, EW-50621-95). Post-fabrication, the tissue chip components were subjected to ultrasonic cleaning and autoclaving on a dry cycle.

Tissue chip assembly. Tissue chip components were removed from sterile packaging in a biosafety cabinet. A standard glass microscope slide was placed onto the bottom surface of the polysulfone body using a silicone O-ring. Two polycarbonate

clamps were press-fit around the slide, silicone O-ring and tissue chip to provide a compression seal. Luer elbows were press-fit into Luer-taper ports at both ends of the tissue chip. A loop of Pharmed tubing was attached to a peristaltic section and a 3-way valve to connect the Luer elbows at the inlet and outlet ports. The entire assembly was inserted into a 100 mm cell culture dish and a tubing transfer lid was placed on top. Tubing was installed into the slots of the lid, while a standard lid was used to protect the tissue chip from above. With the tubing assembly completed, 12 ml of endothelial medium was infused via the Luer lock and 3-way valve to prime the flow loop and remove air. Once primed, the endothelialized mesh inserts were installed into each tissue chamber, and the assembled tissue chip was then moved into an incubator and connected to a peristaltic pump.

Estimation of small molecule absorption and diffusive transport. To determine absorption of small molecules by the mesh inserts, FITC-labelled dextran (3 kDa, 10 μ M) was added to a standard cell culture well with a mesh insert. Aliquots were taken over time and assayed for fluorescence on a spectrophotometer (Biotek). To determine diffusion through the mesh inserts, FITC-labelled dextran (3 kDa, 10 μ M) was added to the bottom chamber of a mesh insert, without vascular flow. Aliquots were taken from the top and bottom of the mesh inserts over time and assayed for fluorescence on a spectrophotometer (Biotek). To determine distribution of a small molecule within the tissue chip, FITC-dextran (3 kDa, 10 μ M) was introduced in the reservoir and the tissue chips were connected to a peristaltic pump run at a flow rate of 3.3 ml min⁻¹. Aliquots were taken from different locations in the tissue chip over time and assayed for fluorescence on a spectrophotometer (Biotek).

Culture media. The tissue chip contained 1.5 ml of media in each tissue compartment (liver, heart, bone and skin) and 12 ml of recirculating media. The composition of each medium is summarized in Supplementary Table 2.

Study design. Tissue chip validation over 4 weeks of culture. To validate the tissue chip, we studied four different configurations: (1) Multi-organ system ($n=12$), where the multi-chamber tissue chips contain endothelialized mesh inserts to separate tissue-specific niches from vascular flow; (2) Mixed system ($n=6$), containing mesh inserts without endothelial barrier, allowing tissue and vascular culture media to mix rapidly, a condition equivalent to the use of common media for all tissues; and (3–4) Isolated system ($n=6$), with or without endothelial barrier, with each tissue cultured separately in the same volume of tissue-specific medium (1.5 ml). Conditions (1) and (2) had a perfusate flow channel running on a peristaltic pump with a hydrodynamic shear at the mesh of 1.88 dynes cm⁻². Monocytes (50,000 CD14⁺ cells) were added into the reservoir at the beginning of the experiment and after 14 d. Recirculating flow was maintained for 4 weeks. Every other day, 1 ml of medium was changed in each tissue chamber and in the vascular reservoir; medium samples were immediately frozen at -20°C for subsequent analysis. Similarly, 1 ml of media from Isolated tissues was taken and replenished every other day. At the end of the 4 week study, tissues were collected and sectioned for proteomics (immediately flash frozen) and histology (immediately fixed in 4% paraformaldehyde).

PD and PK models of doxorubicin toxicity. After validating the multi-tissue tissue chip as described above, we modelled doxorubicin's PK/PD. We designed a multi-compartment computational model of the tissue chip for mathematical simulations of absorption, distribution, metabolism and secretion of doxorubicin. We compared the functional and molecular responses of tissues within the Multi-organ tissue chip (doxorubicin exposed $n=6$; negative controls $n=3$), Mixed tissue chip (doxorubicin exposed $n=6$; negative control $n=3$) and Isolated setting (doxorubicin exposed $n=6$; negative control $n=3$, with and without endothelial barrier). All groups were exposed to the same cumulative dose of doxorubicin (30 μ M, 17,400 ng ml⁻¹). In the Multi-organ and Mixed groups, we administered the drug into the reservoir and followed up for the 72 h without media change. Small media samples were collected from the reservoir and the tissue chambers at 1, 24 and 72 h for Ultra-Performance Liquid Chromatography–Mass Spectrometry (UPLC–MS/MS) quantification of non-metabolized drug and its main metabolite. At 72 h, the supernatant was collected, function was assessed for all tissues and the heart tissues were sampled for evaluation of cardiotoxicity by miRNA analysis.

Tissue formation and maturation. Heart. Heart muscle was formed and matured as described previously^{11,38}. Briefly, a ratio of 75% hiPSC-derived CM (WTC-11 cell line, obtained through a material transfer agreement from B. Conklin, Gladstone Institute) were combined with 25% normal human dermal fibroblasts (NHDF, Lonza) in 84 μ l 33.3 mg ml⁻¹ human fibrinogen (Sigma-Aldrich, F3879) and cross-linked with 16 μ l 100 U ml⁻¹ thrombin from human plasma (Sigma-Aldrich, T6884) to form a hydrogel between two flexible pillars. After 20 min of cross-linking at 37 $^{\circ}\text{C}$ in 5% CO₂, cardiac medium was added (RPMI 1640; Thermo Fisher, 11875-093; B-27 supplement (serum free, Thermo Fisher, 17504044); ascorbic acid (Sigma-Aldrich, A8960); and penicillin/streptomycin (Gibco by Life Technologies, 15070063)) supplemented with 0.02 mg ml⁻¹ aprotinin (Sigma-Aldrich, A3428). After 1 week of compaction, heart tissues were transferred to the maturation chip where they were subjected to electromechanical

conditioning at a frequency increasing from 2 to 6 Hz (0.33 Hz d⁻¹, biphasic stimulation, 2 ms pulse duration, 4.5 V cm⁻¹ field intensity).

Liver. hiPSC-derived hepatocytes were purchased from Cellular Dynamics (iCell Hepatocytes 2.0) and thawed at room temperature. An AggreWell plate with 400 μ m microwells (STEMCELL Technologies, 34411) was prepared according to the manufacturer's protocol. Hepatocytes (10 million cells) were mixed with NHDF (Lonza, 10 million cells) in hepatocyte culture medium (HCM, Lonza, CC-3198). The dual cell suspension was then added to 20 wells (approximately 500,000 hepatocytes and 500,000 NHDF in each well) with 2 ml HCM per well. After 48 h of culture at 37 $^{\circ}\text{C}$ and 5% CO₂, cell aggregates were collected and encapsulated in fibrin hydrogel formed from fibrinogen (84% of volume) and thrombin (16% of volume). The cells in hydrogel were placed into 48-well tissue-culture-treated plates (Corning), using 200 μ l per well. The hydrogel was allowed to cross-link in a cell culture incubator for 20 min, after which 1 ml HCM supplemented with 0.02 mg ml⁻¹ aprotinin was added. Tissues were allowed to polymerize for at least 48 h before being used in experiments.

Bone. Bovine calf metacarpal joints were purchased in bulk and stored at -40°C (Lampire Biological Laboratories, 19D24003). A band saw was used to cut approximately 4 cm tall trabecular bone sections from the distal end of metacarpals. A CNC milling machine was then used to generate bone cores with a cross-section of 4 \times 8 mm that were cut into 1 mm thick sections using an IsoMet low-speed wafering saw. Each section (4 mm wide \times 8 mm long \times 1 mm thick) was decellularized using our previously established protocols³⁹ to remove all cellular material while preserving the bone matrix composition and architecture. Bone scaffolds were processed in batch by following the following step-wise protocol on an orbital shaker: (1) phosphate buffered saline (PBS) with 0.1% ethylenediaminetetraacetic acid (EDTA) (w/v) for 1 h at room temperature, (2) 10 mM Tris, 0.1% EDTA (w/v) in deionized (DI) water overnight at 4 $^{\circ}\text{C}$, (3) 10 mM Tris, 0.5% sodium dodecyl sulfate (w/v) in DI water for 24 h at room temperature and (iv) 100 U ml⁻¹ DNase, 1 U ml⁻¹ RNase, 10 mM Tris in DI water for 6 h at 37 $^{\circ}\text{C}$. The resulting bone matrix was lyophilized and weighed to ensure that each piece had an appropriate matrix density for cell seeding (12–18 mg per scaffold). For sterilization, bone scaffolds were subjected to 70% ethanol treatment overnight under ultraviolet light, and incubated in Dulbecco's modified Eagle medium (DMEM) overnight.

Bone marrow-derived MSCs (Lonza) or hiPSC-derived MSCs were expanded and seeded into the bone matrix scaffolds using 4 \times 10⁵ cells per scaffold suspended in 40 μ l of medium (DMEM supplemented with 10% (v/v) HyClone foetal bovine serum (FBS), 1% penicillin/streptomycin and 1 ng ml⁻¹ of basic fibroblast growth factor, bFGF), according to established protocols⁴⁰. To differentiate hiPSC (WTC-11 cell line) into MSC, the STEMdiff mesenchymal progenitor kit (STEMCELL Technologies, 0529) was used according to the manufacturer's protocol. The cells were allowed to attach for 2 h in additional medium (DMEM supplemented with 10% (v/v) HyClone FBS, 1% penicillin/streptomycin and 1 ng ml⁻¹ bFGF) overnight. The following day, osteogenic differentiation was initiated by changing to osteogenic medium consisting of low-glucose DMEM supplemented with 1 μ M dexamethasone, 10 mM β -glycerophosphate and 50 μ M L-ascorbic acid-2-phosphate (all from Sigma-Aldrich). Each scaffold was incubated in 1 ml of osteogenic medium, with media changes 3 \times per week for 3 weeks, allowing for the MSC to differentiate into functional maturing osteoblasts.

Primary monocytes were expanded, seeded into the bone scaffolds and differentiated into functional mature osteoclasts using our previously developed protocols⁴¹. Briefly, peripheral blood mononuclear cells were isolated from buffy coats of human blood (fully de-identified samples obtained from the New York Blood Center) by density gradient centrifugation with Ficoll-Paque PLUS (GE Healthcare, 17-1440-02). Following manufacturers' protocols, immunomagnetic isolation of monocytes (Big Easy EasySep Magnet, Stem Cell Technologies, 180001) using negative selection (EasySep human monocyte isolation kit, Stem Cell Technologies, 19359) was performed. For the following 2 d, 8 \times 10⁶ monocytes were cultured on 25 cm² ultra-low attachment flasks (Corning, 3815) with 10 ml maintenance medium (RPMI 1640, ATCC, 30-2001) supplemented with 10% heat-inactivated human serum (Corning, 35-060), 1% penicillin/streptomycin and 20 ng ml⁻¹ recombinant human macrophage colony-stimulating factor (M-CSF, PeproTech, 300-25) at 37 $^{\circ}\text{C}$ in a humidified incubator at 5% CO₂. Human CD14⁺ monocytes were then seeded at a concentration of 4 \times 10⁵ cells in 40 μ l medium per scaffold, allowed to attach for 2 h at 37 $^{\circ}\text{C}$ in a humidified incubator at 5% CO₂, and subsequently differentiated for 2 weeks into osteoclasts in minimum essential medium Eagle - alpha modification (α -MEM, Sigma, M4526) supplemented with 10% (v/v) heat-inactivated HyClone FBS, 1% penicillin/streptomycin, l-glutamine (Gibco, 25030-081), 20 ng ml⁻¹ recombinant human M-CSF (PeproTech, 300-25) and 40 ng ml⁻¹ recombinant human sRANK ligand (PeproTech, 310-01). Cytokines were replenished every 3 d. Cells were maintained at 37 $^{\circ}\text{C}$ in a humidified incubator at 5% CO₂.

Skin. Skin tissues were formed following a previously described protocol²². Briefly, 1.5 \times 10⁷ NHDF were embedded in 1 ml 3 mg ml⁻¹ type I collagen matrix (Millipore, 08-115), and the polymerized cell-containing hydrogel was incubated

on a transwell mesh (BD Biosciences) for 5–7 d in DMEM supplemented with 10% FBS. Then, 2.5×10^5 keratinocytes were seeded onto the matrix, and incubated in epidermalization medium containing a 3:1 mixture of DMEM and HAM'S F-12, 0.1% FBS, 2 nM triiodothyronine (T3, Sigma, T5516), 5 ng ml⁻¹ insulin (Sigma, I9278), 0.4 µg ml⁻¹ hydrocortisone (Sigma, H0888) and 10 ng ml⁻¹ epidermal growth factor (Millipore, 01-107) for an additional 6 d to ensure keratinocytes were confluent enough to cover the surface. The composite culture was raised to the air-liquid interface for 7 d in a cornification medium with high calcium concentration (1.8 mM) without growth factors to induce epidermal differentiation. By culturing skin tissues on top of a floating device inside the tissue chamber in the Multi-organ tissue chip, we were able to maintain the air-liquid interface over the entire duration of the experiment.

Endothelial barriers. To optimize the hydrodynamic shear stress, we tested three different conditions: zero stress, 1.88 and 6.27 dynes cm⁻². The barriers were prepared as described below and exposed to incrementally increasing shear stress: 0.5 dyne cm⁻² for 12 h, 1.0 dyne cm⁻² for 24 h, 1.88 dynes cm⁻² for 24 h and 6.27 dynes cm⁻² for 48 h. Overall, we determined that a maximum shear stress rate of 1.88 dynes cm⁻² was the most ideal and subsequently used the following protocol for endothelial tissue formation within the studies described herein: 0.5 dyne cm⁻² for 12 h, 1.0 dyne cm⁻² for 24 h, 1.88 dynes cm⁻² for 24 h.

We also optimized the pore size of the nylon mesh by testing four different sizes (5, 10, 20 and 40 µm) and prepared the endothelial barrier in them as described below. Custom mesh inserts were fabricated as described above, autoclaved on a wet cycle, coated with fibronectin (1:100 from 10 µg ml⁻¹ stock, Sigma-Aldrich, F4759) for 45 min and washed twice with PBS. Overall, we determined that 20 µm pore size was the largest pore size we could reliably use to establish confluent endothelial barriers, promote cell-mediated communication and minimize substrate area, and subsequently used these 20-µm-pore-size transwells for all studies.

Human MSCs were expanded in monolayers, dissociated with trypsin between passages 5 and 8, and seeded using 150,000 cells in 50 µl volume to the top of each insert. The MSC suspension (50 µl) was left on each mesh insert for 1 h to enable cell attachment. After 1 h, additional medium was added to each well (2 ml per well), fully immersing the cell-coated meshes within the wells of the ultra-low attachment plate (Corning, 3473), and the suspension was cultured at 37 °C with 5% CO₂ for 24 h.

Human umbilical venous endothelial cells (hUVECs) were expanded to passages 5 to 8. To differentiate hiPSC (WTC-11 cell line) into endothelial cells, the STEMdiff endothelial differentiation kit (STEMCELL Technologies, 08005) was used according to the manufacturer's protocol. Within this study, hUVECs were used for all data, except for Fig. 3e–l where hiPSC-derived endothelial cells from the WTC-11 hiPSC line were used to derive cells for all tissues to demonstrate the tissue chip's utility in 'patient-on-a-chip' models (that is, using the same genetic background for all tissues). The bottom surface of each MSC insert was coated with 400,000 hUVECs and an additional 50,000 MSCs. To this end, the MSC medium was removed, allowing for each insert to stay only slightly hydrated and flipped over to the bottom side. A 20 µl cell suspension of hUVEC/MSC was added twice, 15 min apart, to the bottom surface of each insert and incubated at 37 °C and 5% CO₂ in between the two cell additions, allowing for incremental attachment of cells before addition of endothelial media (EGM-2, Lonza, CC-3162). Each insert was estimated to have a total of 400,000 hUVECs and 200,000 MSCs to mimic the dynamics between vascular populations, represented by the endothelium and perivascular supporting cells (pericytes) in blood vessels. After 48 h, mesh inserts with adherent cells were placed into the tissue chips and exposed to hydrodynamic shear stress of 0.5 dyne cm⁻² for 12 h, 1 dyne cm⁻² for 24 h and 1.88 dynes cm⁻² for 24 h. Shear stress at the endothelial layer was modelled using SOLIDWORKS flow simulation software.

Immune cells. To differentiate hiPSC (WTC-11 cell line) into monocytes, the STEMdiff monocyte kit (STEMCELL Technologies, 05320) was used according to the manufacturer's protocol. Primary human CD14⁺ monocytes were isolated using magnetic activated cell sorting (MACS) with CD14⁺ sorting beads (Miltenyi Biotec) from a human leukopak (New York Blood Center). The isolated cells were maintained in a buffer solution on ice for <3 h before introduction into the tissue chip. Primary or hiPSC-derived CD14⁺ monocytes (50,000 cells) were introduced into the reservoir and circulated through the tissue chip for the duration of the experiment. After 2 weeks of the 4-week experiment, monocytes were replenished by introducing an additional 50,000 CD14⁺ cells into circulation through the reservoir.

CD63 exosome cross-talk. HiPSC-derived CM were transfected with a pCT-CD63-GFP exosome Cyto-Tracer (System Biosciences, CYT0120-VA-1). Due to decreased expression of transfected hiPSC after their differentiation into cardiomyocytes, cells were transfected at day 12 of the hiPSC-derived CM differentiation and directly used to make heart tissues. The CD63-GFP label was tracked using the IVIS Spectrum optical imaging system (PerkinElmer) at Columbia University's Oncology Precision Therapeutics and Imaging Core. Engineered tissues were placed next to each other in the same field of view

and compared directly with multiple imaging views (top, side) using an IVIS 200 Spectrum device. The IVIS Living Image software was used to convert the signal to the normalized radiant efficiency (emission light (photons s⁻¹ cm⁻² sr⁻¹); excitation light (µW cm⁻²)). Fluorescence was measured by selecting the same region of interest for each tissue and quantifying the sum of the radiant efficiencies of all fluorescent pixels within the region of interest. Exported images showing the radiant efficiencies as a heat map were generated within the IVIS Living Image software (PerkinElmer).

Cryo-injury studies. Vascularized Multi-organ tissue chips were assembled as described above, and each tissue chip contained two heart tissues in two middle chambers, with the first and last chamber remaining empty. One of the two heart tissues was exposed to cryoinjury by dry ice for 5 s, while the other served as a control. Immune cells (200,000 CD14⁺ monocytes) were labelled with Vybrant DiD cell-labelling solution (Thermo Fisher) to enable tracking, introduced into the reservoir and circulated in the tissue chip. The tissue chips were maintained for 7 d without media change, and the heart tissues were imaged with an IVIS Spectrum optical imaging system (PerkinElmer) at Columbia University's Oncology Precision Therapeutics and Imaging Core. For imaging, the heart tissues were removed from the Multi-organ tissue chip to avoid autofluorescence. The healthy and injured tissues were aligned next to each other in the same field of view and compared directly in multiple imaging views (top, side) using the IVIS 200 Spectrum device. The IVIS Living Image software (PerkinElmer) was used to analyse the images by converting the signal to the normalized radiant efficiency (emission light (photons s⁻¹ cm⁻² sr⁻¹)/excitation light (µW cm⁻²)). The fluorescence was measured by selecting the same region of interest for each tissue and subsequently quantifying the sum of the radiant efficiencies of all fluorescent pixels within the region of interest. Exported images showing the radiant efficiencies as a heat map were generated within the IVIS Living Image software (PerkinElmer).

Supernatant and functional assays. Supernatant samples were collected from each chamber and reservoir, frozen immediately, and subsequently thawed and used for several assays as described below. Over 4 weeks of culture in the tissue chip, 1 ml of supernatant was sampled every 2 d, while for the doxorubicin experiments 100 to 250 µl samples were taken at different timepoints (1, 24 and 72 h). Supernatant samples were stored at -20 °C for less than 3 months before use; once thawed, no supernatant sample was left at 4 °C for more than 2 days and thawed no more than two times.

Cytokine profiles. CCL20 and CXCL12 readings were obtained from 50 µl of tissue supernatant taken after 28 d of culture using the immune monitoring 65-Plex Human ProcartaPlex panel (Thermo Fisher, EPX650-10065-901) according to the manufacturer's instructions. Samples were allowed to incubate overnight at 4 °C, run on a Luminex-200 and analysed by Luminex software by comparing to the included standards.

Heart function assays. Cardiac excitability, force and beat rate were obtained using our previously established protocols^{11,38}. Cardiac troponin I secretion was determined using the Human Cardiac Troponin I ELISA kit (Abcam, ab200016) according to the manufacturer's instructions.

Liver function assays. To assess liver function, supernatant samples were analysed for albumin and urea secretion using a Human ELISA kit (Bethyl, E88-129) and a Urea Nitrogen test kit (Thermo Fisher, SB-0580-250), respectively. Assays were performed according to the manufacturer's instructions.

Bone function assays. To assess the bone's ability to remodel its matrix, supernatant samples were analysed for TRAP activity (Kamiya Biomedical, KT-008) and bone sialoprotein (Mybiosource, MBS261861) after 28 d of culture. These assays were performed according to the manufacturer's instructions. Micro-computed tomography was performed within the OPTIC core using the Quantum FX micro-computed tomography imaging system (PerkinElmer). Bones were placed within 48-well plates and 4 wells were imaged at a time.

Skin function assays. To assess the TEER of skin tissues, we used a tissue resistance measurement chamber (EndOhm, World Precision Instruments). Each chamber contained a pair of concentric electrodes providing accurate resistance measurements, according to the manufacturer's protocol. We recorded 2–3 technical replicates per tissue and calculated the tissue resistance by multiplying the measured resistance (Ohm) with the effective tissue area (cm²).

Endothelial barriers. To assess the TEER of endothelial barriers, we used the tissue resistance measurement chamber (EndOhm, World Precision Instruments) described above. We recorded 2–3 technical replicates per barrier, and calculated the barrier resistance from the measured resistance (Ohm) and the effective barrier area (cm²). To assess dextran diffusion through the barrier, two different sizes of FITC-dextran (3 kDa, D3307; 70 kDa, D1864; Thermo Fisher) were added to the reservoir of tissue chips containing endothelial barriers that were prepared as described above. Chips were connected to the peristaltic pump and medium

was sampled from each chamber (at 0, 1, 2, 6, 12, 24 and 48 h) to measure the fluorescent signal by a spectrophotometer (BioTek, Synergy HTX). According to the previously reported method⁴¹, permeability was calculated using the equation: $Pe = \frac{C_t \times V}{C_0 \times A \times \Delta t}$ where C_t is the concentration in tissue chambers, C_0 is the initial concentration, V is the volume of the media within the vascular chamber, A is the area of the membrane with cells and Δt is the assay time.

End-point assays. *Tissue preparation.* Tissue samples were bisected for proteomic and histologic analyses. One half of the sample was snap frozen using liquid nitrogen and stored at -80°C for <1 month before being analysed for proteomics. The second half of each tissue sample was fixed for 24 h in paraformaldehyde, washed in PBS and submitted to the Herbert Irving Comprehensive Cancer Center (HICCC) Molecular Pathology Lab at Columbia University for paraffin embedding and sectioning.

Immunostaining. Heart, bone, liver and skin constructs were fixed in 4% paraformaldehyde for 24 h, embedded in paraffin and sectioned for histological and immunofluorescence examination at $5\ \mu\text{m}$. All tissues were processed for hematoxylin & eosin (H&E) staining and trichrome and bone tissues were processed for picosirius red staining by the HICCC Molecular Pathology Lab at Columbia University. Paraffin-embedded tissue blanks were hydrated, processed for antigen-retrieval using a 10 mM sodium citrate buffer for 20 min in heat and permeabilized with 0.25% (v/v) Triton X for 20 min. Samples were then blocked for 2 h with 10% FBS and stained as follows. Heart samples were incubated with a primary antibody for actinin alpha 2 (1:100, Invitrogen, 701914) overnight at 4°C . Liver samples were incubated with primary antibodies for albumin (1:100, Thermo Fisher, A80-229F) and cytochrome P450 enzyme CYP3A4 (1:50, Millipore, AB1254) overnight at 4°C . Bone samples were stained using the TRAP staining kit (Kamiya Biomedical, KT-008) according to the manufacturer's directions. Bone samples were also incubated with an antibody for bone sialoprotein II (1:500, Millipore Sigma, AB1854) and osteocalcin (1:500, Millipore Sigma, AB10911). Skin samples were incubated with primary antibodies for keratin 14 (1:100, Biogenex, PRB-155P) and vimentin (1:100, Santa Cruz Biotechnology, sc-6260) overnight at 4°C . After washing with PBS, samples were incubated with fluorophore-conjugated secondary antibodies (1:200, Invitrogen, A-11012) for 2 h at room temperature. Slides were covered with cover-slips using mounting medium containing 4',6'-diamidino-2-phenylindole (DAPI) (Prolong Mountant with NucBlue, Invitrogen, P36981) and examined using either a Zeiss LSM 5 Exciter confocal laser scanning microscope or Nikon Ti Eclipse inverted confocal microscope.

Endothelial layers were fixed in paraformaldehyde at 37°C for 2 min. After aspirating the fixation solution, samples were washed delicately using PBS supplemented with 1 mM CaCl_2 and 0.5 mM MgCl_2 . Samples were subsequently permeabilized using 0.5% Triton X-100 at 37°C for 10 min. Once washed using supplemented PBS, endothelial barriers were stored at 4°C for less than 3 weeks before staining. For staining, a dilution of 1:250 for VE-cadherin (Sino Biological, 10433-MM01, or Abcam, ab33168) and F-actin (Thermo Fisher, Alexa Fluor 647 phalloidin) in 2% BSA was added to each sample at 4°C overnight. Samples were subsequently washed with supplemented PBS three times for 5 min each. For secondary staining, goat anti-mouse (1:400, Thermo Fisher, A-11029) in 2% BSA, phalloidin (1:400, Thermo Fisher, A30106), and DAPI (1:1000, Thermo Fisher, D1306) were added to each endothelial barrier sample. Samples were kept in the dark on a shaker overnight and washed three times for 5 min each the next day before imaging.

RNA sequencing. Engineered heart tissues were flash frozen in RNAlater (Thermo Fisher, AM7021) and sent to GENEWIZ for standard RNA-seq with polyA selection using an Illumina HiSeq, 2×150 bp configuration, single index per lane and subsequent analysis as described below. Sequence reads were trimmed to remove possible adapter sequences and nucleotides of poor quality using Trimmomatic v.0.36. The trimmed reads were mapped to the *Homo sapiens* GRCh38 reference genome available on ENSEMBL using the STAR aligner v.2.5.2b (a splice aligner that detects splice junctions and incorporates them to help align the entire read sequences) to generate BAM files. Unique gene hit counts were calculated using featureCounts from the Subread package v.1.5.2. Only unique reads that fell within exon regions were counted. The gene hit counts table was used for downstream differential expression analysis.

Using DESeq2, gene expressions were compared between the 'control' tissues (engineered heart tissues cultured for 4 weeks without electromechanical stimulation) and 'matured' tissues (engineered heart tissues cultured for 4 weeks with electromechanical stimulation at a frequency increasing from 2 to 6 Hz at 0.33 Hz per day¹¹). The Wald test was used to generate P values and \log_2 (fold changes). Genes with $P < 0.05$ and absolute \log_2 (fold change) > 1 were selected as differentially expressed genes for each comparison. The differentially expressed genes bi-clustering heat map was generated to visualize the expression profile of the top 30 genes sorted by their adjusted P values, and identify co-regulated genes across the treatment conditions.

A volcano plot was generated to include only the most statistically significant differentially expressed genes and show the global transcriptional change across the groups. All genes were plotted, with each datapoint representing a gene. The

\log_2 (fold change) of each gene (x axis) was plotted against the \log_{10} of its P value (y axis). Genes with $P < 0.05$ and a \log_2 (fold change) > 1 , indicated by red dots, represented upregulated genes. Genes with $P < 0.05$ and a \log_2 (fold change) < 1 , indicated by blue dots, represented downregulated genes.

GSEA. The differentially expressed genes obtained from RNA sequencing of matured heart tissues were ranked from highest to lowest expression and uploaded to GSEA software^{26,42}. Enrichment plots were directly exported from the programme.

IPA. Data were analysed through the use of IPA Networks (QIAGEN, <https://www.qiagenbioinformatics.com/products/ingenuitypathway-analysis>), and the results were exported directly and used without modifications.

Flow cytometry. Before analysis by flow cytometry, the cells were labelled with the following antibodies or dyes: FITC anti-human CD45 antibody (1:100, Biogenex, 304006), Brilliant Violet 605 anti-human CD14 (1:100, Biogenex, 301834), Brilliant Violet 421 anti-human ITGAM (1:100, Biogenex, 301324), PE anti-human CD68 antibody (1:100, Biogenex, 333807), DRAQ5 (1:100, Biogenex, 424101) and anti-troponin T (1:50, Thermo Fisher, BS-10648R) followed by a secondary antibody (1:500, Thermo Fisher, PA1-28834). Cells were measured using a Z55 cell analyser (Bio-Rad) and NovoCyte Quanteon (Agilent) flow cytometer and data were analysed using FlowJo (BD Biosciences).

Quantitative proteomics. Proteomics sample preparation and tandem mass tag (TMT) labelling were performed as described earlier⁴³ with minor modifications. Briefly, frozen tissues were lysed in buffer by bead-beating in 8 M urea, 1% Sodium Dodecyl Sulfate SDS, 200 mM 3-[4-(2-hydroxyethyl)-1-piperazinyl]-1-propanesulfonic acid (EPPS, pH 8.5) and protease inhibitor. Samples were reduced with 5 mM tris(2-carboxyethyl)phosphine (TCEP) and alkylated with 10 mM iodoacetamide that was quenched with 10 mM dithiothreitol (DTT). A total of 50 μg protein was chloroform-methanol precipitated. Protein pellets were reconstituted in 200 mM EPPS (pH 8.5) and protein concentration was determined using a Pierce BCA assay kit (Thermo Fisher, 23225). Total protein from each sample (2–25 μg) was digested overnight at room temperature with Lys-C protease at a 50:1 protein:protease ratio while shaking. Trypsin was added at a 100:1 protein:protease ratio and the samples were incubated for 6 h at 37°C . Digested peptides were quantified using a Nanodrop at 280 nm and 2–25 μg of peptide from each sample were labelled with 200 μg TMT reagent using 10-plex TMT kit. TMT labels were checked by pooling 100 ng of each sample and were mixed at 1:1 across all channels using normalization factor samples. Bulk samples were fractionated using Pierce high-pH reversed-phase peptide fractionation kit (Thermo Fisher, 84868) and each fraction was dried down in a speed vacuum. Dried peptides were dissolved in 10 μl 3% acetonitrile/0.1% formic acid and injected using SPS-MS3.

LC-MS/MS tissue proteomics. Fractioned peptides were separated using Thermo Fisher UltiMate 3000 RSLCnano system and Thermo Fisher EASY-Spray source with Thermo Fisher Acclaim PepMap 100 (2 cm \times 75 μm trap column) and Thermo Fisher EASY-Spray PepMap RSLC C18 (50 cm \times 75 μm internal diameter column) with a 5–30% acetonitrile gradient in 0.1% formic acid over 127 min at a flow rate of 250 nl min^{-1} . After each gradient, the column was washed with 90% buffer B for 5 min and re-equilibrated with 98% buffer A (0.1% formic acid, 100% high-performance liquid chromatography (HPLC)-grade water) for 40 min. For BPRP-separated proteome fractions, the full MS spectra were acquired in the Orbitrap at a resolution of 120,000. The 10 most intense MS1 ions were selected for MS2 analysis. The isolation width was set at 0.7 Da and isolated precursors were fragmented by CID at a normalized collision energy (NCE) of 35% and analysed in the ion trap using 'turbo' scan speed. Following acquisition of each MS2 spectrum, a synchronous precursor selection (SPS) MS3 scan was collected on the top 10 most intense ions in the MS2 spectrum. SPS-MS3 precursors were fragmented by higher energy collision-induced dissociation at an NCE of 65% and analysed using the Orbitrap.

Proteomic analysis. Raw mass spectrometric data were analysed using Proteome Discoverer 2.2 to perform database search and TMT reporter ion quantification. TMT tags on lysine residues and peptide N termini (+229.163 Da) and the carbamidomethylation of cysteine residues (+57.021 Da) were set as static modifications, while the oxidation of methionine residues (+15.995 Da) and deamidation (+0.984) on asparagine and glutamine were set as a variable modification⁴³. Data were searched against the UniProt Human database with peptide-spectrum match and protein-level FDR at 1% FDR. The signal-to-noise measurements of each protein were normalized so that the sum of the signals for all proteins in each channel was constant, to account for equal protein loading. Protein identification and quantification were imported into Perseus⁴⁴ for multiple-sample tests for statistical analysis (FDR < 0.05 or FDR < 0.01) to identify proteins demonstrating statistically significant changes in abundance.

Benchmarking proteomic data for engineered tissues against adult tissues. The identified proteins demonstrating statistically significant changes in abundance were compared to published adult tissue datasets from the Human Protein Atlas⁴⁵.

Because the methodology used to generate each dataset varies greatly, direct comparisons could not be made. Instead, within each tissue dataset, individual protein expression levels were exported into Excel (Microsoft) and subsequently tertiled into 'Low', 'Medium' and 'High' expression levels, as is done in the Human Protein Atlas. Proteins that were not expressed were labelled as 'Not detected' to avoid skewing comparisons with false low counts.

The percent of shared proteins was calculated by determining the number of proteins expressed (at any level) in the engineered tissue dataset versus the published adult tissue dataset, as a percentage of shared proteins (expressed in both tissues) within the total number of proteins⁴⁵. To further determine the correlation of the shared protein expression levels between the engineered tissues and the corresponding published data⁴⁵, the numbers of matching genes expressed as 'Low', 'Medium' or 'High' in both tissue sets were calculated as a percentage over the total number of shared proteins expressed overall.

Heat maps were generated using the tertiled data, by selecting a list of proteins according to two criteria: (1) the protein should be considered 'tissue enriched' by the Human Protein Atlas and (2) the protein should be expressed in both datasets to enable comparisons. The lists of proteins for each heat map were generated using only the proteins listed as highly expressed within each tissue in the Human Protein Atlas. When the suggested protein was not expressed in one of the datasets, we continued down the list until completing data for 15 proteins per tissue. Comparisons between engineered and adult tissues were made according to tissue type, with engineered bone lacking a proper comparison. Bone is deemed a 'rare' tissue by the Human Protein Atlas, and further literature searches did not yield more closely matching datasets; therefore, the protein data for engineered bone were compared to that of adult bone marrow, the closest tissue.

Proteomic data GO, KEGG, differential expression and pathway analysis. The identified proteins demonstrating statistically significant changes in abundance were subsequently used to perform GO and Kyoto Encyclopedia of Genes and Genomes (KEGG) pathway analyses as follows. GO analysis of shared highly expressed proteins in all tissues within each culture condition (Multi-organ, Mixed, Isolated) was performed using ShinyGO v0.6⁴⁶. First, gene lists were assembled using Excel (Microsoft) by filtering for genes (as determined from the corresponding proteins in the description corresponding to each protein accession number) listed as highly expressed in the heart, liver, skin and bone tissues, according to the previous methodology where each dataset was tertiled within Excel (Microsoft). This list was uploaded to the ShinyGO v0.61 server with the following settings: 'Human' as the 'Best matching species', '0.05' as the 'P value cutoff (FDR)', and '30' as the '# of most significant terms to show'.

The resulting networks were directly exported from the site and used without editing. Tissue-specific GO analysis was conducted using PANTHER (Protein Analysis Through Evolutionary Relationships) Classification System⁴⁷ using lists in Excel (Microsoft), by filtering for genes (determined from the corresponding proteins in the description corresponding to each protein accession number) listed as highly expressed in the engineered tissue (for example, heart) for each of the culture conditions (Multi-organ, Mixed, Isolated). The input genes were compared against all genes within the *Homo sapiens* reference list and a PANTHER overrepresentation test for GO cellular component complete was performed using a FISHER test with FDR correction. Further expression analysis for engineered tissues was performed by integrated Differential Expression and Pathway (iDEP) analysis. Here, the protein expression datasets generated for each engineered tissue were uploaded and pathway analysis was performed (using the Human reference dataset) using GSEA for GO Biological Process and KEGG pathways for the top 30 pathways, with a significance cutoff (FDR) of 0.2 and a gene set size minimum between 15 and 2,000⁴⁸.

Drug studies. Cardiac dose response studies. Heart tissues were imaged at baseline and at each sequential dosage for 20 s at 100 frames per second under bright-field illumination using a Zyla 4.2 sCMOS camera (Andor) and NIS-Elements software (Nikon) or Pike F-032b (Allied Vision Technologies) camera. The resulting videos were analysed for pixel movement in a custom MATLAB code described previously³⁸. The resulting traces were used to determine the beat frequency and plot it as a function of increasing dosages to get an EC₅₀ value.

Doxorubicin and doxorubicinol concentrations. Concentrations of doxorubicin and its metabolic product doxorubicinol were measured in cell culture supernatants using a UPLC-MS/MS system at the Biomarkers Core Laboratory, Irving Institute for Clinical and Translational Research (Columbia University). Doxorubicin and doxorubicinol were assayed simultaneously in samples spiked with internal standard (daunorubicin) using Agilent 6410 LC-MS/MS under positive ESI MRM mode (Transitions used: doxorubicin 544.2 > 398.1; doxorubicinol: 546.2 > 400.1). All compounds were quantitated by comparing the integrated peak areas of unknown against those of known amounts of purified standards.

miRNA analysis. miRNA characterization. miRNA was isolated using miRNeasy mini kit (Qiagen, 217004). Samples were shipped on dry ice to Advanced BioMedical Laboratories and assayed using the miRNA 4.0 Genechip array (Thermo Fisher). Results were analysed using the Transcriptome Analysis Console

(TAC) 4.0 software (Thermo Fisher). Additional IPA was performed using the methodology described above.

miRNA GSEA. To assess the activity of miRNAs, we performed one-tail GSEA of their targets, as reported in MultiMiR (release 3.11)⁴⁹ and RBio-miGS (update 0.2.12)⁵⁰ using the R bioconductor packages. Specifically, we assessed whether miRNA targets were enriched in downregulated or upregulated genes after doxorubicin treatment, indicating miRNA activity gain or loss, respectively. As a result, the NES is negative when the miRNA activity increases and positive when its activity decreases. Thus, to avoid confusion, we inverted the NES sign such that a positive or negative NES corresponds to a miRNA activity gain or loss, respectively. Since the analytical form of the null distribution for the NES statistic is not known, P values were computed using an empirical null distribution, generated by random gene shuffling. GSEA was performed using fgsea (v1.13.5)⁵¹ package in R.

Sensitivity and specificity calculations. To assess the sensitivity and specificity of miRNA expression, we calculated whether or not the fold change demonstrated within the Multi-organ or Isolated group was consistent with what was seen clinically^{16,19}. The results were tallied as true positive, false positive, false negative or true negative. From these tallies, the specificity was calculated as described below.

$$\text{Specificity} = \frac{\text{True negative}}{\text{False positive} + \text{True negative}} \times 100$$

Computational modelling. Models of each tissue chip compartment were developed utilizing ODE-based distributed multi-compartment reduced-order models, using CFD Research Corporation's Computational Biology tools. These models were applied to simulate in vitro absorption, distribution, metabolism and excretion of doxorubicin.

General approach. A compartmental mathematical model describing drug transport in various organ segments (fluidic channel, endothelial barrier, membrane, tissue and tank) was derived using the general total fluid mass and species mass balance equations:

$$\frac{\partial \rho}{\partial t} + \nabla \cdot (\rho \vec{u}) = \sum \dot{m} \quad (1)$$

where \vec{u} is the velocity vector, ρ is fluid density, t is time and the right-hand side term is the sum of source inflows and outflows. Despite a constant fluid density assumption, we retained the temporal derivative to enable treatment of time-dependent volumes, as described below. The general species mass balance expressed for a concentration C is given as,

$$\frac{\partial C}{\partial t} + \nabla \cdot (\vec{u}C) = \nabla \cdot (D\nabla C) + S_c \quad (2)$$

where D is the diffusion coefficient and S_c is the generalized source term from chemical reactions. Integrating spatial terms for convection and diffusion into individual fluxes across the computational control volume boundaries and treating these as source terms in the ODE, the above mass and species transport equations can be approximated as:

$$\frac{\partial V}{\partial t} = \sum Q \quad (3)$$

$$V \frac{\partial C}{\partial t} = Q(C_{in} - C) + (J_+ - J_-) + V \times S_c \quad (4)$$

where V is the compartment volume, C is the species concentration inside the compartment, C_{in} is the convective inlet concentration, Q is the volumetric flow rate and J_+ , J_- are the permeation (diffusive) fluxes across the boundaries of the computational control volume (organ device barriers). Because of the convection-dominated flow conditions, streamwise diffusion has been neglected and only transverse fluxes (across barriers) have been retained. Note that the volume integration of the original partial differential equations resulted in a set of ODE.

The transverse flux between two adjacent sub-compartments, F, and endothelial barrier, E, can be expressed as:

$$J = S \frac{1}{\frac{\delta_E}{k_p} + \frac{\delta_F}{D_F}} \left(\frac{C_E}{k_p} - C_F \right) = S \times P_{F-E} \left(\frac{C_E}{k_p} - C_F \right) \quad (5)$$

where S is the fluidic channel-endothelium barrier (F-E) interface area, C_F is the drug concentration in the fluidic compartment, C_E is the concentration in the endothelium barrier compartment, k_p is the partition coefficient, δ_E and δ_F are the half-distances to the F-E interface and P_{F-E} is the effective permeability coefficient. Depending on the compound partition coefficient, k_p , there may be a concentration discontinuity at the fluid-membrane interface. The model also accounts for

drug partitioning into the tubing, tank and reservoir materials for cellular drug metabolism, and for the effects of intake/efflux transporters. Because each tank is subdivided into sub-compartments, V_p in the vertical (tank axis) direction and due to lack of convective flow in the tank, the species mass balance equations in the tank account for vertical diffusion flux as:

$$V_i \frac{\partial C_i}{\partial t} = (J_{i+} - J_{i-}) + V_i \times S_{ci} \quad (6)$$

and:

$$J_{i+} = A_i \frac{D}{\delta_+} (C_{i-} - C_i) \quad (7)$$

$$J_{i-} = A_i \frac{D}{\delta_-} (C_i - C_{i+}) \quad (8)$$

where A is the tank cross-section area, C_{i-} , C_i and C_{i+} , are concentrations in the lower, current and upper sub-compartments, and δ_- and δ_+ are the distances between centres of adjacent sub-compartments. For drug development applications, a set of two or more species conservation equations must be solved for both the primary compound and for its metabolite(s). These sets of equations are coupled via a drug enzymatic transformation reaction term in the cell layers, where a sink term of the primary compound becomes a source term in the metabolite conservation equation. Drug transport and conservation equations may include the compound metabolic clearance term calculated using the organ-specific intrinsic clearance, Cl_{int} , which is typically expressed using the Michaelis–Menten kinetics model:

$$Cl_{int} = \frac{V_{max}}{K_m + C} \quad (9)$$

where V_{max} represents the maximum reaction rate and the Michaelis constant K_m is the compound concentration at which the reaction rate is half of V_{max} ³¹. A detailed description of the mathematical models for each organ chamber is provided in the following sections.

Liver tissue chamber. The compartmental mathematical model describing drug transport and metabolism can be derived using general mass balance equations, with all flux terms integrated over the compartment boundaries. The resultant equations are expressed in the form of a set of ODEs representing the species mass balance in each compartment. A schematic of the liver tissue chamber is shown in Extended Data Fig. 9b. The model accounts for the primary drug (doxorubicin) and its main metabolite (doxorubicinol). In all equations below, doxorubicin is represented by the superscript 1, while doxorubicinol is represented by the superscript 2. The equations are primarily written for doxorubicin, but are also applicable for doxorubicinol, unless stated otherwise. The fluidic channel is separated into two different parts. One portion of the fluidic channel is exactly below the membrane and is called liver fluidic channel (LFC), while the other portion of the fluidic channel called the liver inlet fluidic channel (LIFC) connects the LFC to the tubing. The mass balance equations for the LFC and the LIFC can be written as:

$$V_{LIFC} \frac{dC_{LIFC}^1}{dt} = Q_f (C_{TL,20}^1 - C_{LIFC}^1) \quad (10)$$

$$V_{LFC} \frac{dC_{LFC}^1}{dt} = Q_f (C_{LIFC}^1 - C_{LFC}^1) - J_{LFC-LBM}^1 \quad (11)$$

where C_i and V_i ($i = LIFC, LFC, LBM, TL20$) represent the species concentration and volume of individual compartments, and J_{ij} describes the diffusive flux between compartments i and j . The subscripts TL,20 and LBM represent the last discretized section of the tubing lumen and the bottom layer of the membrane. The flow rate is represented by Q_f .

Endothelial barrier. The endothelial barrier consists of three layers: a nylon mesh and cells on both sides. The top and bottom layers are functionalized and account for drug partitioning. The mass balance equations for the three layers of the membrane can be written as:

$$V_{LBM} \frac{dC_{LBM}^1}{dt} = J_{LFC-LBM}^1 - J_{LBM-LMM}^1 \quad (12)$$

$$V_{LMM} \frac{dC_{LMM}^1}{dt} = J_{LBM-LMM}^1 - J_{LMM-LTM}^1 \quad (13)$$

$$V_{LTM} \frac{dC_{LTM}^1}{dt} = J_{LMM-LTM}^1 - J_{LTM-LBT}^1 \quad (14)$$

where the subscript LMM represents the middle layer of the membrane, LTM represents the top layer of the membrane and LBT represents the bottom layer of the tank.

The tank containing the liver tissue is separated into three layers. The liver tissue is situated in the bottom layer of the tank. The mass balance for the three layers of the tank can be written as:

$$V_{LBT} \frac{dC_{LBT}^1}{dt} = J_{LTM-LBT}^1 - J_{LBT-LMT}^1 - J_{LBT-L}^1 - Q_d C_{LBT} \quad (15)$$

$$V_{LMT} \frac{dC_{LMT}^1}{dt} = J_{LBT-LMT}^1 - J_{LMT-LTT}^1 - C_{LMT}^1 \frac{dV_{LMT}}{dt} \quad (16)$$

$$V_{LTT} \frac{dC_{LTT}^1}{dt} = J_{LMT-LTT}^1 \quad (17)$$

where the subscript LMT represents the middle layer of the tank, LTT represents the top layer of the tank and L represents the liver tissue.

It was experimentally observed that some amount of drug is absorbed by the tissue chip and the tank. The model accounts for the drug loss by including a clearance flow rate term (Q_d) in the bottom layer of the tank. The media is sampled from the middle layer of the tank.

The liver tissue is modelled to metabolize doxorubicin into its metabolite, doxorubicinol. The mass balance equation for the liver tissue can be written as:

$$V_L \frac{dC_L^1}{dt} = J_{LBT-L}^1 - S_{L,met}^{1-2} - C_L S_{L,el}^1 \quad (18)$$

$$V_L \frac{dC_L^2}{dt} = J_{LBT-L}^2 + S_{L,met}^{1-2} - C_L S_{L,el}^2 \quad (19)$$

where $S_{L,met}$ is the metabolic transformation rate of doxorubicin to doxorubicinol and $S_{L,el}$ is the compound elimination rate. The metabolic transformation rate is typically expressed using the Michaelis–Menten kinetics model, given as:

$$S_{L,met}^{1-2} = \frac{V_{max} C_L^1}{K_m + C_L^1} \quad (20)$$

where V_{max} is the maximum reaction rate and the Michaelis constant K_m is the compound concentration at which the reaction rate is half of V_{max} .

The flux terms in the above compartmental mass balance equations are expressed using permeability limiting equations. The diffusive flux terms can be written as:

$$J_{LFC-LBM}^1 = A_M \times P_{LFC-LBM}^1 \left(f_u C_{LFC}^1 - \frac{C_{LBM}^1}{k_p} \right) \quad (21)$$

$$J_{LBM-LMM}^1 = A_M \times P_{LBM-LMM}^1 \left(\frac{C_{LBM}^1}{k_p} - C_{LMM}^1 \right) \quad (22)$$

$$J_{LMM-LTM}^1 = A_M \times P_{LMM-LTM}^1 \left(C_{LMM}^1 - \frac{C_{LTM}^1}{k_p} \right) \quad (23)$$

$$J_{LTM-LBT}^1 = A_M \times P_{LTM-LBT}^1 \left(\frac{C_{LTM}^1}{k_p} - C_{LBT}^1 \right) \quad (24)$$

$$J_{LBT-LMT}^1 = A_T \times P_{LBT-LMT}^1 \left(C_{LBT}^1 - C_{LMT}^1 \right) \quad (25)$$

$$J_{LMT-LTT}^1 = A_T \times P_{LMT-LTT}^1 \left(C_{LMT}^1 - C_{LTT}^1 \right) \quad (26)$$

$$J_{LBT-L}^1 = A_L \times P_{LBT-L}^1 \left(C_{LBT}^1 - \frac{C_L^1}{k_p} \right) \quad (27)$$

where A is the interfacial surface area, P is the permeability, f_u is the unbound fraction of the drug and k_p is the partition coefficient (based on the log(P) value) of the drug). The subscripts represent the associated compartments. The permeabilities are calculated as:

$$\frac{1}{P_{LFC-LBM}^1} = \frac{\delta_{LFC}}{D_{LFC}} + \frac{\delta_{LBM}}{k_p D_{LBM}} \quad (28)$$

$$\frac{1}{P_{LBM-LMM}^1} = \frac{\delta_{LBM}}{k_p D_{LBM}} + \frac{\delta_{LMM}}{D_{LMM}} \quad (29)$$

$$\frac{1}{P_{LMM-LTM}^1} = \frac{\delta_{LMM}}{D_{LMM}} + \frac{\delta_{LTM}}{k_p D_{LTM}} \quad (30)$$

$$\frac{1}{P_{LTM-LBT}^1} = \frac{\delta_{LTM}}{k_p D_{LTM}} + \frac{\delta_{LBT}}{D_{LBT}} \quad (31)$$

$$\frac{1}{P_{LBT-LMT}^1} = \frac{\delta_{LBT}}{D_{LBT}} + \frac{\delta_{LMT}}{D_{LMT}} \quad (32)$$

$$\frac{1}{P_{LMT-LTT}^1} = \frac{\delta_{LMT}}{D_{LMT}} + \frac{\delta_{LTT}}{D_{LTT}} \quad (33)$$

$$\frac{1}{P_{LBT-L}^1} = \frac{\delta_{LBT}}{D_{LBT}} + \frac{\delta_L}{k_p D_L} \quad (34)$$

where δ is the effective thickness of a compartment and D is the diffusion coefficient of the drug in the compartment. The parameters used in the model are given in Supplementary Table 3. All variables used in the computational model and their meaning are described in Supplementary Table 4.

Heart tissue chamber. A compartmental schematic of the heart tissue chamber is shown in Extended Data Fig. 9c. The fluidic channels associated with the heart tissue chamber are named heart inlet fluidic channel (HIFC) and heart fluidic channel (HFC). HFC is situated exactly below the heart tissue chamber's membrane. The top and bottom functionalized layers of the membrane are represented by the acronyms HTM and HBM. The middle layer of the membrane is represented as HMM. The top, middle and bottom layers of the tank are named as HTT, HMT and HBT, respectively. The heart tissue (represented as H) is situated in the middle layer of the tank. The two PDMS pillars supporting the heart tissue are modelled as a single compartment that interacts with the second and third layers of the tank. The mass balance, diffusive flux and permeability calculation equations for the fluidic channels and the membrane layers of the heart tissue chamber are the same as those of the liver tissue chamber. Convective fluid flow brings in drug from the LFC compartment to the HIFC compartment. The main modelling differences in the heart tissue chamber are the position of the heart tissue, inclusion of the PDMS pillars and the absence of metabolism and elimination. Unlike the liver tissue, the heart tissue interacts with the second layer of the tank. The mass balance equations of the bottom, middle and top layers of the tank can be written as:

$$V_{HBT} \frac{dC_{HBT}^1}{dt} = J_{HTM-HBT}^1 - J_{HBT-HMT}^1 - Q_{cl} C_{HBT} \quad (35)$$

$$V_{HMT} \frac{dC_{HMT}^1}{dt} = J_{HBT-HMT}^1 - J_{HMT-HTT}^1 - J_{HMT-H}^1 - J_{HMT-PD}^1 - C_{HMT}^1 \frac{dV_{HMT}}{dt} \quad (36)$$

$$V_{HTT} \frac{dC_{HTT}^1}{dt} = J_{HMT-HTT}^1 - J_{HTT-PD}^1 \quad (37)$$

where the subscript PD represents the PDMS compartment. The diffusive flux exchange between the two layers of the tank and the PDMS pillar is given as:

$$J_{HMT-PD}^1 = A_{PD} \times P_{HMT-PD}^1 \left(C_{HMT}^1 - \frac{C_{PD}^1}{k_p} \right) \quad (38)$$

$$J_{HTT-PD}^1 = A_{PD} \times P_{HTT-PD}^1 \left(C_{HTT}^1 - \frac{C_{PD}^1}{k_p} \right) \quad (39)$$

The permeabilities P_{HMT-PD}^1 and P_{HTT-PD}^1 are calculated in the same manner as given in equation (34). As there is no metabolic transformation or elimination in the heart tissue, the mass balance is given as:

$$V_H \frac{dC_H^1}{dt} = J_{HMT-H}^1 \quad (40)$$

Bone tissue chamber. A schematic of the bone tissue chamber is shown in Extended Data Fig. 9d. The fluidic channels associated with the bone tissue chamber are named as bone inlet fluidic channel (BIFC) and bone fluidic

channel (BFC). BFC is situated exactly below the bone tissue chamber's membrane. The top and bottom functionalized layers of the membrane are represented by the acronyms BTM and BBM. The middle layer of the membrane is represented as BMM. The top, middle and bottom layers of the tank are named as BTT, BMT and BBT, respectively. The bone tissue (represented as B) is situated in the first layer of the tank and on top of the BTM, and is treated as a porous medium composed of fluid, osteoblast cells (OB) and osteoclast cells (OC). The drug is assumed to bind to the receptors on the cells. The fluidic channel is modelled for the convective fluid flow that brings in the drug from the HFC to the BIFC. The mass balance, diffusive flux and permeability equations for the BIFC, BFC, BMM, BBM, BMT and BTT compartments are similar to that of the liver tissue chamber. As the bone tissue is situated directly above the top layer of the membrane, the diffusive flux is modelled for the membrane–bone interface using the following equations for the top layer of the membrane, bottom layer of the tank and bone tissue:

$$V_{BTM} \frac{dC_{BTM}^1}{dt} = J_{BMM-LTM}^1 - J_{BTM-B}^1 \quad (41)$$

$$V_{BBT} \frac{dC_{BBT}^1}{dt} = J_{BBT-B}^1 - J_{BBT-BMT}^1 - Q_{cl} C_{BBT} \quad (42)$$

$$V_B \frac{dC_B^1}{dt} = J_{BTM-B}^1 - J_{BBT-B}^1 - S_{OB}^1 - S_{OC}^1 \quad (43)$$

where S_{OB} and S_{OC} are nonlinear saturable bindings on the cell receptors and can be written as:

$$S_{OB}^1 = k_{OB}^{lf} C_{OB}^1 (C_{OB,max}^1 - C_{OB}^1) - k_{OB}^{lr} C_{OB}^1 \quad (44)$$

$$S_{OC}^1 = k_{OC}^{lf} C_{OC}^1 (C_{OC,max}^1 - C_{OC}^1) - k_{OC}^{lr} C_{OC}^1 \quad (45)$$

where k^{lf} and k^{lr} are the forward and reverse binding rate constants, and $C_{OB,max}$ and $C_{OC,max}$ are the maximum density of the binding sites (receptors).

The mass balance for the receptors can be written as:

$$V_{OB} \frac{dC_{OB}^1}{dt} = S_{OB}^1 \quad (46)$$

$$V_{OC} \frac{dC_{OC}^1}{dt} = S_{OC}^1 \quad (47)$$

Although the current model has the capability to include binding of the drug to the receptors, it is not included for the validation. The S_{OB} and S_{OC} terms are assumed to be zero. The diffusive flux between the top layer of the membrane and the bone tissue (J_{BTM-B}^1), and between the bone tissue and the bottom layer of the tank (J_{BBT-B}^1) can be written as:

$$J_{BTM-B}^1 = A_M \times P_{BTM-B}^1 (C_{BTM}^1 - C_B^1) \quad (48)$$

$$J_{BBT-B}^1 = A_{BBT-B} \times P_{BBT-B}^1 (C_B^1 - C_{BBT}^1) \quad (49)$$

where A_{BBT-B} is the surface area of the bone tissue in contact with the bottom layer of the tank (excludes bottom surface area of the bone tissue). The permeabilities are calculated in a similar manner as described in equation (32), as there will be no drug partitioning when moving from the functionalized top layer of the membrane to the bone tissue.

Skin tissue chamber. The skin tissue chamber is modelled such that the skin tissue (represented as S) rests in the top layer of the tank to maintain an air–liquid interface. The rest of the compartments are modelled in the same way as for the liver tissue chamber. The fluidic channels associated with the skin tissue chamber are named as skin inlet fluidic channel (SIFC) and skin fluidic channel (SFC). The skin tissue chamber has another fluidic channel section named as skin outlet fluidic channel (SOFC) that connects the SFC to the reservoir. SFC is situated exactly below the skin tissue chamber's membrane. The top and bottom functionalized layers of the membrane are represented by the acronyms STM and SBM. The middle layer of the membrane is represented as SMM. The top, middle and bottom layers of the tank are STT, SMT and SBT, respectively.

A compartmental schematic of the skin tissue chamber is shown in Extended Data Fig. 9e. The mass balance, diffusive flux and permeability equations for the SIFC, SFC, SBM, SMM, STM and SMT compartments are similar to that of the liver tissue chamber. The mass balance for the SBT compartment is as described in

equation (35). The fluidic channel is modelled such that the convective fluid flow brings in the drug from the BFC to the SIFC. The mass balance equation for the outlet fluidic channel compartment can be written as:

$$V_{\text{SOFC}} \frac{dC_{\text{SOFC}}^1}{dt} = Q_f (C_{\text{SFC}}^1 - C_{\text{SOFC}}^1) \quad (50)$$

The mass balance equation for the top layer of the tank and the skin tissue can be written as:

$$V_{\text{STT}} \frac{dC_{\text{STT}}^1}{dt} = J_{\text{SMT-STT}}^1 - J_{\text{STT-S}}^1 \quad (51)$$

$$V_s \frac{dC_s^1}{dt} = J_{\text{STT-S}}^1 \quad (52)$$

The interfacial surface area used to calculate the diffusive flux $J_{\text{STT-S}}^1$ excludes the top surface area of the skin tissue as it is in contact with the air and not the medium.

Reservoir and tubing system. The compartmental mathematical model describing the drug transport in the reservoir and tubing is also expressed in the form of a set of ODEs representing the species mass balance in each compartment. The reservoir compartment is assumed to be well mixed and the tubing is discretized into 20 individual sections. The model accounts for the outer PharMed BPT shell around the tubing lumen. A compartmental schematic of the reservoir and tubing model is shown in Extended Data Fig. 9f. The reservoir (RES) is connected to the SOFC compartment from the skin tissue chamber and the first discretized cell of the tubing lumen (TL, 1). The mass balance for the reservoir compartment can be written as:

$$V_{\text{RES}} \frac{dC_{\text{RES}}^1}{dt} = Q_f (C_{\text{SOFC}}^1 - C_{\text{RES}}^1) - C_{\text{RES}}^1 \frac{dV_{\text{RES}}}{dt} \quad (53)$$

The drug transport in the tubing lumen is mainly due to convective fluid flow. The model also accounts for drug absorption by the outer shell of the tubing. The mass balance equation for the first discretized section of the tubing lumen and the first discretized section of the BPT shell (TB, 1) can be written as:

$$V_{\text{TL},1} \frac{dC_{\text{TL},1}^1}{dt} = Q_f (C_{\text{RES}}^1 - C_{\text{TL},1}^1) - J_{\text{TL},1-\text{TB},1}^1 - J_{\text{TL},1-\text{TL},2}^1 \quad (54)$$

$$V_{\text{TB},1} \frac{dC_{\text{TB},1}^1}{dt} = J_{\text{TL},1-\text{TB},1}^1 - J_{\text{TB},1-\text{TB},2}^1 \quad (55)$$

where subscripts TB,2 and TL,2 represent the second BPT shell cell and the second lumen cell, respectively. The mass balance equations for the lumen and the BPT shell cells can be written as:

$$V_{\text{TL},i} \frac{dC_{\text{TL},i}^1}{dt} = Q_f (C_{\text{TL},i-1}^1 - C_{\text{TL},i}^1) + J_{\text{TL},i-1-\text{TL},i}^1 - J_{\text{TL},i-\text{TL},i+1}^1 - J_{\text{TL},i-\text{TB},i}^1 \quad (56)$$

$$V_{\text{TB},i} \frac{dC_{\text{TB},i}^1}{dt} = J_{\text{TL},i-\text{TB},i}^1 + J_{\text{TB},i-1-\text{TB},i}^1 - J_{\text{TB},i-\text{TB},i+1}^1 \quad (57)$$

where TL is tubing lumen and TB is BPT shell. The subscript 'i' corresponds to the respective discretized cell number and can have a value between 2 and 19 (i=2-19). The mass balance equation for the last discretized cell of the lumen and BPT shell can be written as:

$$V_{\text{TL},20} \frac{dC_{\text{TL},20}^1}{dt} = Q_f (C_{\text{TL},19}^1 - C_{\text{TL},20}^1) - J_{\text{TL},20-\text{TB},20}^1 + J_{\text{TL},19-\text{TL},20}^1 \quad (58)$$

$$V_{\text{TB},20} \frac{dC_{\text{TB},20}^1}{dt} = J_{\text{TL},20-\text{TB},20}^1 + J_{\text{TB},19-\text{TB},20}^1 \quad (59)$$

The diffusive flux between adjacent lumen discretized cells can be expressed as:

$$J_{\text{TL},i-1-\text{TL},i}^1 = A_{\text{TL}} \times P_{\text{TL}}^1 (C_{\text{TL},i-1}^1 - C_{\text{TL},i}^1) \quad (60)$$

$$J_{\text{TL},i-\text{TL},i+1}^1 = A_{\text{TL}} \times P_{\text{TL}}^1 (C_{\text{TL},i}^1 - C_{\text{TL},i+1}^1) \quad (61)$$

where ATL is the available interfacial area between two lumen cells and PTL is the drug permeability for the lumen.

The diffusive flux between adjacent BPT shell discretized cells can be expressed as:

$$J_{\text{TB},i-1-\text{TB},i}^1 = A_{\text{TB}} \times P_{\text{TB}}^1 (C_{\text{TB},i-1}^1 - C_{\text{TB},i}^1) \quad (62)$$

$$J_{\text{TB},i-\text{TL},i+1}^1 = A_{\text{TB}} \times P_{\text{TL}}^1 (C_{\text{TB},i}^1 - C_{\text{TL},i+1}^1) \quad (63)$$

where ATB is the available interfacial area between two BPT shell cells and PTB is the drug permeability for the BPT shell.

The diffusive flux between the lumen cell and the BPT shell cell can be expressed as:

$$J_{\text{TL},i-\text{TB},i}^1 = A_{\text{TLB}} \times P_{\text{TLB}}^1 \left(C_{\text{TL},i}^1 - \frac{C_{\text{TB},i}^1}{k_p} \right) \quad (64)$$

where ATLB is the available interfacial area between the lumen cell and the BPT shell cell, and PTLB is the drug permeability for the lumen-BPT shell interface.

The drug permeability for the lumen and for the BPT shell can be calculated as described in equation (32). The drug permeability for the lumen-BPT shell interface can be calculated as described in equation (28).

Non-endothelialized model. The non-endothelialized model (Mixed condition) is based on the primary model of the entire tissue chip. The equations representing the species mass balance, diffusive flux and permeabilities for the reservoir, tubing, inlet fluidic channels, second and third layer of the tank (including first layer of the tank for the bone tissue chamber), and the tissue compartments (except for the bone tissue) are expressed as previously described for the entire tissue chip model. In this model, the nylon mesh separating the tank from the fluidic channel consists of a single layer. The top and bottom functionalized layers of the membrane are removed and thus the membrane does not account for the drug partitioning. In the liver, heart and skin tissue chambers, the nylon mesh is directly in contact with the first layer of the tank, therefore the changed equations are similar for all of them.

A generalized compartmental schematic is shown in Supplementary Fig. 6d. The compartments for which the equations are the same as the primary model are not included in the schematic. For this model, the bottom layer of the tank, membrane and the fluidic channel below the membrane are represented by the acronyms BT, MM and FC, respectively. The mass balance equations for these compartments can be written as:

$$V_{\text{FC}} \frac{dC_{\text{FC}}^1}{dt} = Q_f (C_{\text{IFC}}^1 - C_{\text{FC}}^1) - J_{\text{FC-MM}}^1 \quad (65)$$

$$V_{\text{MM}} \frac{dC_{\text{MM}}^1}{dt} = J_{\text{FC-MM}}^1 - J_{\text{MM-BT}}^1 \quad (66)$$

$$V_{\text{BT}} \frac{dC_{\text{BT}}^1}{dt} = J_{\text{MM-BT}}^1 - J_{\text{BT-MT}}^1 - J_{\text{BT-L}}^1 - Q_d C_{\text{BT}} \quad (67)$$

where the subscript IFC represents inlet fluidic channel, MT represents the middle layer of the tank and L represents the liver tissue. The flux JBT-L is only applicable for the liver tissue chamber and is not included for the heart tissue chamber and the skin tissue chamber.

The flux terms in the above compartmental mass balance equations can be written as:

$$J_{\text{FC-MM}}^1 = A_{\text{M}} \times P_{\text{FC-MM}}^1 (f_u C_{\text{FC}}^1 - C_{\text{MM}}^1) \quad (68)$$

$$J_{\text{MM-BT}}^1 = A_{\text{M}} \times P_{\text{MM-BT}}^1 (C_{\text{MM}}^1 - C_{\text{BT}}^1) \quad (69)$$

The diffusive fluxes JBT-MT and JBT-L are same as described previously in equations (25) and (27), respectively. The permeabilities are calculated as:

$$\frac{1}{P_{\text{FC-MM}}^1} = \frac{\delta_{\text{FC}}}{D_{\text{FC}}} + \frac{\delta_{\text{MM}}}{D_{\text{MM}}} \quad (70)$$

$$\frac{1}{P_{\text{MM-BT}}^1} = \frac{\delta_{\text{MM}}}{D_{\text{MM}}} + \frac{\delta_{\text{BT}}}{D_{\text{BT}}} \quad (71)$$

In the bone tissue chamber, the membrane is in contact with the tissue and thus the equations slightly vary from those of the other tissue chambers. The compartmental schematic for the non-endothelialized model of the bone tissue chamber is shown in Supplementary Fig. 6e. The compartments for which the equations are the same as the primary model, are not included in the

schematic. For this model, the bone tissue, membrane and the fluidic channel below the membrane are represented by the acronyms B, BMM and BFC, respectively (similar to the primary model). The mass balance equations for these compartments can be written as,

$$V_{\text{BFC}} \frac{dC_{\text{BFC}}^1}{dt} = Q_{\text{f}} \left(C_{\text{BFC}}^1 - C_{\text{BFC}}^1 \right) - J_{\text{BFC-BMM}}^1 \quad (72)$$

$$V_{\text{BMM}} \frac{dC_{\text{BMM}}^1}{dt} = J_{\text{BFC-BMM}}^1 - J_{\text{BMM-B}}^1 \quad (73)$$

$$V_{\text{B}} \frac{dC_{\text{B}}^1}{dt} = J_{\text{BMM-B}}^1 - J_{\text{BBT-B}}^1 \quad (74)$$

where the subscripts BFC and BBT represent the inlet fluidic channel and bottom tank layer of the bone tissue chamber, respectively.

The flux terms in the above compartmental mass balance equations can be written as:

$$J_{\text{BFC-BMM}}^1 = A_{\text{M}} \times P_{\text{BFC-BMM}}^1 \left(f_{\text{u}} C_{\text{BFC}}^1 - C_{\text{BMM}}^1 \right) \quad (75)$$

$$J_{\text{BMM-B}}^1 = A_{\text{M}} \times P_{\text{BMM-B}}^1 \left(C_{\text{BMM}}^1 - \frac{C_{\text{B}}^1}{k_{\text{p}}} \right) \quad (76)$$

The diffusive flux $J_{\text{BBT-B}}^1$ is same as described previously in equation (49). The permeabilities are calculated as:

$$\frac{1}{P_{\text{BFC-BMM}}^1} = \frac{\delta_{\text{BFC}}}{D_{\text{BFC}}} + \frac{\delta_{\text{BMM}}}{D_{\text{BMM}}} \quad (77)$$

$$\frac{1}{P_{\text{BMM-B}}^1} = \frac{\delta_{\text{BMM}}}{D_{\text{BMM}}} + \frac{\delta_{\text{B}}}{k_{\text{p}} D_{\text{B}}} \quad (78)$$

Mass and volume conservation. To ensure proper model performance, we tested whether the total mass and volume in the system was conserved during a simulation. We simulated a constant drug concentration of 1 g cm^{-3} in the reservoir, assumed no sampling or drug metabolism in this simulation, and assessed the mass and volume in the system over more than 60h.

Parametric study. In the current Multi-organ and Mixed models, the tissue chambers are discretized into three layers. Chamber discretization is typically used to capture transport delays due to local concentration gradients. In the current models, tissue chamber discretization was optimized using a single tissue chamber test case (without tissue construct), using a similar perfusion media flow rate of 1.5 ml min^{-1} . The test case model for doxorubicin included the following compartments: inlet fluidic channel, fluidic channel, membrane and tissue chamber (Supplementary Fig. 6f). Three test cases with varying spatial subdivisions were performed, where the tissue chamber was discretized with one, three and five layers. In the main text, we have used the time step $\Delta t = 10 \text{ s}$ for the simulation period of 72h. To analyse the effect of time step, we performed simulations with reduced time steps Δt of 1.0s and 0.01s for the total simulation time of 4h. Drug concentration time profiles were monitored at the bottom and top of the chamber.

For $\Delta t = 1.0 \text{ s}$, the three spatial resolution test cases showed similar overlapping concentration-time profiles. For $\Delta t = 0.01 \text{ s}$, a concentration gradient was observed in the five-layer case for the first 7s; however, all concentration-time profiles overlapped for the remainder of the simulation time. This demonstrates that the original time step of $\Delta t = 10 \text{ s}$ and three-layer spatial discretization are adequate for the primary simulations. Our initial approach of discretizing the tissue chamber into three cells allows us to position the individual tissues according to the experimental setup.

Statistics. All measurements reported were taken from distinct samples. Data were analysed in Excel (Microsoft) and graphed in Prism (GraphPad). Data are shown as mean \pm s.d. for a given number of biological replicates. Significant differences were defined by $P < 0.05$ for all statistical methods, unless otherwise noted. Differences between the experimental groups were analysed by unpaired, two-tailed Student's t -test, or one-way or multi-way analysis of variance (ANOVA). Post hoc pairwise analysis was done using Tukey's HSD test.

Reporting Summary. Further information on research design is available in the Nature Research Reporting Summary linked to this article.

Data availability

Source data for some graphs in the main figures and in the Extended Data figures are available as Supplementary Information. All raw and analysed datasets

generated during the study are available from the corresponding author on request. Source data are provided with this paper.

Code availability

All software used to analyse the data is commercial or open-source. The custom code for the analyses of pixel movement can be obtained at <https://www.nature.com/articles/s41596-019-0189-8>.

Received: 8 July 2020; Accepted: 11 March 2022;

Published online: 27 April 2022

References

- Di, L. et al. A perspective on the prediction of drug pharmacokinetics and disposition in drug research and development. *Drug Metab. Dispos.* **41**, 1975–1993 (2013).
- Mak, I. W., Evaniew, N. & Ghert, M. Lost in translation: animal models and clinical trials in cancer treatment. *Am. J. Transl. Res.* **6**, 114–118 (2014).
- Tuntland, T. et al. Implementation of pharmacokinetic and pharmacodynamic strategies in early research phases of drug discovery and development at Novartis Institute of Biomedical Research. *Front. Pharmacol.* **5**, 174 (2014).
- Pound, P. & Ritskes-Hoitinga, M. Is it possible to overcome issues of external validity in preclinical animal research? Why most animal models are bound to fail. *J. Transl. Med.* **16**, 304 (2018).
- Huh, D. et al. Reconstituting organ-level lung functions on a chip. *Science* **328**, 1662–1668 (2010).
- Wikswio, J. P. The relevance and potential roles of microphysiological systems in biology and medicine. *Exp. Biol. Med.* **239**, 1061–1072 (2014).
- Polacheck, W. J. et al. A non-canonical Notch complex regulates adherens junctions and vascular barrier function. *Nature* **552**, 258–262 (2017).
- Shinha, K., Nihei, W., Ono, T., Nakazato, R. & Kimura, H. A pharmacokinetic-pharmacodynamic model based on multi-organ-on-a-chip for drug-drug interaction studies. *Biomicrofluidics* **14**, 044108 (2020).
- Trapecar, M. et al. Gut-liver physiomics reveal paradoxical modulation of IBD-related inflammation by short-chain fatty acids. *Cell Syst.* **10**, 223–239.e9 (2020).
- Low, L. A., Mummery, C., Berridge, B. R., Austin, C. P. & Tagle, D. A. Organs-on-chips: into the next decade. *Nat. Rev. Drug Discov.* **20**, 345–361 (2021).
- Ronaldson-Bouchard, K. et al. Advanced maturation of human cardiac tissue grown from pluripotent stem cells. *Nature* **556**, 239–243 (2018).
- Novak, R. et al. Robotic fluidic coupling and interrogation of multiple vascularized organ chips. *Nat. Biomed. Eng.* **4**, 407–420 (2020).
- Ronaldson-Bouchard, K. & Vunjak-Novakovic, G. Organs-on-a-chip: a fast track for engineered human tissues in drug development. *Cell Stem Cell* **22**, 310–324 (2018).
- Leger, K. J. et al. Circulating microRNAs: potential markers of cardiotoxicity in children and young adults treated with anthracycline chemotherapy. *J. Am. Heart Assoc.* **6**, e004653 (2017).
- McAleer, C. W. et al. Multi-organ system for the evaluation of efficacy and off-target toxicity of anticancer therapeutics. *Sci. Transl. Med.* **11**, eaav1386 (2019).
- Oatmen, K. E. et al. Identification of a novel microRNA profile in pediatric patients with cancer treated with anthracycline chemotherapy. *Am. J. Physiol. Heart Circ. Physiol.* **315**, H1443–H1452 (2018).
- Tacar, O., Sriamornsak, P. & Dass, C. R. Doxorubicin: an update on anticancer molecular action, toxicity and novel drug delivery systems. *J. Pharm. Pharmacol.* **65**, 157–170 (2013).
- Thorn, C. F. et al. Doxorubicin pathways: pharmacodynamics and adverse effects. *Pharmacogenet. Genomics* **21**, 440–446 (2011).
- Yadi, W. et al. Bioinformatic analysis of peripheral blood miRNA of breast cancer patients in relation with anthracycline cardiotoxicity. *BMC Cardiovasc. Disord.* **20**, 43 (2020).
- Schepers, A., Li, C., Chhabra, A., Seney, B. T. & Bhatia, S. Engineering a perfusable 3D human liver platform from iPS cells. *Lab Chip* **16**, 2644–2653 (2016).
- Villasante, A. et al. Tissue-engineered model of human osteolytic bone tumor. *Tissue Eng. C Methods* **23**, 98–107 (2017).
- Itoh, M. et al. Generation of 3D skin equivalents fully reconstituted from human induced pluripotent stem cells (iPSCs). *PLoS ONE* **8**, e77673 (2013).
- Neil, J. E., Brown, M. B. & Williams, A. C. Human skin explant model for the investigation of topical therapeutics. *Sci. Rep.* **10**, 21192 (2020).
- Davies, P. F. Flow-mediated endothelial mechanotransduction. *Physiol. Rev.* **75**, 519–560 (1995).
- Hirschi, K. K. & D'Amore, P. A. Pericytes in the microvasculature. *Cardiovasc. Res.* **32**, 687–698 (1996).

26. Subramanian, A. et al. Gene set enrichment analysis: a knowledge-based approach for interpreting genome-wide expression profiles. *Proc. Natl Acad. Sci. USA* **102**, 15545–15550 (2005).
27. Zeng, H., Wang, J., Clouse, H., Lagrutta, A. & Sannajust, F. Resolving the reversed rate effect of calcium channel blockers on human-induced pluripotent stem cell-derived cardiomyocytes and the impact on in vitro cardiac safety evaluation. *Toxicol. Sci.* **167**, 573–580 (2019).
28. Uhlén, M. et al. Proteomics. Tissue-based map of the human proteome. *Science* **347**, 1260419 (2015).
29. Prantil-Baun, R. et al. Physiologically based pharmacokinetic and pharmacodynamic analysis enabled by microfluidically linked organs-on-chips. *Annu. Rev. Pharmacol. Toxicol.* **58**, 37–64 (2018).
30. Herland, A. et al. Quantitative prediction of human pharmacokinetic responses to drugs via fluidically coupled vascularized organ chips. *Nat. Biomed. Eng.* **4**, 421–436 (2020).
31. Przekwas, A. & Somayaji, M. R. in *Organ-on-a-Chip* (eds Hoeng, J. et al.) 311–361 (Academic Press, 2020). <https://doi.org/10.1016/B978-0-12-817202-5.00011-5>
32. Somayaji, M. R., Das, D. & Przekwas, A. Computational approaches for modeling and analysis of human-on-chip systems for drug testing and characterization. *Drug Discov. Today* **21**, 1859–1862 (2016).
33. Chramiec, A. et al. Integrated human organ-on-a-chip model for predictive studies of anti-tumor drug efficacy and cardiac safety. *Lab Chip* **20**, 4357–4372 (2020).
34. Wang, Y. et al. Taurine zinc solid dispersions attenuate doxorubicin-induced hepatotoxicity and cardiotoxicity in rats. *Toxicol. Appl. Pharmacol.* **289**, 1–11 (2015).
35. Fan, C. et al. Combination breast cancer chemotherapy with doxorubicin and cyclophosphamide damages bone and bone marrow in a female rat model. *Breast Cancer Res. Treat.* **165**, 41–51 (2017).
36. Rigaud, V. O.-C. et al. Circulating miR-1 as a potential biomarker of doxorubicin-induced cardiotoxicity in breast cancer patients. *Oncotarget* **8**, 6994–7002 (2017).
37. Chen, Y. & Wang, X. miRDB: an online database for prediction of functional microRNA targets. *Nucleic Acids Res.* **48**, D127–D131 (2020).
38. Ronaldson-Bouchard, K. et al. Engineering of human cardiac muscle electromechanically matured to an adult-like phenotype. *Nat. Protoc.* **14**, 2781–2817 (2019).
39. Bhumiratana, S. et al. Tissue-engineered autologous grafts for facial bone reconstruction. *Sci. Transl. Med.* **8**, 343ra83 (2016).
40. Marcos-Campos, I. et al. Bone scaffold architecture modulates the development of mineralized bone matrix by human embryonic stem cells. *Biomaterials* **33**, 8329–8342 (2012).
41. Thomas, A. et al. Characterization of vascular permeability using a biomimetic microfluidic blood vessel model. *Biomicrofluidics* **11**, 024102 (2017).
42. Mootha, V. K. et al. PGC-1 α -responsive genes involved in oxidative phosphorylation are coordinately downregulated in human diabetes. *Nat. Genet.* **34**, 267–273 (2003).
43. Navarrete-Perea, J., Yu, Q., Gygi, S. P. & Paulo, J. A. Streamlined Tandem Mass Tag (SL-TMT) protocol: an efficient strategy for quantitative (phospho) proteome profiling using tandem mass tag-synchronous precursor selection-MS3. *J. Proteome Res.* **17**, 2226–2236 (2018).
44. Tyanova, S. et al. The Perseus computational platform for comprehensive analysis of (prote)omics data. *Nat. Methods* **13**, 731–740 (2016).
45. Wang, D. et al. A deep proteome and transcriptome abundance atlas of 29 healthy human tissues. *Mol. Syst. Biol.* **15**, e8503 (2019).
46. Ge, S. X., Jung, D. & Yao, R. ShinyGO: a graphical gene-set enrichment tool for animals and plants. *Bioinformatics* **36**, 2628–2629 (2020).
47. Mi, H., Muruganujan, A., Ebert, D., Huang, X. & Thomas, P. D. PANTHER version 14: more genomes, a new PANTHER GO-slim and improvements in enrichment analysis tools. *Nucleic Acids Res.* **47**, D419–D426 (2019).
48. Ge, S. X., Son, E. W. & Yao, R. iDEP: an integrated web application for differential expression and pathway analysis of RNA-seq data. *BMC Bioinformatics* **19**, 534 (2018).
49. Ru, Y. et al. The multiMiR R package and database: integration of microRNA-target interactions along with their disease and drug associations. *Nucleic Acids Res.* **42**, e133 (2014).
50. Zhang, J. & Storey, K. B. RBiomirGS: an all-in-one miRNA gene set analysis solution featuring target mRNA mapping and expression profile integration. *PeerJ* **6**, e4262 (2018).
51. Korotkevich, G. et al. Fast gene set enrichment analysis. Preprint at *bioRxiv* <https://doi.org/10.1101/060012> (2021).

Acknowledgements

We gratefully acknowledge funding of this research by the NIH (UG3 EB025765, P41 EB027062 and R01 CA249799 to G.V.-N.; R35 CA197745, S10 OD012351 and S10 OD021764 to An.C.; UL1 TR001873 to the Irving Institute for Clinical and Translational Research; P30 CA013696 to the Confocal and Specialized Microscopy Shared Resource), NSF (Engineering Research Center EEC-1647837 to C.S.C. and G.V.-N., Graduate Research Fellowship DGE1644869 to D.N.T.) and F.C.T. (PD/BD/105819/2014 to D.T.). We thank P. L. Graney, E. Öztürk, M. C. Samaritano, N. Valerio Dorrello and B. Fine for helpful discussions; R. Nandakumar and C. Qiao (Biomarkers Core Laboratory at the Irving Institute for Clinical Translational Research), M. Kissner (Columbia Stem Cell Initiative Flow Cytometry Core), C. Damoci (Oncology Precision Therapeutics and Imaging Core Shared Resource), the Molecular Pathology, Confocal and Specialized Microscopy, and the Oncology Precision Therapeutics and Imaging Core Shared Resources at the Columbia University Herbert Irving Comprehensive Cancer Center for technical support.

Author contributions

K.R.-B., D.T., K.Y. and G.V.-N. designed the study; K.R.-B., D.T., A. Chramiec, Y.Z., B.M.L., D.N.T., J.J., M.T., Z.G., R.K.S., E.H.A., A. Pappalardo and S. Stylianos performed experiments; K.Y. and M.S. developed the tissue chip; K.R.-B., D.T., A. Califano, S.T., R.K.S., J.S., B.M.L. and S. Sonar conducted data analyses; A.M.C., C.S.C., K.K.H., S.P.H., C.G. and A. Przekwas provided inputs; K.R.-B., D.T., D.N.T. and G.V.-N. interpreted the data and wrote the manuscript.

Competing interests

G.V.-N. is a co-founder and board director of epiBone, Tara Biosystems, Xylyx Bio and Implatate and holds equity in all four companies. K.R.-B. and Y.Z. are co-founders of TARA Biosystems and hold equity in the company. S.P.H. holds equity in Xylyx Bio. An.C. is founder, equity holder and consultant of DarwinHealth, Inc., a company that has licensed some of the algorithms used in this manuscript from Columbia University. Columbia University is also an equity holder in DarwinHealth, Inc. The other authors declare no competing interests.

Additional information

Extended data is available for this paper at <https://doi.org/10.1038/s41551-022-00882-6>.

Supplementary information The online version contains supplementary material available at <https://doi.org/10.1038/s41551-022-00882-6>.

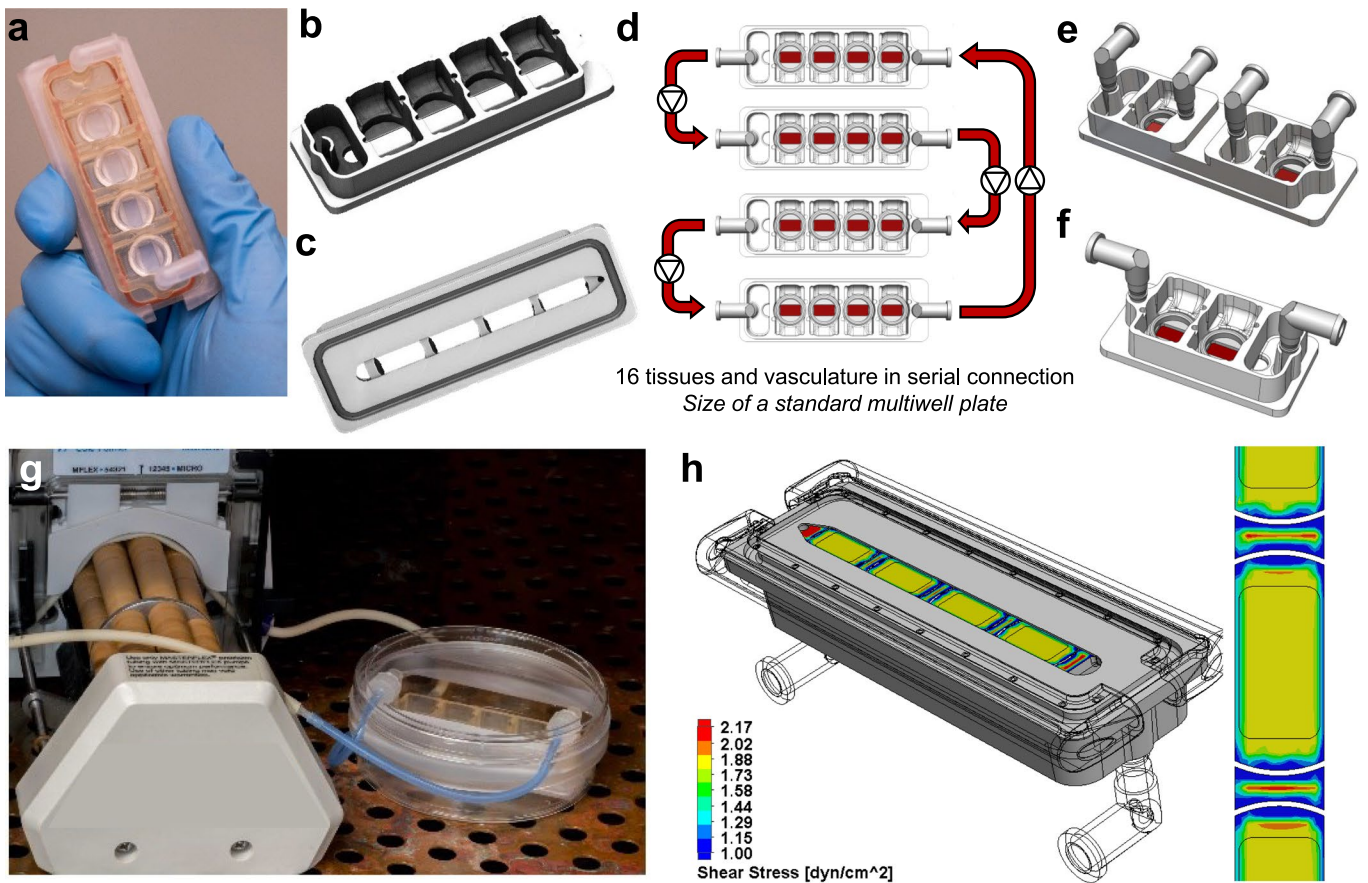
Correspondence and requests for materials should be addressed to Gordana Vunjak-Novakovic.

Peer review information *Nature Biomedical Engineering* thanks Jeffrey Borenstein, Roger Kamm and the other, anonymous, reviewer(s) for their contribution to the peer review of this work.

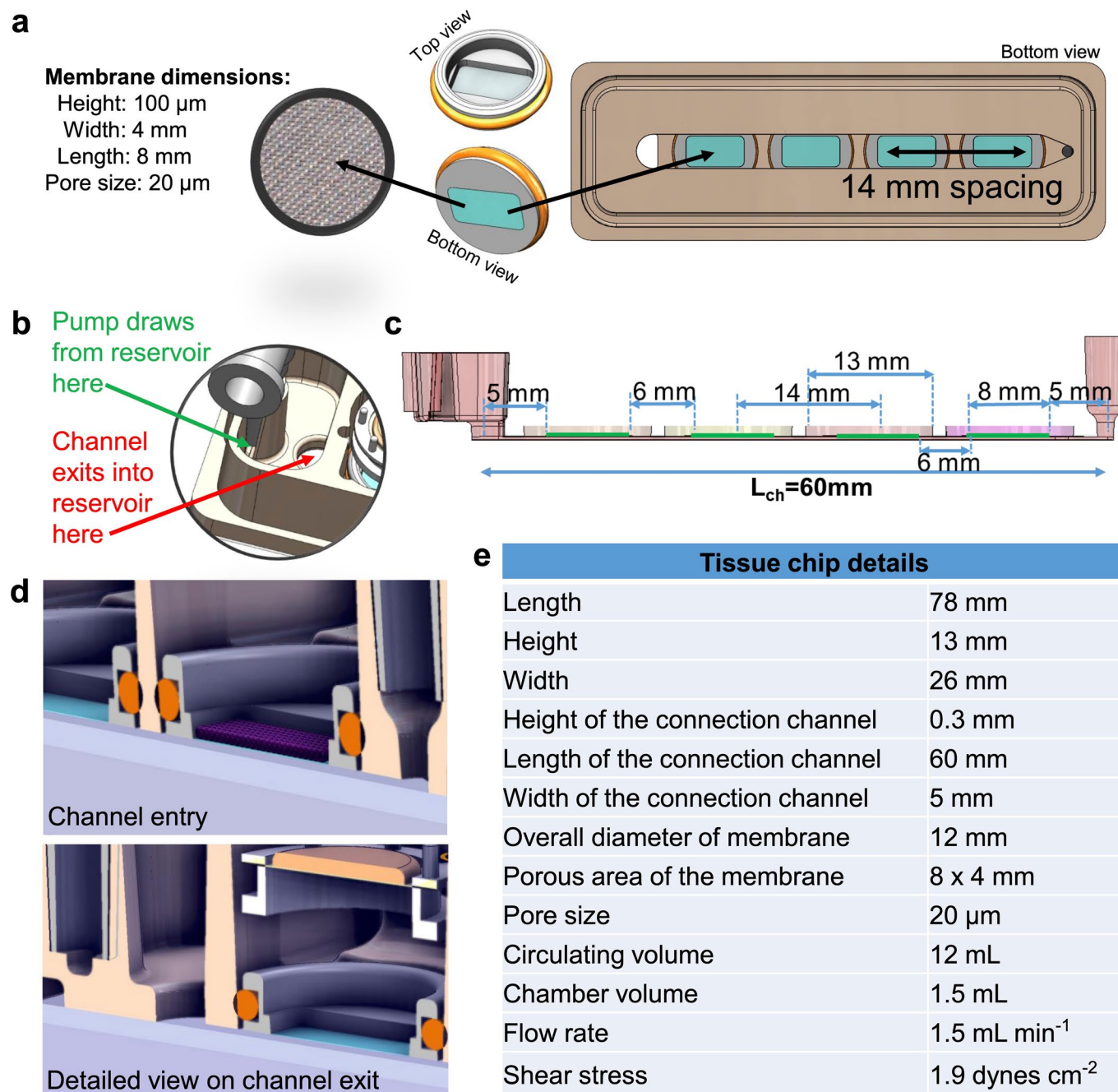
Reprints and permissions information is available at www.nature.com/reprints.

Publisher's note Springer Nature remains neutral with regard to jurisdictional claims in published maps and institutional affiliations.

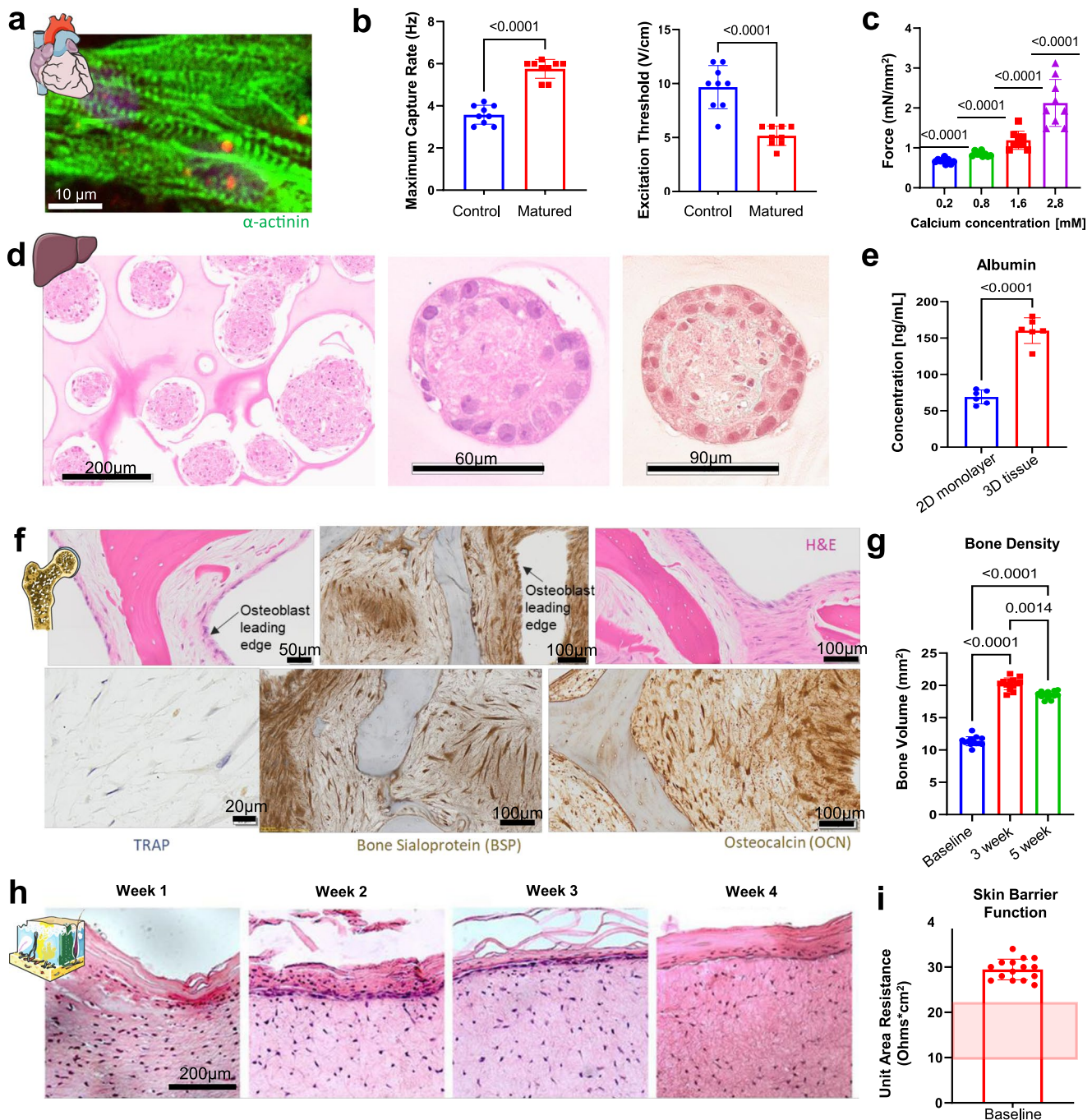
© The Author(s), under exclusive licence to Springer Nature Limited 2022



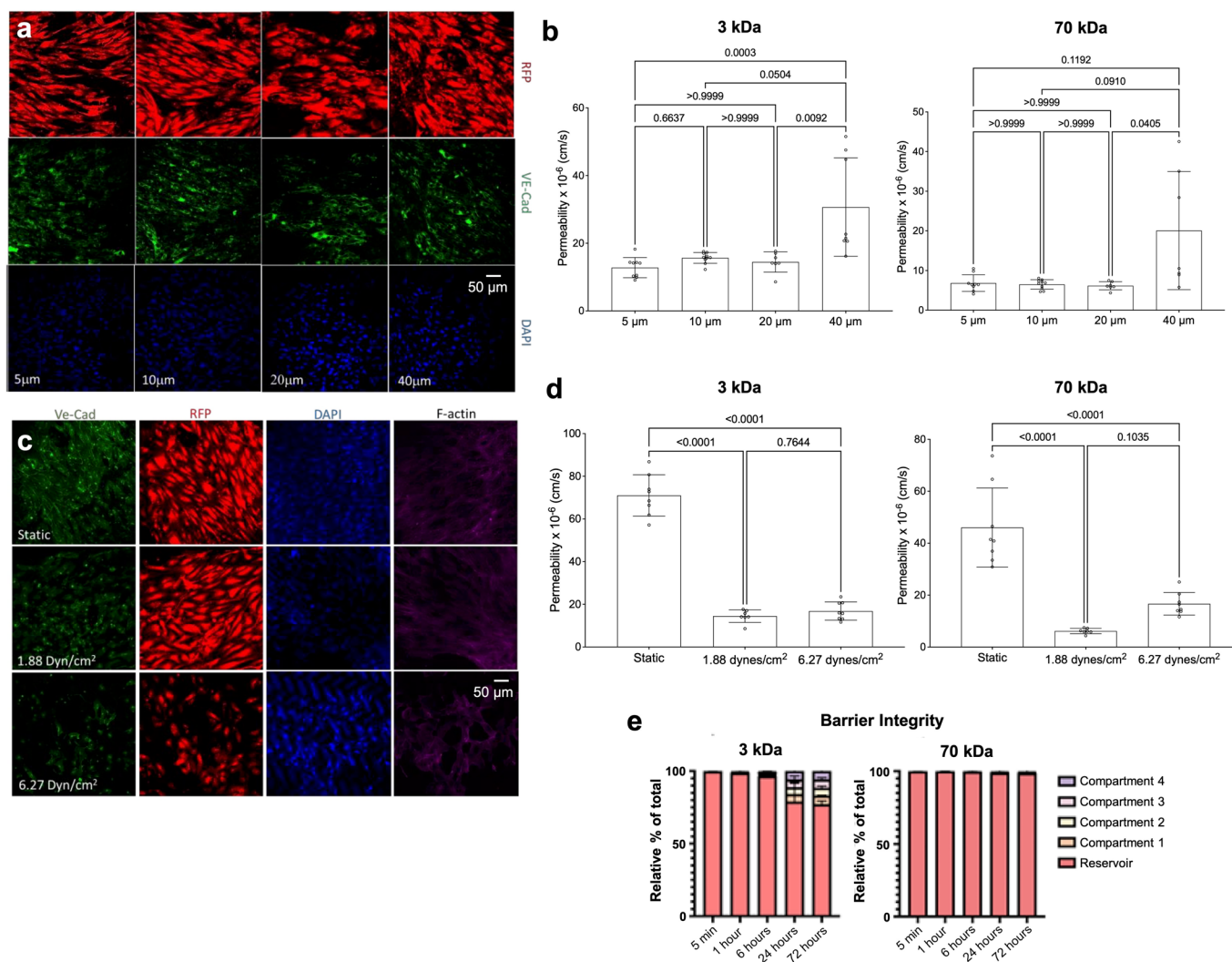
Extended Data Fig. 1 | Tissue chip configurability and modularity. **a**, Photograph of the assembled chip. **b**, Top view of the tissue chip including each compartment chamber and reservoir for circulating media. **c**, Bottom view of the chip. **d**, Configurability of the tissue chip can be established through connecting reactors in series for scaling of engineered organs. **e**, Alternative chip design for single-organ culture with perfusion and vascular barrier. **f**, Alternative chip design for dual-organ culture with perfusion and vascular barrier. **g**, Tissue chip with tubing attached to a peristaltic pump during integrated culture. **h**, Computational fluidic model of shear stress during perfusion with the vascular barrier, at a flow rate of 1.3 mL min^{-1} to yield a shear stress of 1.88 dyn cm^{-2} at the vascular barrier interface.



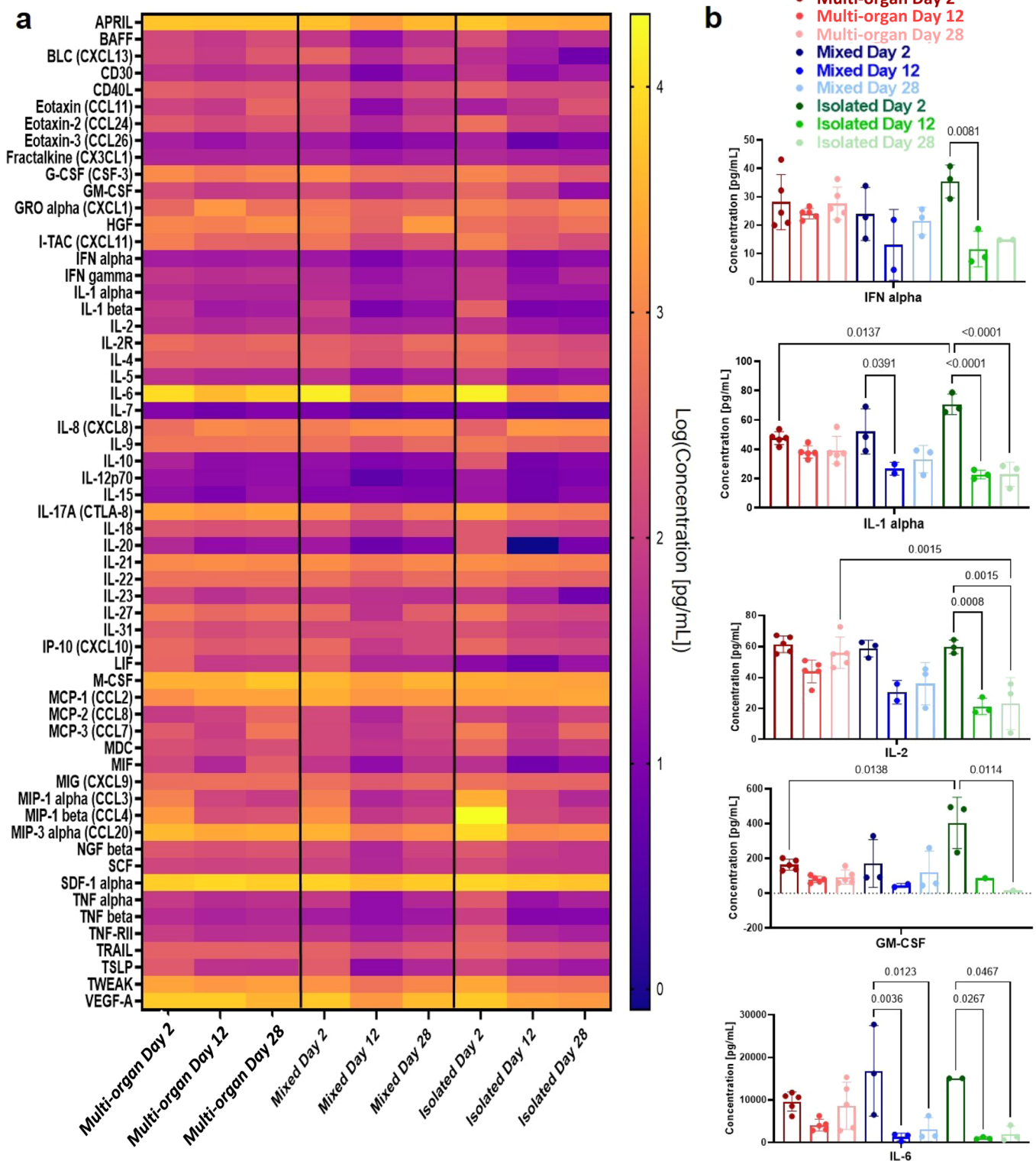
Extended Data Fig. 2 | Tissue chip design details for integration of engineered tissues. **a**, Images and dimensions of the engineered transwell insert and its location within the tissue chip. **b**, Top view of the reservoir to detail routing of fluid from the channel into the reservoir and subsequent pump driven routing into the tubing via the elbow connector. **c**, Schematic side view of the tissue chip with measurements. **d**, Schematic images detailing fluidic routing of vascular media via the designed channel entry and exit ports. **e**, Tissue chip details.



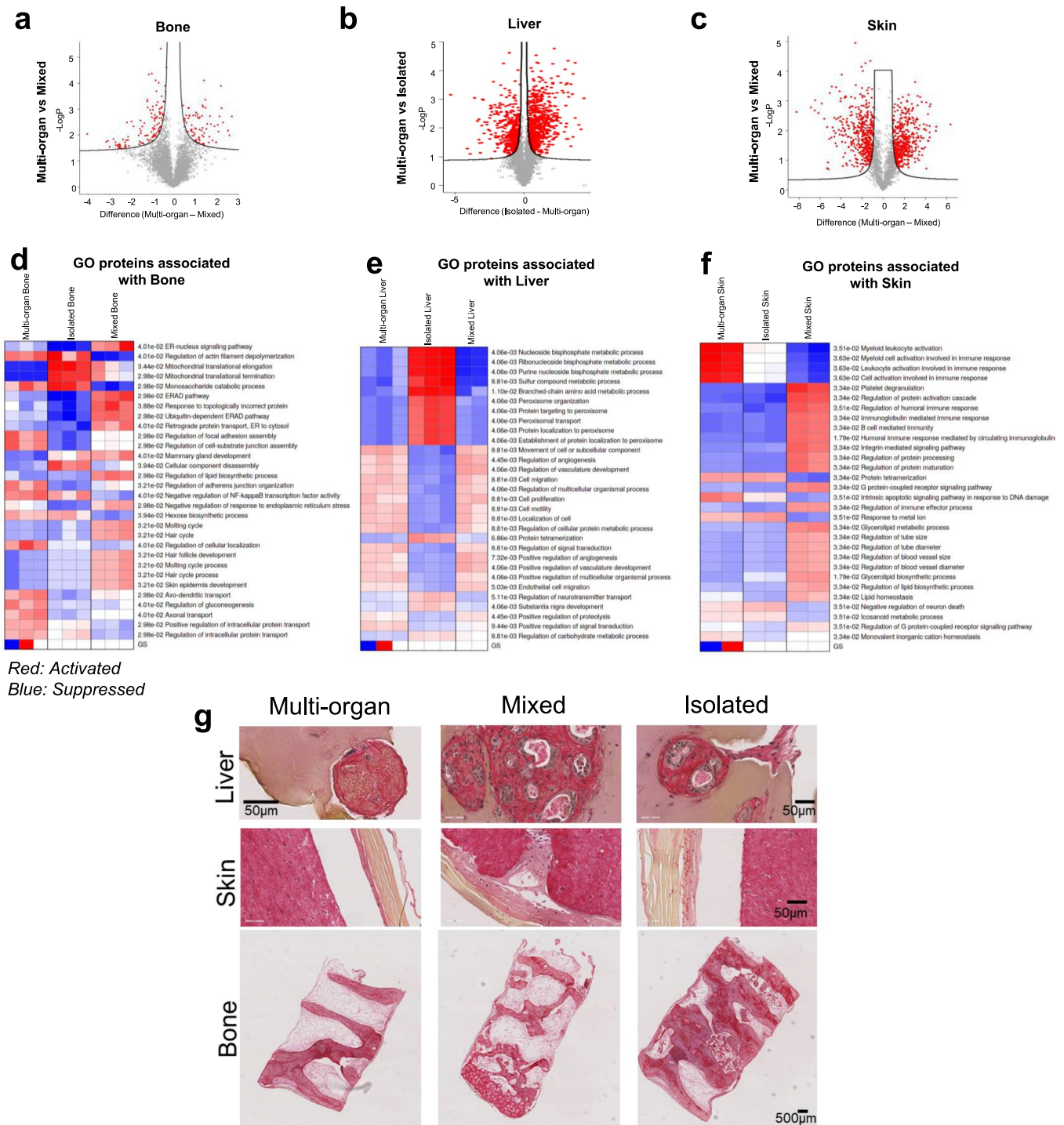
Extended Data Fig. 3 | Characterization of tissue specific maturation. **a-c**, Electromechanically matured cardiac tissues show aligned actinin alpha expression (green, scale bar, 10 μ m) (**a**), functional improvements in maximum capture rate and excitation threshold (**b**) ($n=8-9$ biological replicates), and increased force responses when exposed to increasing calcium concentrations (**c**) ($n=9$ biological replicates). **d-e**, Liver tissues are matured via co-culture of cells in 3D aggregated as detailed by immunohistochemical staining (**d**) and increased albumin secretion (**e**) ($n=6$ biological replicates). **f**, Immunohistochemical staining of engineered bone slices stain positive for osteocalcin, TRAP activity, and bone sialoprotein. **g**, Micro-computed tomography imaging of bone scaffolds over time details bone remodeling during the osteoblastic and osteolytic phases of induced bone maturation ($n=13$ biological replicates). **h**, Immunohistochemical staining of engineered skin slices detail the formation of the epidermis and dermis over 4 weeks of maturation. **i**, TEER values detail the barrier function of the engineered skin, with reported values detailed by the red shaded region²³ ($n=15$ biological replicates). Data is shown as mean \pm SD and statistics determined by unpaired t-test (b, c, e), or one-way ANOVA (g, i).



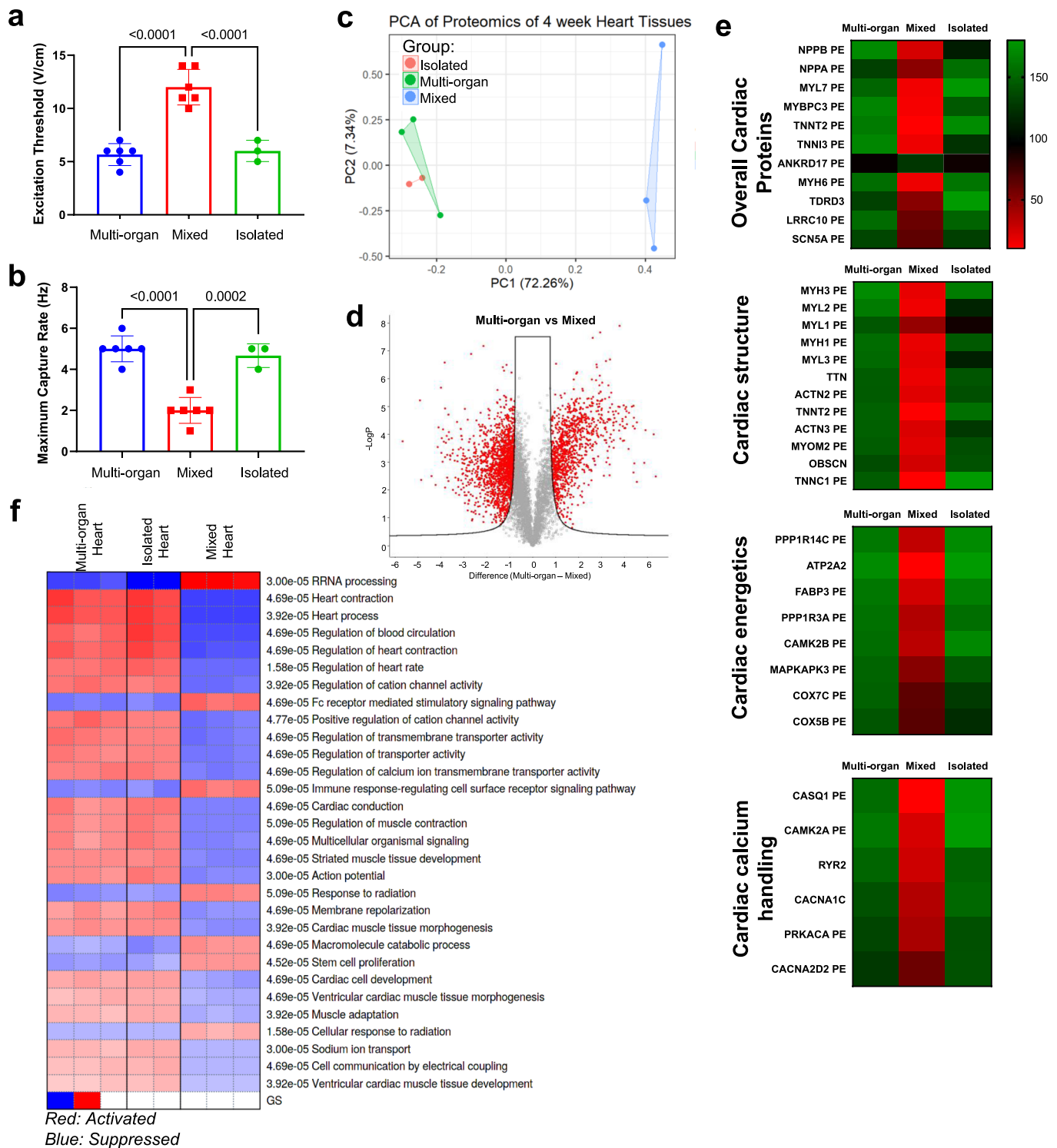
Extended Data Fig. 4 | Establishment of mature, selectively permeable vascular barrier. **a-b**, Immunofluorescence imaging of vascular barriers (**a**) and FITC-Dextran transport through vascular barriers cultured on various transwell pore sizes (**b**) ($n = 7-10$ biological replicates). Scale bar, $50 \mu\text{m}$. **c-d**, Immunofluorescence imaging of vascular barriers (**c**) and FITC-Dextran transport through vascular barriers cultured under different shear stress conditions (**d**) ($n = 7-8$ biological replicates). Scale bar, $50 \mu\text{m}$. **e**, Barrier function demonstrated by tracking tagged dextran molecules of different size ($n = 3$ biological replicates). Data is shown as mean \pm SD and statistics determined by two-way or mixed ANOVA.



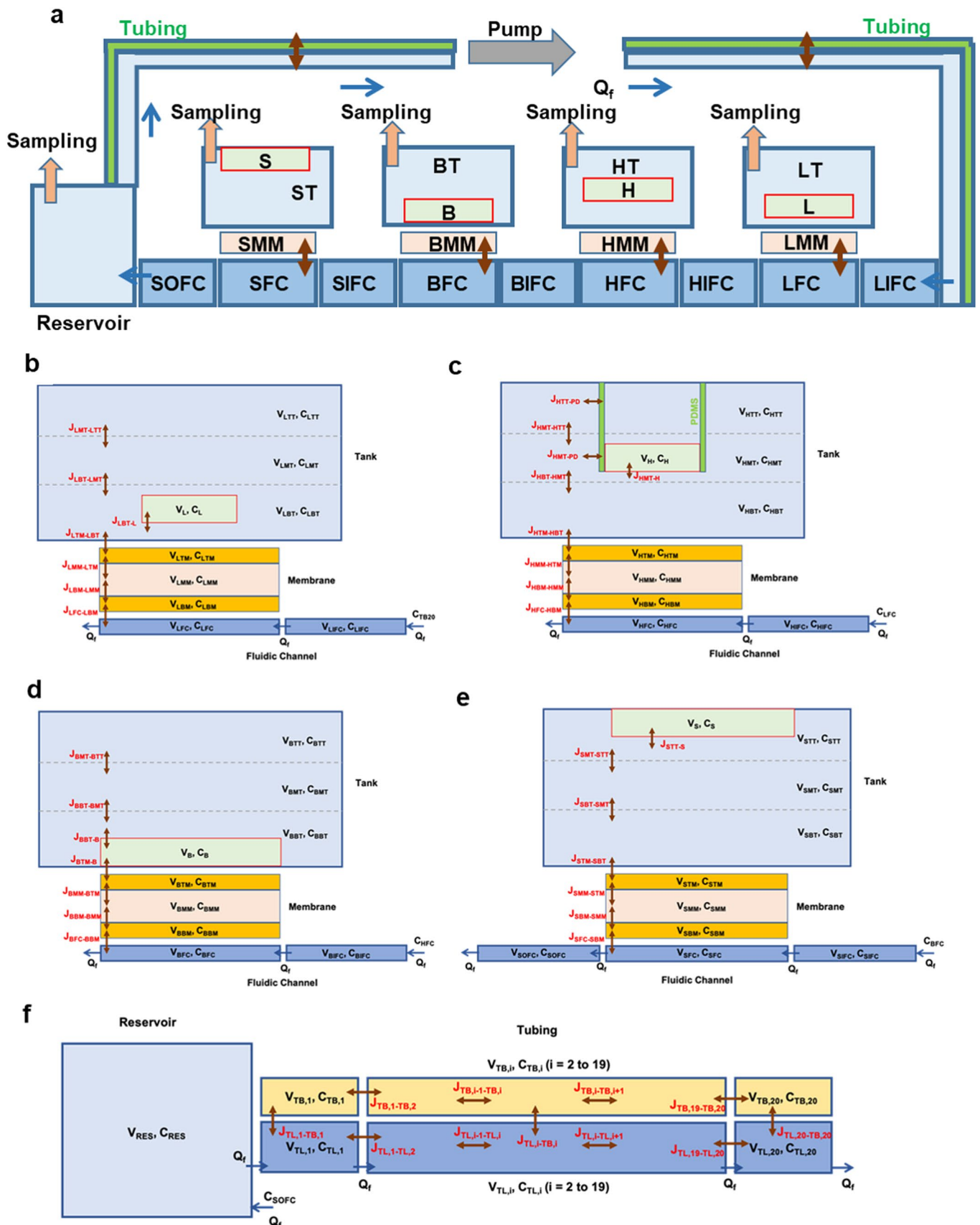
Extended Data Fig. 6 | Immune function over four-week culture. a-b, Heatmap of all measured cytokines (**a**) and individual cytokine expression for selected cytokines (**b**) over 28 days of culture in the different tissue chips configurations (*Multi-organ*, $n=5$ biological replicates; *Mixed* and *Isolated*, $n=3$ biological replicates). Data is shown as mean \pm SD and statistics determined by one-way ANOVA.



Extended Data Fig. 7 | Proteomic breakdown of bone, liver, and skin tissues studied over four weeks in *Multi-organ* multi-tissue chip, in the *Mixed* media approach, and in *Isolation*. a-c, Proteomic breakdown of engineered bone (more than 6,000 unique proteins; **a), liver (more than 2,000 proteins; **b**), and skin (more than 2,000 proteins; **c**) studied over 28 days in the integrated *Multi-organ* multi-tissue chip, chip with mixed media, and tissues cultured in isolation. Comparison of integrated versus mixed conditions via differential protein abundances is represented by Volcano plots. **d-f**, PGSEA plots of the top 30 GO Biological Process pathways, with red indicating activated pathways and blue indicating suppressed pathways for bone (**d**), liver (**e**), and skin (**f**). **g**, Immunohistochemical staining for picrosirius red details collagen within liver, skin, and bone tissues after 28 days. Scale bar for liver and skin stains, 50 µm. Scale bar for bone stains, 500 µm.**

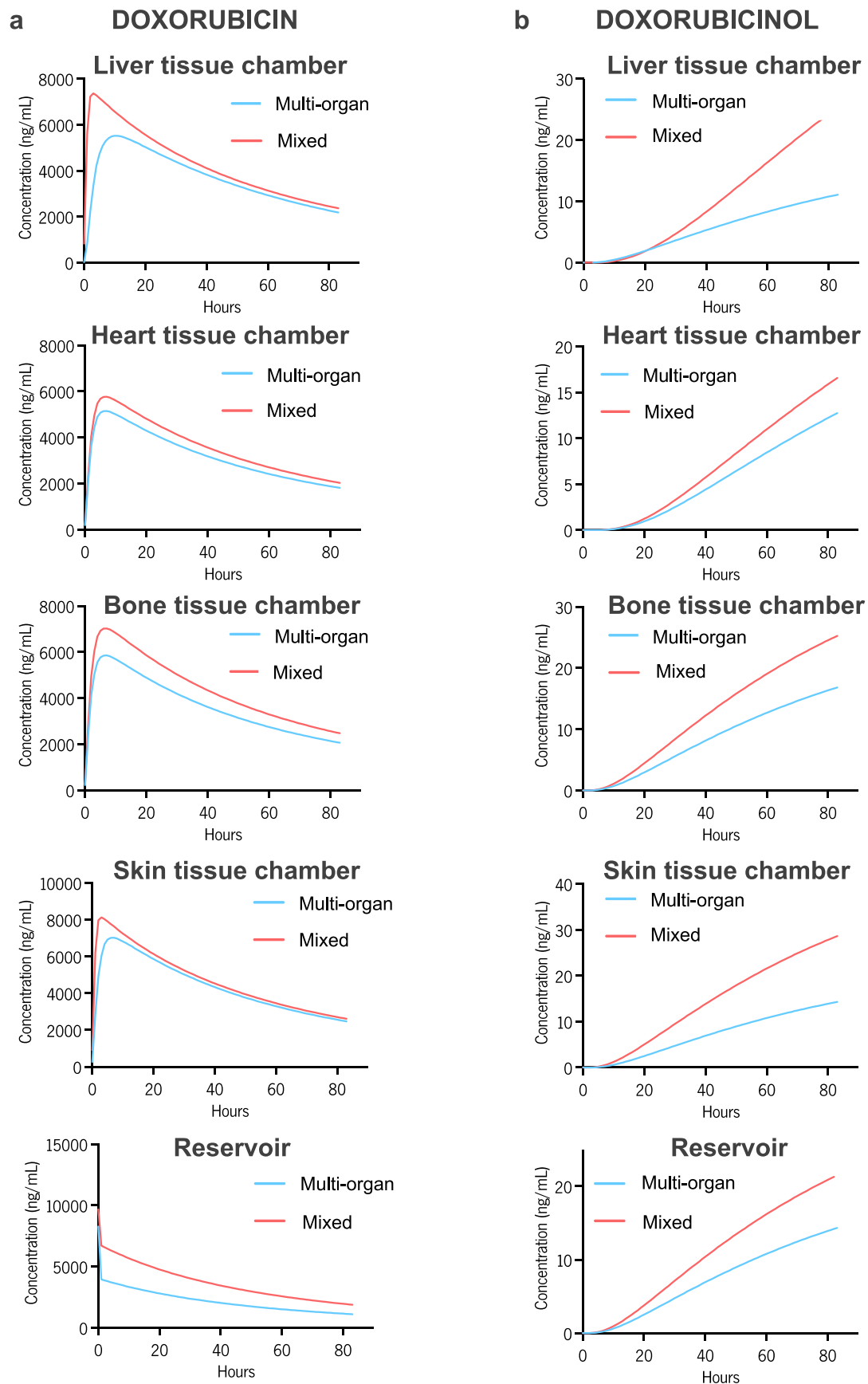


Extended Data Fig. 8 | Proteomic breakdown of engineered cardiac tissues studied over four weeks in *Multi-organ* multi-tissue chip, in the *Mixed* media approach, and in *Isolation*. a-b, Excitation threshold (a) and maximum capture rate (b) of cardiac tissues for each experimental condition (Data is shown as mean \pm SD and statistics determined by Ordinary one-way ANOVA. *Multi-organ* and *Mixed*, $n = 6$ biological replicates; *Isolated*, $n = 3$ biological replicates). c, PCA clustering of each experimental condition. d, Comparison of integrated versus mixed conditions via differential protein abundances. e, Proteins important to cardiac tissue function, structure, energetics, and calcium handling. f, PGSEA pathway analysis showing the top 30 GO Biological Process pathways related to disease and function in integrated vs. mixed conditions, with red indicating activated and blue indicating suppressed pathways.



Extended Data Fig. 9 | See next page for caption.

Extended Data Fig. 9 | Development of a multi-compartment computational model of the multi-tissue chip. **a**, Schematic of the entire mechanistic multi-compartment model. All tissue tanks have a similar configuration that is composed of a cylindrical tank divided in 3 sub-compartments (TT, MT, and BT), an endothelial membrane with 3 layers (TM, MM, and BM), a fluidic inflow segment (IFC), and a fluidic perfusion segment (FC). All the individual compartments were represented by species mass balance equations, calculated using drug flux (J) and volumetric medium flow (Q_v). **b**, Schematic of the liver tissue chamber. **c**, Schematic of the heart tissue chamber. **d**, Schematic of the bone tissue chamber. **e**, Schematic of the skin tissue chamber. **f**, Schematic of the reservoir and tubing.



Extended Data Fig. 10 | Comparison of the Multi-organ and Mixed computational PK models. a-b, Doxorubicin (a) and doxorubicinol (b) levels over time within all tissue chambers and in the reservoir predicted by the computational PK model for the Multi-organ (blue line) and the Mixed platform (red bar).

Reporting Summary

Nature Portfolio wishes to improve the reproducibility of the work that we publish. This form provides structure for consistency and transparency in reporting. For further information on Nature Portfolio policies, see our [Editorial Policies](#) and the [Editorial Policy Checklist](#).

Statistics

For all statistical analyses, confirm that the following items are present in the figure legend, table legend, main text, or Methods section.

n/a Confirmed

- | | | |
|-------------------------------------|-------------------------------------|--|
| <input type="checkbox"/> | <input checked="" type="checkbox"/> | The exact sample size (n) for each experimental group/condition, given as a discrete number and unit of measurement |
| <input type="checkbox"/> | <input checked="" type="checkbox"/> | A statement on whether measurements were taken from distinct samples or whether the same sample was measured repeatedly |
| <input type="checkbox"/> | <input checked="" type="checkbox"/> | The statistical test(s) used AND whether they are one- or two-sided
<i>Only common tests should be described solely by name; describe more complex techniques in the Methods section.</i> |
| <input checked="" type="checkbox"/> | <input type="checkbox"/> | A description of all covariates tested |
| <input checked="" type="checkbox"/> | <input type="checkbox"/> | A description of any assumptions or corrections, such as tests of normality and adjustment for multiple comparisons |
| <input checked="" type="checkbox"/> | <input type="checkbox"/> | A full description of the statistical parameters including central tendency (e.g. means) or other basic estimates (e.g. regression coefficient) AND variation (e.g. standard deviation) or associated estimates of uncertainty (e.g. confidence intervals) |
| <input checked="" type="checkbox"/> | <input type="checkbox"/> | For null hypothesis testing, the test statistic (e.g. F , t , r) with confidence intervals, effect sizes, degrees of freedom and P value noted
<i>Give P values as exact values whenever suitable.</i> |
| <input checked="" type="checkbox"/> | <input type="checkbox"/> | For Bayesian analysis, information on the choice of priors and Markov chain Monte Carlo settings |
| <input checked="" type="checkbox"/> | <input type="checkbox"/> | For hierarchical and complex designs, identification of the appropriate level for tests and full reporting of outcomes |
| <input checked="" type="checkbox"/> | <input type="checkbox"/> | Estimates of effect sizes (e.g. Cohen's d , Pearson's r), indicating how they were calculated |

Our web collection on [statistics for biologists](#) contains articles on many of the points above.

Software and code

Policy information about [availability of computer code](#)

Data collection NIS-Elements (Nikon)

Data analysis All software used to analyse the data is commercial or open-source: Excel (Microsoft), Prism (GraphPad), MATLAB (MathWorks), CoBI (CFD Research), FlowJo (BD Biosciences), SOLIDWORKS Flow Simulation (SolidWorks), IVIS Living Image (PerkinElmer), GSEA (UC San Diego and Broad Institute), Transcriptome Analysis Console (Thermo Fisher Scientific). The custom code for the analyses of pixel movement can be obtained at <https://www.nature.com/articles/s41596-019-0189-8>.

For manuscripts utilizing custom algorithms or software that are central to the research but not yet described in published literature, software must be made available to editors and reviewers. We strongly encourage code deposition in a community repository (e.g. GitHub). See the Nature Portfolio [guidelines for submitting code & software](#) for further information.

Data

Policy information about [availability of data](#)

All manuscripts must include a [data availability statement](#). This statement should provide the following information, where applicable:

- Accession codes, unique identifiers, or web links for publicly available datasets
- A description of any restrictions on data availability
- For clinical datasets or third party data, please ensure that the statement adheres to our [policy](#)

Source data for all graphs in the Main Figures and in the Extended Data Figures are available as Supplementary Information. All raw and analysed datasets generated during the study are available from the corresponding author on request.

Field-specific reporting

Please select the one below that is the best fit for your research. If you are not sure, read the appropriate sections before making your selection.

Life sciences Behavioural & social sciences Ecological, evolutionary & environmental sciences

For a reference copy of the document with all sections, see [nature.com/documents/nr-reporting-summary-flat.pdf](https://www.nature.com/documents/nr-reporting-summary-flat.pdf)

Life sciences study design

All studies must disclose on these points even when the disclosure is negative.

Sample size	All sample sizes were determined on the basis of our previous studies with the same tissues (heart, bone, liver, and skin).
Data exclusions	No data were excluded from the analyses.
Replication	All quantitative data were obtained in replicated experiments, and the findings were reproduced from one experiment to another.
Randomization	Engineered tissues were randomly allocated into the experimental groups and analytical assays.
Blinding	The investigators as well as facilities providing specific analytical assessments were blinded to experimental-group allocation.

Reporting for specific materials, systems and methods

We require information from authors about some types of materials, experimental systems and methods used in many studies. Here, indicate whether each material, system or method listed is relevant to your study. If you are not sure if a list item applies to your research, read the appropriate section before selecting a response.

Materials & experimental systems

n/a	Involvement in the study
<input type="checkbox"/>	<input checked="" type="checkbox"/> Antibodies
<input type="checkbox"/>	<input checked="" type="checkbox"/> Eukaryotic cell lines
<input checked="" type="checkbox"/>	<input type="checkbox"/> Palaeontology and archaeology
<input checked="" type="checkbox"/>	<input type="checkbox"/> Animals and other organisms
<input checked="" type="checkbox"/>	<input type="checkbox"/> Human research participants
<input checked="" type="checkbox"/>	<input type="checkbox"/> Clinical data
<input checked="" type="checkbox"/>	<input type="checkbox"/> Dual use research of concern

Methods

n/a	Involvement in the study
<input checked="" type="checkbox"/>	<input type="checkbox"/> ChIP-seq
<input type="checkbox"/>	<input checked="" type="checkbox"/> Flow cytometry
<input checked="" type="checkbox"/>	<input type="checkbox"/> MRI-based neuroimaging

Antibodies

Antibodies used

Anti-VE-Cadherin: Sino Biological; Catalog# 10433-MM01; Clone 01; Dilution 1:250
 Anti-VE Cadherin: Abcam; Catalog # ab33168; Clone N/A; Dilution 1:250
 Anti-Actin alpha 2: Thermo Fisher Scientific; Catalog # 701914; Clone 7H1L69; Dilution 1:100
 Anti-Cytochrome P450 CYP3A4: Millipore; Catalog # AB1254; Clone N/A; Dilution 1:50
 Anti-Albumin: Thermo Fisher Scientific; Catalog # A80-229F; Clone N/A; Dilution 1:100
 Anti-Keratin 14: Biolegend; Catalog # PRB-155P; Clone N/A; Dilution 1:100
 Anti-Vimentin: Santa Cruz Biotechnology; Catalog # sc-6260; Clone V9; Dilution 1:100
 Anti-Bone sialoprotein II: Millipore Sigma; Catalog # AB1854; Clone N/A; Dilution 1:500
 Anti-Osteocalcin: Millipore Sigma; Catalog # AB10911; Clone N/A; Dilution 1:500
 Anti-CD45: Biolegend; Catalog # 304006; Clone HI30; Dilution 1:100
 Anti-CD14: Biolegend; Catalog # 301834; Clone M5E2; Dilution 1:100
 Anti-ITGAM (CD11b): Biolegend; Catalog # 301324; Clone ICRF44; Dilution 1:100
 Anti-CD68: Biolegend; Catalog # 333807; Clone Y1/82A; Dilution 1:100
 Anti-Troponin T: Thermo Fisher Scientific; Catalog # BS-10648R; Clone N/A; Dilution 1:50
 Goat anti-Mouse: Thermo Fisher Scientific; Catalog # A-11029; Clone N/A; Dilution 1:400
 Goat anti-Rabbit: Thermo Fisher Scientific; Catalog # A-11012; Clone N/A; Dilution 1:200
 Rabbit anti-Human: Thermo Fisher Scientific; Catalog # PA1-28834; Clone N/A; Dilution 1:500

Validation

All antibodies used in this study were validated, and detailed information can be found on the manufacturers' websites:

Anti-VE-Cadherin: <https://www.sinobiological.com/antibodies/human-ve-cadherin-10433-mm01>
 Anti-VE Cadherin: <https://www.abcam.com/ve-cadherin-antibody-intercellular-junction-marker-ab33168.html>
 Anti-Actin alpha 2: <https://www.thermofisher.com/antibody/product/alpha-Actinin-2-Antibody-clone-7H1L69-Recombinant-Monoclonal/701914>
 Anti-Cytochrome P450 CYP3A4: <https://www.emdmillipore.com/US/en/product/Anti-Cytochrome-P450-Enzyme-CYP3A4->

Antibody,MM_NF-AB1254

Anti-Albumin: <https://www.thermofisher.com/antibody/product/Human-Albumin-Antibody-Polyclonal/A80-229F>Anti-Keratin 14: <https://www.biolegend.com/en-us/products/keratin-14-polyclonal-antibody-purified-10953?GroupID=GROUP26>Anti-Vimentin: <https://www.scbt.com/p/vimentin-antibody-v9>Anti-Bone sialoprotein II: https://www.emdmillipore.com/US/en/product/Anti-Bone-Sialoprotein-II-Antibody,MM_NF-AB1854Anti-Osteocalcin: https://www.emdmillipore.com/US/en/product/Anti-Osteocalcin-Antibody,MM_NF-AB10911Anti-CD45: <https://www.biolegend.com/en-us/products/fitc-anti-human-cd45-antibody-707?GroupID=BLG5926>Anti-CD14: <https://www.biolegend.com/en-us/products/brilliant-violet-605-anti-human-cd14-antibody-7653?GroupID=BLG10263>Anti-ITGAM (CD11b): <https://www.biolegend.com/en-us/products/brilliant-violet-421-anti-human-cd11b-antibody-7325>Anti-CD68: <https://www.biolegend.com/en-us/products/pe-anti-human-cd68-antibody-4845>Anti-Troponin T: <https://www.thermofisher.com/antibody/product/Troponin-T-Antibody-Polyclonal/BS-10648R>Goat anti-Mouse: <https://www.thermofisher.com/antibody/product/Goat-anti-Mouse-IgG-H-L-Highly-Cross-Adsorbed-Secondary-Antibody-Polyclonal/A-11029>Goat anti-Rabbit: <https://www.thermofisher.com/antibody/product/Goat-anti-Rabbit-IgG-H-L-Cross-Adsorbed-Secondary-Antibody-Polyclonal/A-11012>Rabbit anti-Human: <https://www.thermofisher.com/antibody/product/Rabbit-anti-Human-IgG-H-L-Cross-Adsorbed-Secondary-Antibody-Polyclonal/PA1-28834>

Eukaryotic cell lines

Policy information about cell lines

Cell line source(s)

The human hiPSC line, WTC-11, was obtained from Bruce Conklin, Gladstone Institute, through a Material Transfer Agreement. Peripheral blood mononuclear cells (PBMCs) were obtained from the New York Blood Center.

We purchased the following cell lines:

Normal human dermal fibroblasts (NHDF) from Lonza, Catalog # PCS-201-012

iCell Hepatocytes from CDI, Catalog # C1023

Mesenchymal stromal cells (MSCs) from Lonza, Catalog # PT-2501

Human umbilical venous endothelial cells (HUVECs) from Angio-Proteomie, Catalog # cAP-0001RFP

Authentication

The WTC-11 line has been characterized in a previously published manuscript (Kreitzer et al., Am J Stem Cells, 2013) and its certificate can be obtained at https://www.coriell.org/0/Sections/Search/Sample_Detail.aspx?Ref=GM25256. For peripheral blood mononuclear cells: <https://www.nybc.org/products-and-services/blood-products/research-products>

All other cells were validated, and detailed information can be found on the manufacturers' websites:

Normal human dermal fibroblasts: <https://www.atcc.org/products/pcs-201-012#generalinformation>

iCell Hepatocytes: <https://www.fujifilmcdi.com/icell-hepatocytes-20-01279-ghpc01279>

Mesenchymal stromal cells: https://bioscience.lonza.com/lonza_bs/US/en/Primary-and-Stem-Cells/p/000000000000186706/hMSC---Human-Mesenchymal-Stem-Cells

Human umbilical vein endothelial cells: <https://www.angioproteomie.com/ccp3099-rfp-expressing-human-umbilical-veinendothelial-c-cap-0001rfp.htm>

Mycoplasma contamination

The cells were regularly tested for mycoplasma.

Commonly misidentified lines (See [ICLAC](https://www.iclac.org/) register)

No commonly misidentified cells were used.

Flow Cytometry

Plots

Confirm that:

- The axis labels state the marker and fluorochrome used (e.g. CD4-FITC).
- The axis scales are clearly visible. Include numbers along axes only for bottom left plot of group (a 'group' is an analysis of identical markers).
- All plots are contour plots with outliers or pseudocolor plots.
- A numerical value for number of cells or percentage (with statistics) is provided.

Methodology

Sample preparation

All samples were collected and washed with a FACS buffer (1 mM EDTA and 2% FBS in PBS), filtered through a 40-um mesh cell strainer, and stained prior to acquisition on the Bio-Rad ZE5 Cell Analyzer or Agilent NovoCyte Quanteon. The circulating cells were collected from primary human peripheral blood donors and subjected to magnetic cell sorting for CD14 (Miltenyi Biotec) prior to use.

Instrument

Bio-Rad ZE5 Cell Analyzer and Agilent NovoCyte Quanteon

Software

FlowJo 10.6.1 (BD Biosciences)

Cell population abundance

> 98% CD14+, ITGAM (CD11b)+ cells were used after magnetic cell sorting.

Gating strategy

Multiple gating strategies were used for analysis. First gating for total cells and single cells (removing doublets), then for DRAQ5+ cells to account for live cells and to distinguish from debris.

Tick this box to confirm that a figure exemplifying the gating strategy is provided in the Supplementary Information.